In this work spin injection into GaAs from Fe and (Ga,Mn)As was investigated. For the realization of any spintronic device the detailed knowledge about the spin lifetime, the spatial distribution of spin-polarized carriers and the influence of electric fields is essential. In the present work all these aspects have been analyzed by optical measurements of the polar magneto-optic Kerr effect (pMOKE) at the cleaved edge of the samples. Besides the attempt to observe spin pumping and thermal spin injection into n-GaAs the spin solar cell effect is demonstrated, a novel mechanism for the optical generation of spins in semiconductors with potential for future spintronic applications. Also important for spin-based devices as transistors is the presented realization of electrical spin injection into a two-dimensional electron gas.

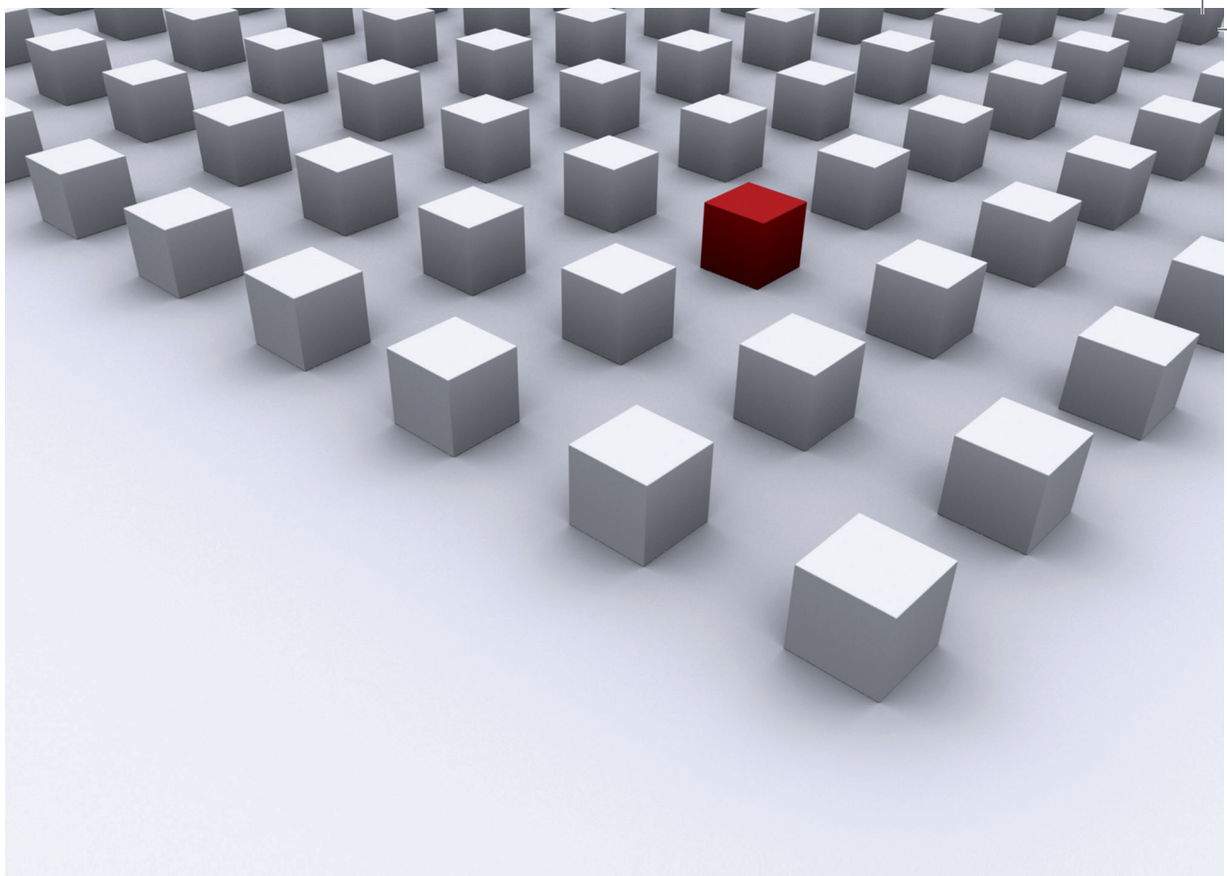

Dissertationsreihe Physik - Band 34

Bernhard Endres

Spin injection into GaAs

Universitätsverlag Regensburg

ISBN 978 3 86845 102 3 ISBN 978-3-86845-102-3

gefördert von:

Alumni der physikalischen Fakultät der Universität Regensburg e.V.

Universität Regensburg

Bernhard Endres

34

Dissertationsreihe Physik

Universitätsverlag Regensburg

Bernhard Endres

Spin injection into GaAs

Spin injection into GaAs

Dissertation zur Erlangung des Doktorgrades der Naturwissenschaften (Dr. rer. nat.)
der Fakultät für Physik der Universität Regensburg
vorgelegt von

Bernhard Endres
Regensburg
2013

Die Arbeit wurde von Prof. Dr. Günther Bayreuther angeleitet.
Das Promotionsgesuch wurde am 22.11.2012 eingereicht.

Prüfungsausschuss:	Vorsitzender:	Prof. Dr. V. Braun
	1. Gutachter:	Prof. Dr. G. Bayreuther
	2. Gutachter:	Prof. Dr. D. Bougeard
	weiterer Prüfer:	Prof. Dr. D. Weiss

Dissertationsreihe der Fakultät für Physik der Universität Regensburg, Band 34

Herausgegeben vom Präsidium des Alumnivereins der Physikalischen Fakultät:
Klaus Richter, Andreas Schäfer, Werner Wegscheider, Dieter Weiss

Bernhard Endres

Spin injection into GaAs

Universitätsverlag Regensburg

Bibliografische Informationen der Deutschen Bibliothek.
Die Deutsche Bibliothek verzeichnet diese Publikation
in der Deutschen Nationalbibliografie. Detailierte bibliografische Daten
sind im Internet über http://dnb.ddb.de abrufbar.

1. Auflage 2013

Leibnizstraße 13, 93055 Regensburg

Konzeption: Thomas Geiger
Umschlagentwurf: Franz Stadler, Designcooperative Nittenau eG
Layout: Bernhard Endres
Druck: Docupoint, Magdeburg
ISBN: 978-3-86845-102-3

Weitere Informationen zum Verlagsprogramm erhalten Sie unter:
www.univerlag-regensburg.de

Spin injection into GaAs

Dissertation

zur Erlangung des Doktorgrades
der Naturwissenschaften (Dr. rer. nat.)
der Fakultät für Physik
der Universität Regensburg

vorgelegt von

Bernhard Endres

aus Regensburg

Mai 2013

Promotionsgesuch eingereicht am: 20.11.2012

Die Arbeit wurde angeleitet von: Prof. Dr. Günther Bayreuther

Prüfungsausschuss:	Vorsitzender:	Prof. Dr. V. Braun
	1. Gutachter:	Prof. Dr. G. Bayreuther
	2. Gutachter:	Prof. Dr. D. Bougeard
	weiterer Prüfer:	Prof. Dr. D. Weiss

Contents

1. Introduction

Today, modern information technology is mainly based on semiconductors and ferromagnets. While data processing and computing usually takes place in semiconductor transistors, information is mostly stored magnetically on hard discs[1]. In field effect transistors (FET) a gate contact controls the "on" and "off" state of a transistor, if electron charge can pass through or not. This technology has experienced a remarkable performance boost since its invention - mainly due to minimization, i.e. the systematic reduction of the device dimensions. This trend is reflected in Moore's Law [1] from 1965, predicting that the amount of transistors per area is doubled each 18 month. However, the ongoing size scaling will come into conflict with practical and fundamental limits in the near future, when the transistor size reaches the atomic scale. Quantum mechanical effects such as tunneling will then prevent the "off" state of the FET.

Up to now, the whole semiconductor technology including FETs only makes use of the electron charge, completely ignoring the associated electron spin and the connected magnetic moment. Electron spins are randomly aligned in these devices and hence cannot be used for information processing. Consequently, by integrating spin polarized currents and using the carrier spin as a new degree of freedom, there is a huge potential to further improve this technology and enhance functionality. This active field of research, also called spintronics, is a potential candidate for future electronic devices. It was triggered by the discovery of the giant magnetoresistance (GMR) effect in 1988 [2, 3]. Its implementation in read heads for hard discs led to the breakthrough of stored information density and showed the economic potential for spintronic devices. In 2007, A. Fert and P. Grünberg were honored with the Nobel Prize in Physics for the discovery of this effect.

In contrast to metal-based spintronic effects as GMR, semiconductor-based spintronics offers new prospects. This is due to the existence of a bandgap and the ability to control carrier concentration via doping, gate voltages, band-bending and light irradiation. Basically, there are four key requirements for the realization of a semiconductor spintronic device:

- efficient injection of spin-polarized electrons into the semiconductor,

[1] beside the growing influence of semiconductor-based solid state drives (SSDs)

- reasonable spin diffusion lengths and spin lifetimes in the semiconductor to preserve and transfer the information,
- effective control and manipulation of the spins for the requested functionality,
- efficient detection of the spins to generate the output.

A natural source of electron spin polarization is provided by ferromagnetic materials, which are mostly used for information storage, e.g. in hard discs, since the magnetization direction is an ideal, nonvolatile possibility to mimic the "1" and "0" of a digital bit. The use of ferromagnetic electrodes enables to electrically inject and detect spin polarized currents in semiconductors. Since the rotation of the electron spin orientation is, in principle, less energy consuming than the movement of electron charges [4], FETs using the orientation of a spin polarized current to control the "on" and "off" state have the potential to improve this technology beyond the ultimate scaling limits of the existing silicon-based CMOS[2] technology [5, Chap. 17]. The basic structure of a Spin-FET is sketched in Fig. 1.1 as an example for the integration of magnetism in semiconductors. Combining ferromagnets and semiconductors also opens the window for the incorporation of information storage and information processing.

A further advantage of semiconductors and their bandgap is the interaction with light, on which the large optoelectronic industry is based. As an example for the insertion of photonics, a Spin-LED is sketched in Fig. 1.1, converting a spin polarized current into circularly polarized light. Altogether, by merging these different technologies, the realization of storage, detection, logic and communication on a single chip should be possible [5, Chap. 1]. However, despite the intense research in recent years, a commercial semiconductor spintronic device is still waiting for its realization.

A first step for the realization of any semiconductor spintronic device is the generation of spin polarized currents in semiconductors. For that purpose GaAs is an excellent candidate for several reasons: first of all a large spin lifetime was found in n-doped GaAs of about 100 ns [7], as well as long spin transport distances (100 µm in n-type GaAs) [8, 9]. Furthermore, ferromagnetic materials can be grown epitaxially on GaAs, e.g. Fe or (Ga,Mn)As, which is a dilute magnetic semiconductor. In addition, GaAs as direct semiconductor is well suited for the interaction with light. The Spin-LED for instance has proved to be successful to demonstrate and quantify the efficient spin injection into GaAs based heterostructures, which was first shown in 1999 with magnetic semiconductors as injector material [10, 11]. The direct bandgap in GaAs also enables the optical detection of spin polarization via the polar magneto-optic Kerr effect (pMOKE).

[2] complementary metal-oxide-semiconductor

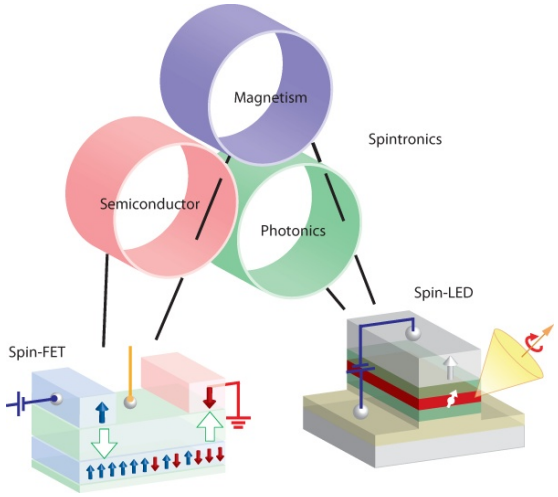

Figure 1.1.: Integration of magnetism in semiconductors may lead to the realization of novel devices as the spin field effect transistor (Spin-FET). In combination with photonics Spin-LEDs could already be realized, converting a spin-polarized current into circularly polarized light (from [6]).

This approach in conjunction with a scanning technique is utilized in this work to visualize spin injection into GaAs and analyze the resulting spin density distribution in the GaAs channel. By means of a special measurement geometry, a direct observation of the injected spin accumulation in GaAs is feasible, even below the ferromagnetic electrodes and without the need of external magnetic fields. This technique was first applied by Kotissek et al. in 2007 [12], demonstrating electrical spin injection from an FeCo contact into n-type GaAs. The here presented work extends the observations with Fe and (Ga,Mn)As as injector materials and provides further insights for spin injection into GaAs.

The layout of the presented work is as follows: the second chapter describes the fundamentals and the theoretical background. It begins with an introduction into the optical properties of GaAs, also explaining the principle of the optical detection mechanism. In Sec. 2.2 the processes relevant for the relaxation of the spin polarization in GaAs will be explained, which are directly connected with the electronic properties, i.e. the doping density in GaAs. Theoretical aspects for the generation of spin-polarized currents in GaAs by electrical spin injection from ferromagnetic materials will be discussed in Sec. 2.4. The subsequent sections then describe spin injection from Fe and (Ga,Mn)As into GaAs, including the formation of the essential tunnel barrier between ferromagnet and semiconductor for efficient spin injection.

Chap. 3 gives an overview of the used methods, sample geometry and measurement principle. An important tool is the Hanle measurement explained in Sec. 3.5, which describes the depolarization of the injected spins in an external

magnetic field and allows to extract the spin lifetime.

The experimental results are summarized in Chap. 4, first demonstrating electrical spin injection from Fe and (Ga,Mn)As into n-doped GaAs. In addition new insights in the distribution and relaxation of the injected spin accumulation are given. In Sec. 4.3, a novel and efficient mechanism to optically generate spins in semiconductors is shown, the spin solar cell and spin photodiode effect. A comparison between thermal and electrical spin injection in Sec. 4.4 then shows the practical obstacles that have to be overcome for efficient thermal spin injection. Finally, optical results from electrical spin injection into a GaAs-based two-dimensional electron gas are discussed in Sec. 4.5.

Chap. 5 then summarizes the results and gives an outlook for future experiments.

2. Fundamentals and theory

2.1. Optical properties of GaAs

Before discussing electrical spin injection, a brief introduction into the basic band structure features of GaAs is given. The III-V semiconductor GaAs has a zinc-blende structure, i.e. the Ga and As atoms occupy a face-centered cubic lattice that is shifted against each other along the space diagonal. Each atom constitutes the center of a tetrahedron, shaped by four atoms of the other component. The valence band and conduction band are then formed by the 4s and 4p states of the Ga and As atoms.

GaAs is a direct band gap semiconductor with the band gap at the center of the Brillouin zone (Γ-point). Thus, as shown in Fig. 2.1a, the conduction band (CB) and valence band are separated by an energy gap E_g (about 1.52 eV at 0 K). The conduction band is two-fold degenerate and consists of s-like states (total angular momentum $j = 1/2$). The valence bands, on the other hand, consist of p-like states with a two-fold degenerate heavy-hole (HH) and light-hole (LH) subband ($j = 3/2$), and a two-fold degenerate split-off (SO) band ($j = 1/2$) separated by the spin-orbit energy $\Delta_{\mathrm{SO}} = 0.34\,\mathrm{eV}$.

Fig. 2.1b shows the optical transitions in GaAs between the valence band and the conduction band. The circled numbers indicate the corresponding transition probabilities for left and right circularly polarized light (σ^+ and σ^-). For photons with the energy of the bandgap E_g (1.515 eV at 10 K), only transitions from the HH and LH states into the conduction band are allowed. However, these transitions obey selection rules that preserve the angular momentum of the absorbed photon of +1 or -1 (denoted by σ^+ and σ^-), respectively. Thus, only four different transitions are allowed. Light with σ^+-polarization, for instance, will generate electrons with $m_j = -1/2$ for heavy hole transitions and electrons with $m_j = 1/2$ for light hole transitions. Since the transitions HH→CB are three times more likely than LH→CB transitions, the absorption of light with σ^+-polarization results in a spin imbalance in the GaAs conduction band.

This means, circularly polarized light can be used to create an unequal occupation of electrons with the spin orientation parallel and anti-parallel to the propagation direction of the incident light. This method has been shown to be useful for

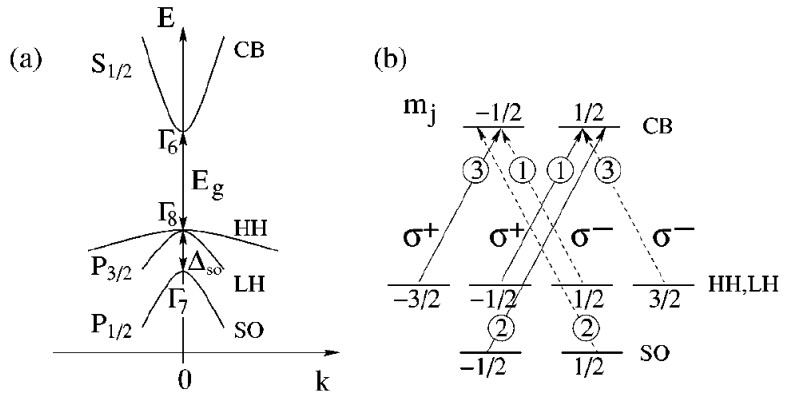

Figure 2.1.: Optical transitions in GaAs (from [13]). (a) Schematic band structure of GaAs near the Γ-point illustrating the band gap E_g, the spin-orbit splitting Δ_{SO} , the conduction band (CB), the heavy hole band (HH), the light hole band (LH) and the spin-orbit split-off band (SO). (b) Optical selection rules between the valence band and the conduction band for left and right circularly polarized light (σ^+ and σ^-). The numbers describe the relative transition probabilities.

the optical generation and investigation of spins in n-doped GaAs (n-GaAs) [14]. Since the selection rules are also true for the recombination of electrons with holes, a spin imbalance in the conduction band will generate circularly polarized light when recombining. This effect is exploited in the already mentioned Spin-LEDs, which were first used to demonstrate spin injection into GaAs. The different transition probabilities also build the basis for the optical detection of a spin accumulation in the conduction band, described in the next section.

2.1.1. Magneto-optic Kerr effect

The polar magneto-optic Kerr effect (pMOKE) is directly connected with the optical selection rules. It is used in this work to measure and image the spin polarization in the GaAs. The effect describes the polarization rotation of a linearly polarized laser beam after being reflected from the sample surface. For GaAs, a Kerr rotation occurs if an unequal occupation of spin up and spin down electrons in the conduction band exists. This imbalance, i.e. the difference of the chemical potential between spin up and spin down electrons, also called spin accumulation, is illustrated in Fig. 2.2 on the left hand side. The out-of-equilibrium state is described by the different Fermi energies for the spin up and the spin down subband. For photons with the energy close to the bandgap, only transitions into the spin down subband are possible. Due to the optical selection rules in GaAs as shown in the previous section, transitions into only one spin subband of the conduction band result in different absorption probabilities for left (lc)

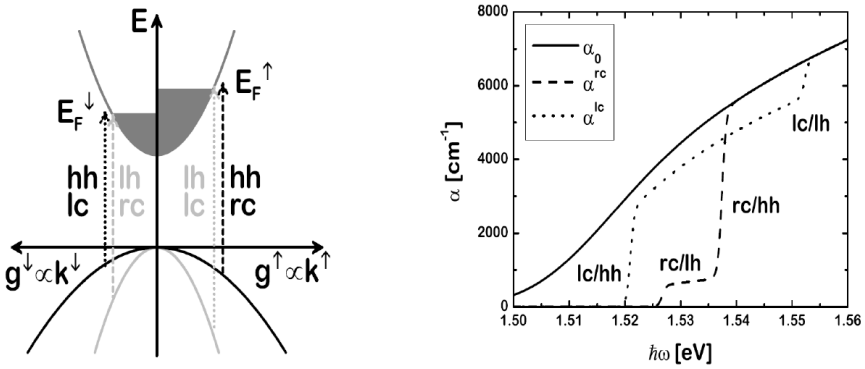

Figure 2.2.: Left: Illustration of a spin accumulation in the GaAs conduction band resulting in a different absorption edge for transitions of left (lc) and right circularly (rc) polarized light from the light (lh) and heavy hole (hh) band into each spin subband (from [15]). Right: Calculated absorption spectrum for $n^{\uparrow} = 1.5 \cdot 10^{17}\,\mathrm{cm}^{-3}$ and $n^{\downarrow} = 0.5 \cdot 10^{17}\,\mathrm{cm}^{-3}$ at 4.2 K. α_0 represents the absorption coefficient without spin accumulation (from [15]).

and right (rc) circularly polarized light. The resulting absorption coefficient for both helicities as a function of the photon energy is shown in Fig. 2.2 on the right hand side. The calculated curves nicely illustrate the four energy steps for the transitions from the light (lh) and heavy hole (hh) states into both spin subbands. Thus, depending on photon energy, the absorption coefficient differs for both helicities. From the absorption coefficient the corresponding refractive index can be calculated via the Kramers-Kronig transformation. The difference in the refractive index between lc and rc polarized light is finally proportional to the Kerr rotation, as shown for instance in the work of P. Kotissek [16].

Fig. 2.3 shows the spectral dependence of the Kerr signal calculated from the absorption coefficients illustrated in Fig. 2.2. The curve matches well with experimental results, as will be shown later. Important to note is the sign reversal in the Kerr spectrum between the pronounced maximum and minimum value. This shows that the photon energy plays a decisive role for the optical detection of a spin accumulation in GaAs. Experimentally, only one sign reversal of the Kerr rotation near the bandgap energy is usually visible (about 1.515 eV at 10 K).

Altogether, it is shown that a spin accumulation in the n-GaAs conduction band results in a Kerr rotation for photon energies close to the bandgap. For relatively small spin accumulations as in the here presented work, the Kerr rotation is proportional to the spin polarization or spin accumulation in the n-GaAs conduction band [15]. A nonlinear behavior between spin polarization and Kerr rotation occurs for spin polarizations above 20% in the conduction band, as shown in the work of M. Beck together with detailed calculations concerning the temperature,

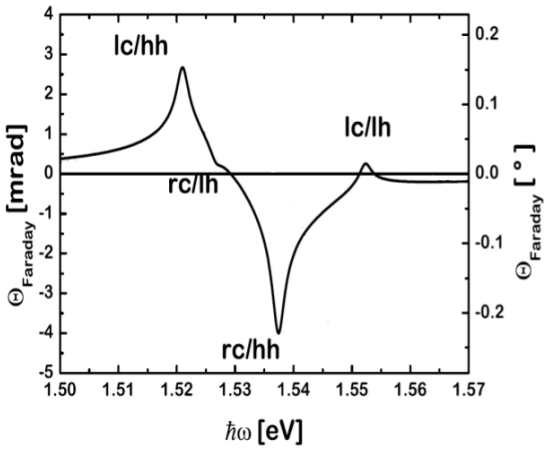

Figure 2.3.: Calculated Kerr rotation as a function of photon energy for a spin accumulation in GaAs, determined by $n^{\uparrow} = 1.5 \cdot 10^{17}\,cm^{-3}$ and $n^{\downarrow} = 0.5 \cdot 10^{17}\,cm^{-3}$ at 4.2 K (from [15]).

doping and wavelength dependence [15].

2.2. Spin relaxation in n-GaAs

Since an imbalance of spin up and spin down electrons in the GaAs conduction band is not the energetically favorable state, the question arises how long this imbalance persists (after switching off the spin generation source) and how the relaxation into an equilibrium state takes place. Depending on the active spin relaxation and spin dephasing mechanism, the spin accumulation relaxes or depolarizes within a characteristic lifetime or spin relaxation time τ_s. Usually one has to distinguish between the spin relaxation time T_1 and the spin dephasing time T_2. The spin dephasing time T_2, also called transversal relaxation time, describes the time until a spin ensemble oriented perpendicular to an external magnetic field dephases, e.g. due to slightly different Lamor frequencies. In contrast, the longitudinal relaxation time T_1 corresponds to the relaxation time for the spin component parallel to the external magnetic field. However, for n-GaAs and relatively weak magnetic fields, T_1 and T_2 are equal [13, 17]. Hence it is sufficient to only use one characteristic time τ_s.

Fig. 2.4 shows the spin lifetime in n-type GaAs as a function of doping density. Large spin lifetimes above 100 ns were found in GaAs at low temperatures for doping densities around $10^{16}\,cm^{-3}$, which is close to the insulator-metal transition at $n = 2 \cdot 10^{16}\,cm^{-3}$. Fig. 2.4 also illustrates the dominant spin relaxation mechanism depending on the carrier concentration. For low doping densities, this is mainly the hyperfine interaction, where donor-bound electrons interact with

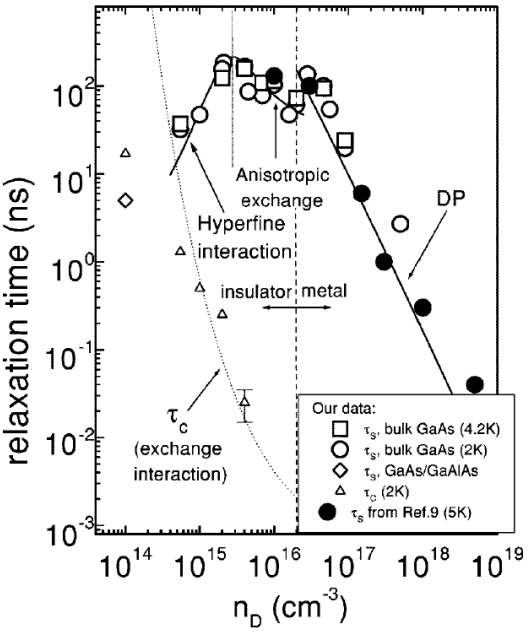

Figure 2.4: Dependence of the spin lifetime on doping density in n-GaAs at low temperatures (from [18]). Above the metal-insulator transition the D'yakonov-Perel' (DP) mechanism limits the relaxation time.

their surrounding randomly aligned nuclear spins. Around n = 10^{16} cm^{-3}, according to Dzhioev et al. [18], spin relaxation of the localized electrons is dominated by exchange interaction with neighboring electrons. Since a metallic behavior with large mobility is preferred for spin injection experiments, besides a large spin lifetime, all investigated samples in this work have doping densities above $2.5 \cdot 10^{16}$ cm^{-3}. For these doping densities above the insulator-metal transition, the D'yakonov-Perel' (DP) mechanism is dominant (see Fig. 2.4). The principle of this spin relaxation mechanism will be explained below.

Before introducing the D'yakonov-Perel' mechanism, it should be noted that other important spin relaxation processes exist. A complete overview is given elsewhere [13, 17, 19]. One of the important spin relaxation mechanisms worth mentioning is the Elliot-Yafet mechanism, which is based on momentum scattering. Due to spin-orbit coupling, electron states are mixtures of spin up and spin down states. Nevertheless, since spin-orbit coupling is usually weak, the electron states still have mainly spin up or spin down character. However, the small admixture of the opposite spin direction gives a probability to flip the spin at each momentum scattering event, resulting in spin relaxation. The Elliot-Yafet mechanism is most important in crystals with structural inversion symmetry as Si or Ge [19, Chap. B6]. In crystals without this symmetry as GaAs, this mechanism plays a negligible role.

2.2.1. D'yakonov-Perel' mechanism

In contrast to the other spin relaxation processes, the D'yakonov-Perel' mechanism actually leads to dephasing rather than relaxation. It is based on internal electric fields in the GaAs zinc-blende structure. Electrons moving through the crystal will experience this field Lorentz-transformed as a magnetic field. Thus, depending on size and direction of the electron wave vector k, an effective magnetic field appears and the electron spin will precess around this field axis. The dephasing due to the D'yakonov-Perel' mechanism arises then from momentum scattering. Electrons in the GaAs conduction band experience a different effective magnetic field when changing direction and hence have a different precession frequency and precession axis. The basic idea of this dephasing process is sketched in Fig. 2.5 on the left hand side.

The effective magnetic field can also be derived from spin-orbit coupling, which in fact is the consequence of relativistic effects. The GaAs conduction band can be modelled by the Hamiltonian [19, Chap. B6]

$$H = \frac{\hbar^2}{2m^*}k^2 + \frac{\hbar}{2}\vec{\sigma}\cdot\vec{\Omega}(\vec{k}). \tag{2.1}$$

The first part describes the parabolic band structure with effective mass m^*. The second term includes the spin via the Pauli matrix vector $\vec{\sigma}$. $\vec{\Omega}(\vec{k})$ can be viewed as the $\vec{k}$-dependent effective magnetic field. The resulting spin-splitting of the GaAs conduction band is shown in Fig. 2.5 on the right hand side. In bulk III-V semiconductors with zinc-blende structure, the effective magnetic field $\vec{\Omega}(\vec{k})$ is proportional to k^3 [19, Chap. B6]:

$$\vec{\Omega}(\vec{k}) = \frac{\alpha\hbar^2}{(2m^*E_g)^{1/2}}\left[k_x(k_y^2-k_z^2)\hat{x} + k_y(k_z^2-k_x^2)\hat{y} + k_z(k_x^2-k_y^2)\hat{z}\right] \tag{2.2}$$

Today, this is called Dresselhaus field or Dresselhaus effect. Here, α is a material-dependent parameter (for GaAs $\alpha = 0.07$), and E_g the semiconductor bandgap. Beside the k^3-dependence of the effective magnetic field, Eq. (2.2) also shows that the spin precession axis strongly depends on the wave vector direction. However, the efficiency of the resulting D'yakonov-Perel' mechanism relies on the momentum scattering time τ. Since the dephasing of a spin ensemble basically occurs during the precession between two scattering events, the mechanism is more effective the larger τ is. For small scattering times the precession angle between two scattering events becomes small and dephasing is suppressed due to the random changes that cancel each other. This effect is called motional narrowing, details are given in Ref. [17].

Despite the fact that the D'yakonov-Perel' mechanism is less effective with increasing scattering rate, Fig. 2.4 shows a drastic decrease of the spin lifetime in

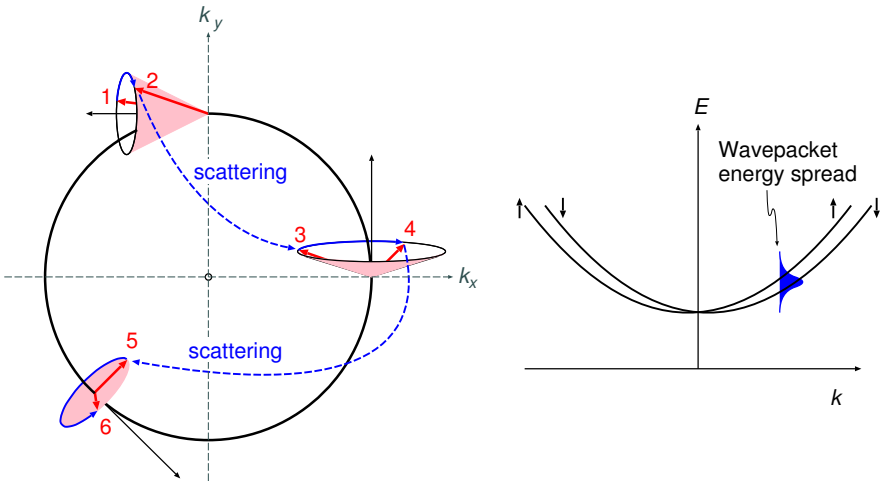

Figure 2.5.: Left: The D'yakonov-Perel' mechanism. Starting at position 1, an electron spin is precessing around the k-dependent effective magnetic field. After scattering from 2 to 3, the effective field changes and the spin starts to precess around a new axis (from [19, Chap. B6]). Right: Spin splitting of the GaAs conduction band due to spin-orbit coupling and the absence of space inversion symmetry (from [19, Chap. B6]).

n-GaAs with increasing doping density in the metallic regime above a doping density of $3 \cdot 10^{16}\,\mathrm{cm}^{-3}$. This is mainly due to the wave vector increase with increasing carrier density. Larger k-values enhance the dephasing mechanism due to the increased precession frequency (see Eq. (2.2)). In addition, the scattering time τ increases with increasing Fermi energy as explained in the next section ($\tau \propto E_F^{3/2}/n$) [13], which counters the decrease of τ with increasing doping density n. In general, the energy dependence of the D'yakonov-Perel' mechanism can be described with the following formula [13]:

$$1/\tau_s \propto \tau(E) \cdot E^3 \tag{2.3}$$

In the same manner the spin lifetime decreases with increasing temperature. However, only a weak temperature dependence was found below 50 K for metallic n-GaAs [7, 20]. In the low temperature regime the thermal energy is small compared to the kinetic energy of the electrons in the conduction band, as discussed in the next section.

2.3. Spin drift and diffusion

The behavior of a spin ensemble or a spin accumulation in the GaAs conduction band is naturally determined by the properties of the conducting electrons around the Fermi level. The mobility for instance describes the ability to accelerate these

electrons in electric fields. When applying an electric field E in the semiconductor, the average velocity (drift velocity) is defined by the mobility μ, not to be confused with the chemical potential introduced below:

$$v_d = -\mu \cdot E = -\frac{e\tau}{m^*} \cdot E \tag{2.4}$$

The mobility depends on the scattering time τ and the electron effective mass m^*. The fact that an electron ensemble travels with a constant drift velocity in an electric field is due to scattering that decelerates the ensemble. The scattering time τ or momentum-relaxation time is a property of the semiconductor and depends on the doping density, the temperature and the crystal purity. A general introduction for GaAs based semiconductors is given in the textbook by E. F. Schubert [21].

In the case of n-GaAs at low temperatures, the main scattering mechanism is ionized impurity scattering due to the strong coulombic interaction. The scattering mechanism strongly depends on the electron velocity. The faster the electron the shorter is the interaction time with the ionized impurity. Therewith, the deflection becomes weaker with increasing electron velocity. Since the electron velocity increases with temperature, the mobility (in case of ionized impurity scattering) has the following temperature dependence [21]:

$$\mu \propto T^{3/2} \tag{2.5}$$

This is directly connected with the temperature dependence of the spin lifetime shown in the previous section. However, for degenerately doped semiconductors, i.e. n-GaAs in the metallic regime, the Fermi velocity is larger than the thermal velocity at low temperatures ($\sim$10 K). Thus, the mobility is expected to remain almost constant in this temperature regime [21], where the velocity is defined by the Fermi energy and not the temperature. Nevertheless, the mobility, i.e. the scattering time increases with increasing electron energy which contributes to the strong energy dependence of the D'yakonov-Perel' mechanism discussed in Sec. 2.2.1.

In contrast to the directed motion of drift in an electric field, diffusion describes the random movement of electrons, which depends on their Fermi velocity v. This velocity randomly changes direction after the scattering time τ. Thus, in this simplified picture, the particle travels an average distance of $l = \tau \cdot v$ after changing its direction. The strength of electron diffusion is described by the diffusivity or diffusion coefficient [17]:

$$D = \frac{1}{2}\frac{l^2}{\tau} = \frac{1}{2}v^2\tau \tag{2.6}$$

The last term of Eq. (2.6) implies that the diffusivity is proportional to the scattering time, as the mobility is (see Eq. (2.4)). Hence, there is a direct relation

between mobility and diffusivity which is often called the Einstein relation:

$$\frac{eD}{\mu} = \frac{1}{2}mv^2 \tag{2.7}$$

For doping densities below the metal-insulator transition (nondegenerate electrons in the GaAs conduction band) the kinetic energy on the right hand side of Eq. (2.7) is given by the thermal energy $k_\mathrm{B}T$. In contrast, for doping densities above the metal-insulator transition (degenerate electron gas in the conduction band) the Fermi velocity v has to be used in Eq. (2.7). Since the doping densities used here are well above the insulator-metal transition, the samples consist of a degenerate electron gas in the GaAs conduction band.

In general, for a more accurate description of the electron behavior in the GaAs conduction band, the density of states $g(E_\mathrm{F})$ has to be taken into account, as the general form of Einstein's relation shows [17]:

$$\frac{eD}{\mu} = \frac{\mathrm{n}}{g(E_\mathrm{F})} \tag{2.8}$$

This equation enables the calculation of the diffusion constant via the mobility, which can be experimentally determined from resistance measurements. The electron density n in the GaAs conduction band can be well controlled by the doping density and is a very important parameter for the spin lifetime as shown in the previous section. However, the density of states at the Fermi energy is difficult to extract, especially for doping densities close to the metal-insulator transition. A rough empirical formula was estimated from low-temperature photo-luminescence measurements in n-GaAs for various doping densities. Fitting the data allows to describe the energy increase ΔE in the conduction band as a function of doping density n [22]:

$$\Delta E(\mathrm{n})[\mathrm{eV}] = 1.4 \cdot 10^{-8} \cdot \mathrm{n}^{\frac{1}{3}} \qquad \mathrm{n\ in\ [cm^{-3}]} \tag{2.9}$$

Alternatively, the GaAs conduction band can be approximated by a single-valley, isotropic and parabolic band. The Fermi energy increase due to the filling of the conduction band in a degenerately doped n-type semiconductor is then given by [21]:

$$\Delta E(\mathrm{n})[\mathrm{J}] = \frac{\hbar^2}{2m_e^*}(3\pi^2\mathrm{n})^{2/3} \qquad \mathrm{n\ in\ [m^{-3}]} \tag{2.10}$$

Eq. (2.9) and Eq. (2.10) can be used to estimate $g(E_\mathrm{F})$ in n-GaAs for the corresponding doping density by using the derivative of the inverse function $\mathrm{n}(\Delta E)$.

Since injected spins are carried by the conduction electrons, the presented equations also describe the drift and diffusion of spins. However, in contrast to the electron charge, spin is not conserved and decays by several mechanisms as shown

in the previous section. Thus, there is a characteristic decay length of a spin accumulation, the spin diffusion length

$$L_s = \sqrt{D \cdot \tau_s} \; . \tag{2.11}$$

It is determined by the spin lifetime and the diffusivity. For large spin diffusion lengths, either a large spin lifetime or a large diffusivity is necessary, i.e. a large Fermi velocity and long scattering times (see Eq. (2.6)). Interestingly, if the spin lifetime is limited by the D'yakonov-Perel' mechanism, the corresponding spin diffusion length does not depend on the scattering time τ [19, Chap. B6], since the influence of τ on D and τ_s cancels each other. Additionally, in the same manner, it was predicted that the spin diffusion length in n-GaAs with dominating D'yakonov-Perel' mechanism does not depend on temperature [13].

When an electric field is applied, a constant drift velocity can be ascribed to the spin ensemble. A superposition of electron drift and spin diffusion occurs, resulting in an effective spin relaxation length L_{eff}. L_{eff} depends on the spin diffusion length L_s and the spin drift length $L_d = v_d \cdot \tau_s$, which itself depends on the electric field induced drift velocity. A detailed derivation is given within the standard model of spin injection [17], which also includes the here used drift-diffusion model.

2.4. Spin injection into GaAs

The previous section has shown how spins distribute in the GaAs due to drift and diffusion. This section now generally introduces into the creation of spins in semiconductors by electrical spin injection from ferromagnets.

2.4.1. Conductivity mismatch

In principle, spin polarized currents in GaAs can be simply created by driving a current from a ferromagnetic material like Fe or (Ga,Mn)As into the GaAs. However, this may lead to a very poor spin polarization in the GaAs because of the so-called conductivity mismatch problem, which was first realized by Schmidt et al. [23]. One can demonstrate this problem in a simplified way with effective resistances, illustrated in Fig. 2.6.

Depending on the band structure and the density of states (DOS) at the Fermi energy, a metallic ferromagnet usually has different resistances in this two current model - for the spin up (majority) and the spin down (minority) channel. Thus, ferromagnets provide a natural source for spin polarized currents. In contrast, for

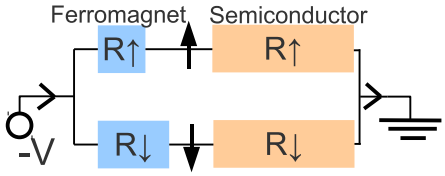

Figure 2.6.: Two current model with effective resistances for majority (up) and minority (down) spins. The corresponding resistance in both materials is illustrated by the different block widths.

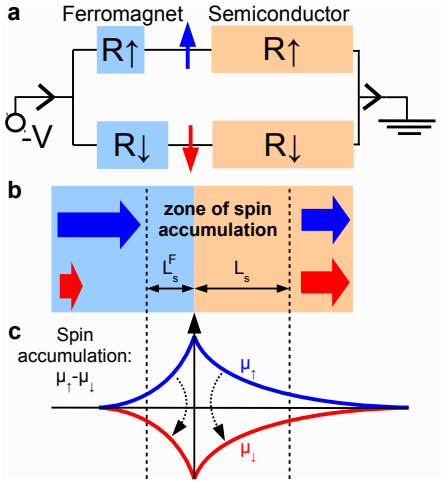

Figure 2.7: (a) Illustration of spin injection with the two current model and effective resistances. (b) Incoming spin polarized current transforms into an outgoing unpolarized current. (c) Creation of spin accumulation at the interface inducing spin relaxation and spin flip processes in both materials (adapted from [24]).

the semiconductor, the effective resistance for spin up and spin down electrons is equal. Furthermore, as in our case, the resistance of the n-GaAs is much larger than the resistance of Fe or (Ga,Mn)As. As a consequence, the total resistance of the spin up channel and the spin down channel is similar, i.e. the current polarization in this heterostructure is negligible (see Fig. 2.6). Details about this equivalent circuit of spin injection and the effective resistances are given elsewhere [17].

A closer look of what occurs with the spin polarized current from the ferromagnet when it is flowing towards the interface is shown in Fig. 2.7. First of all the spin-polarized current across the interface creates an accumulation of spins in the semiconductor. This spin accumulation can be described by the difference between the chemical potential for spin up and spin down ($\mu_s = \mu_\uparrow - \mu_\downarrow$). Since a spin imbalance in the GaAs is not energetically favorable and due to certain spin relaxation mechanisms (see Sec. 2.2), a transformation of majority spins into minority spins occurs in the zone of spin accumulation, resulting in an unpolarized current coming out of the semiconductor (see Fig. 2.7b). The zone of spin accumulation is determined by the spin diffusion length in both materials.

Without any interface resistance between the ferromagnet and the semiconductor, the spin imbalance in the semiconductor diffuses back into the ferromagnet.

In equilibrium, the absence of an interface resistance causes a continuity of the chemical potential across the interface (see Fig. 2.7c). Thus, the maximum spin accumulation at the interface not only depends on the spin lifetime in the semiconductor, it additionally depends on the spin relaxation rate in the ferromagnet. The decisive problem here usually is the much larger DOS in the metallic ferromagnet, i.e. the spin accumulation described by the chemical potential corresponds to a much larger amount of spin up electrons. Thus, even for similar spin lifetimes in ferromagnet and semiconductor, the amount of spin flips is significantly larger in the ferromagnetic region. As a result, the current already depolarizes in the ferromagnet before reaching the interface [25], and hence the whole spin accumulation is suppressed. The same effect occurs if the DOS in both materials is similar, but the spin lifetime is much shorter in the ferromagnet, e.g. for spin injection from (Ga,Mn)As into n-GaAs.

This shows that the conductivity mismatch is not only a problem of the different conductivities, it is rather the combination of the continuity of the chemical potential across the interface and the fact that there is a much larger spin flip rate in the ferromagnet. This is also relevant for efficient spin injection from the dilute magnetic semiconductor (Ga,Mn)As (see Sec. 2.6.1). A detailed derivation of this phenomenon can be found within the standard model of spin injection from Fabian et al. [17].

2.4.2. Tunnel barrier

A solution for the conductivity mismatch problem is the use of a tunnel barrier, which was first suggested in 2000 by Rashba et al. [26]. For Fe on GaAs the formation of a Schottky barrier can be used as a tunnel barrier. In a similar way an Esaki- or tunnel diode can be used for efficient spin injection from (Ga,Mn)As into GaAs. In both cases, the thickness of the barrier can be well controlled by the doping density in the GaAs, as will be shown in Secs. 2.5 and 2.6. For electrical spin injection it is favorable to have a narrow barrier, which enables large tunneling currents and thus reasonable spin accumulations.

Fig. 2.8 illustrates the two current model in a ferromagnet/semiconductor-junction consisting of a tunnel barrier at the interface which dominates the total resistance. The current polarization is now determined by the spin-dependent resistance of the tunnel barrier, arising from the band structure of ferromagnet and semiconductor (see Secs. 2.5.2 and 2.6.1). For the case shown in Fig. 2.8, the tunneling current is mainly carried by majority spin electrons. This generates a majority spin accumulation in the n-GaAs when injecting spins, i.e applying a negative voltage at the ferromagnet. If a positive bias voltage is applied at the ferromagnet, the flow of electrons is reversed. Assuming that the tunneling current is still

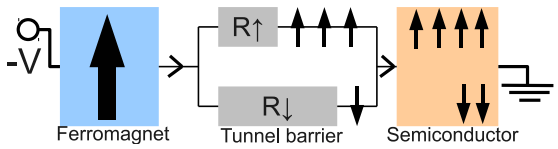

Figure 2.8.: Spin injection across a tunnel barrier where the spin dependent tunnel resistance determines the current polarization. Injection of majority spin electrons (indicated by the small black arrows) creates a majority spin accumulation in the semiconductor.

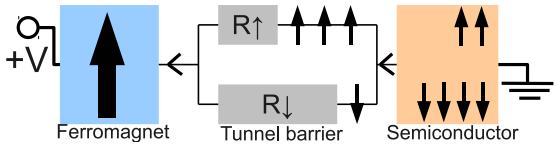

Figure 2.9.: Majority spin extraction across a tunnel barrier leads to a minority spin polarization in the semiconductor.

dominated by majority spin electrons leads to a minority spin accumulation in the semiconductor (see Fig. 2.9).

In summary, by reversing the bias voltage, which means going from spin injection to spin extraction, the spin polarization in the semiconductor is expected to be reversed, too.

2.4.3. Spin accumulation

The spin accumulation in a semiconductor at the interface with a ferromagnet resulting from a spin-polarized current is determined by [17]

$$\mu_s = P_j \cdot jR_N. \tag{2.12}$$

For spin injection through a tunnel barrier, the current polarization P_j is given by the spin-polarization of the tunnel barrier conductance P_Σ. The spin accumulation is then proportional to the current density j and the effective resistance of the nonmagnetic semiconductor $R_N = L_s \cdot \rho_N$, which is a product of the spin diffusion length times the resistivity. Besides the current density j which pumps spins into the semiconductor, the spin accumulation μ_s also depends on how fast the spins distribute and relax in the semiconductor. The maximum spin accumulation at the interface thus also depends on the scattering rate and the spin lifetime in the semiconductor.

2.5. Fe/n-GaAs Schottky contact

The previous section has shown that a tunnel barrier is necessary for the efficient injection of spins from a metallic ferromagnet into GaAs. In this work, spin injection from Fe and (Ga,Mn)As is investigated, where the tunnel barrier between the ferromagnet and the n-GaAs is created by a Schottky barrier or Esaki barrier, respectively. The formation of a Schottky barrier will be explained in the following. The same principles hold for the formation of an Esaki diode between (Ga,Mn)As and n-GaAs, which is shown in Sec. 2.6. In addition, spin-dependent tunneling from Fe into n-GaAs through a Schottky barrier will be addressed in this section.

A Schottky barrier is a potential barrier formed at a metal-semiconductor junction. Electrons from the metal have to overcome this barrier to get into the semiconductor, as well as electrons flowing from the semiconductor into the metal. For spin injection from Fe into GaAs, this barrier can be highly useful as explained in Sec. 2.4. The formation of such a barrier will be explained for now in a simple model of Schottky and Mott. A few enhancements for a better agreement with experimental results will be shown later in this section.

For the derivation the work function of metal and semiconductor has to be known, which defines the Fermi energy in both materials, here Fe and n-doped GaAs (n-GaAs). Fig. 2.10 shows on the left the energy diagram of Fe and n-GaAs without being in contact with each other. Upon connecting Fe and n-GaAs, electrons from the semiconductor flow into the metal until the Fermi level is balanced and no net current is present (see Fig. 2.10 right). However, a local charge density stays in the metal at the interface, and the missing electrons in the semiconductor generate a positive background charge. This generates an electric field close to the interface causing the upwards band bending in the semiconductor. In the simple case where the space-charge in the semiconductor only comes from the ionized donors, the resulting width W of the depletion zone decreases with increasing doping level N_D [21]:

$$W = \sqrt{\frac{2\epsilon_S \Phi_{SB}}{eN_D}} \tag{2.13}$$

Here, ϵ_S corresponds to the permittivity of the semiconductor (about $12.5 \cdot \epsilon_0$ for GaAs). Since the Fermi energy of Fe lies in the middle of the GaAs band gap, the Schottky barrier height $e\Phi_{SB}$ is about 0.7 eV.

Altogether, this simple model explains the principle of a Schottky contact very well. For Fe on n-GaAs the Schottky barrier height also matches with experimental results (0.6-0.8 eV). However, for other metals on GaAs, differences were found in Φ_{SB} with respect to the predicted barrier height (see Fig. 2.10). Indicated by numerous experiments, the difference of Φ_{SB} could be traced back to

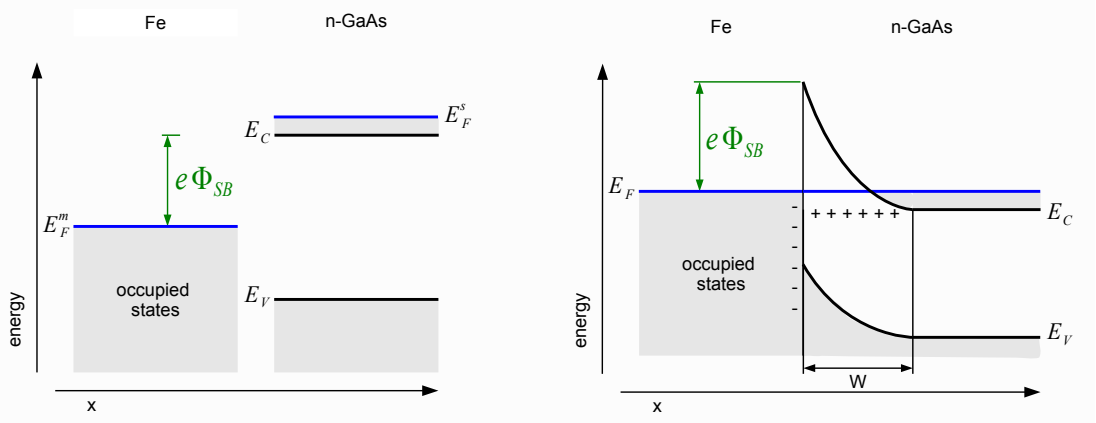

Figure 2.10.: On the left, the energy diagram of Fe and n-doped GaAs without being in contact with each other. The Fermi energy in Fe (E_F^m) lies in the center between the conduction- and the valence band edge E_C and E_V and determines the Schottky barrier height $e\Phi_{SB}$. The band bending and the local charge density after connecting are shown on the right.

metal-induced gap states at the interface, resulting in Fermi level pinning in the middle of the band gap [27]. To characterize transport over the Schottky barrier, the correct barrier height Φ_{SB} is highly important and decisive for current-voltage calculations.

2.5.1. Schottky contact under applied bias

When applying an external bias voltage V_b at the ferromagnet (see Fig. 2.11), the maximum band bending is modified to $(\Phi_{SB} - V_b)$. Thus, the width of the depletion layer W is also changed [27]:

$$W(V_b) = \sqrt{\frac{2\epsilon_S(\Phi_{SB} - V_b)}{eN_D}} \tag{2.14}$$

These changes are illustrated in Fig. 2.11(a) for a positive V_b, called forward bias, and in Fig. 2.11(b) for a negative V_b, called reverse bias.

Forward bias $V_b > 0$

A positive bias results in an electron current from the n-GaAs into the Fe (see Fig. 2.11(a)). Since electrons in the conduction band obey Boltzmann statistics, the number that is able to overcome the barrier exponentially increases with

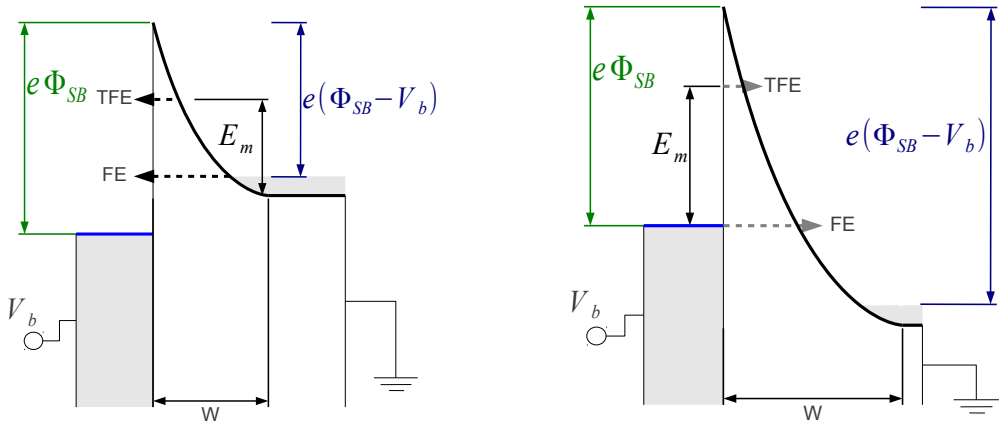

(a) forward bias $V_b > 0$ (b) reverse bias $V_b < 0$

Figure 2.11.: Schottky contact under applied bias. A consequence is the change of the band bending and the width of the depletion layer.

decreasing barrier height. This height is linearly lowered by a forward bias. Thus, the current-voltage characteristic in forward direction ideally is [27]:

$$I(V_b) = I_0(\mathrm{e}^{eV_b/k_\mathrm{B}T} - 1) \tag{2.15}$$

Equation (2.15) is only true when tunneling through the barrier can be neglected. This is the case for a large barrier width W or at high temperatures, where thermionic emission dominates the characteristic. In this regime, the width of the depletion layer W has no influence on the current.

However, at low temperatures and for sufficiently thin barriers, the major contribution to the current is due to electrons tunneling directly from the conduction band of the semiconductor into the metal. The current-voltage characteristic of this process was investigated by Padovani and Stratton [28]. The consideration was done for two regimes, for low temperatures where the tunneling mainly occurs at the Fermi level, called field emission (FE), and for intermediate temperatures, where most of the electrons tunnel at an energy E_m above the Fermi level, called thermionic field emission (TFE). The achieved equations are based on the I-V relationship for an arbitrary potential barrier, where only the first terms of the Taylor expansion were considered. This equation was then applied to the shape of a Schottky-barrier with its dependence on doping level and voltage as explained above. In addition to the mentioned approximations, the image force correction is neglected as well in this consideration. The resulting current-voltage characteristic basically describes an exponential increase of the current with increasing bias voltage. For not too high doped semiconductors, the function can be used to fit parameters of the Schottky contact, e.g. the doping density N_D in the GaAs as shown in Refs. [16] and [29].

Reverse bias $V_b < 0$

For electrical spin injection, the transport characteristic in this direction is decisive. In contrast to a forward bias where spins are extracted out of the GaAs, a reverse bias does not lower the barrier height. Instead, electrons from the metal experience a thinner barrier under reverse bias (see Fig. 2.11(b)). The current-voltage characteristic of electrons tunneling through the barrier can be described after Padovani also by an almost exponential increase of the current with increasing bias voltage [30]. However, for larger doping densities used in this work the I-V characteristics becomes almost ohmic, as shown later.

2.5.2. Spin-dependent tunneling

The realization of a tunnel barrier for efficient spin injection from Fe into n-GaAs has been shown in the previous section via a Schottky barrier. Beside the tunnel barrier, another key ingredient for efficient spin injection is the band structure of both materials, ferromagnet and semiconductor, and the role of band symmetries. Calculations have shown that the symmetry matching of the wavefunctions is decisive for the tunneling probability through a GaAs barrier [31]. This can be understood in terms of the complex band structure of GaAs shown in Fig. 2.12 on the left. The imaginary part describes the exponential decay of an incoming wavefunction corresponding to evanescent states close to the semiconductor surface.

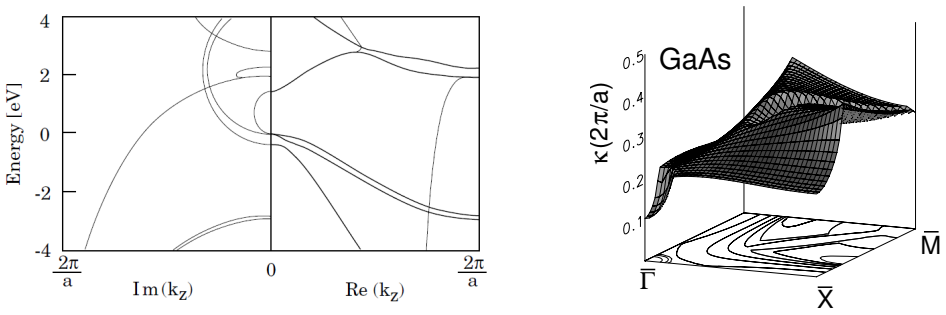

Figure 2.12.: Left: Complex band structure of GaAs (from [32]). Right: Illustration of the decay paramater κ as a function of $\vec{k}_{\|}$ with its minimum at $\vec{k}_{\|} = 0$ corresponding to the $\bar{\Gamma}$-point (from [33]).

In general, the electron wavevector $\vec{k}$ can be separated into components parallel and perpendicular to the interface between ferromagnet and semiconductor ($\vec{k}_{\|}$ and k_z). For perfect crystal structures and interfaces, $\vec{k}_{\|}$ is preserved during the tunneling process. Only the perpendicular component $k_z = q + i\kappa$ is complex within the barrier, where κ describes the decay parameter of the wavefunction

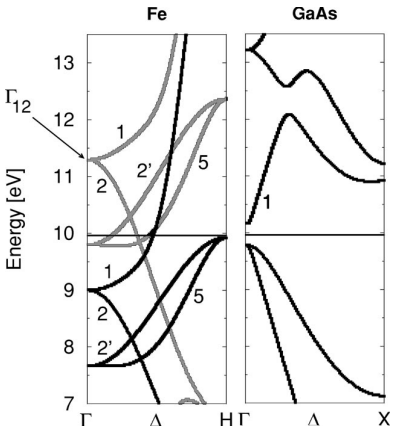

Figure 2.13: Band structures along (001) for Fe and GaAs around the Fermi energy. Grey lines correspond to minority spin bands, black lines to majority spin bands. The numbers represent the symmetries of the (001)-direction Δ (from [31]).

[34]. In case of a Schottky barrier between Fe and n-GaAs, the Fermi level lies in the GaAs bandgap (see previous section). The states at the ferromagnet's Fermi level thus couple to the complex band within the GaAs band gap. Important for tunneling are the symmetry properties of these states which may be different for the majority spin bands and the minority spin bands.

In Fig. 2.12 on the right, κ is plotted as a function of $\vec{k_{\|}}$ for an energy in the middle of the band gap. As expected, the states with $\vec{k_{\|}} = 0$, i.e. electrons under normal incidence will farther penetrate into the GaAs. However, since the amount of states with nonzero $\vec{k_{\|}}$ is much larger, they still can have a large contribution depending on the barrier thickness [33].

For large barriers, the tunneling current is mainly carried by states having the smallest imaginary part κ. This corresponds to the small loop in the GaAs band structure shown in Fig. 2.12 connecting the valence band with the conduction band. Now the symmetry of these states is decisive in order to see which states from the ferromagnet can couple to them and hence dominate tunneling.

Fig. 2.13 shows the spin-resolved band structure of bulk Fe and bulk GaAs for k-vectors normal to the GaAs(001) interface. For Fe, the black lines correspond to majority spin bands and the gray lines to minority spin bands, while the numbers denote the band symmetry. The slowest decaying states in the GaAs barrier have Δ_1 symmetry. In Fe, there are three bands crossing the Fermi energy with different symmetries. It is important to note that the symmetry notations for Fe and GaAs belong to different groups, namely C_{4v} for Fe and C_{2v} for GaAs. However, only the states with Δ_1 symmetry couple well with the conduction band of the GaAs [35]. Thus, the GaAs barrier acts as a strong spin filter, favoring the majority spins with Δ_1 symmetry. Based on the complex band structure and the wavefunction symmetries, a current polarization of 99% was predicted for spin injection from Fe into GaAs(001) through a Schottky barrier [31]. A detailed description of the calculations can be found in Ref. [35], where the authors also state that interface states or intermixing decreases the tunneling polarization.

Experimentally, current polarizations only in the order of 10% were observed at low temperatures [36]. A larger spin polarization of 32% was found later in Spin-LED experiments with an Fe/AlGaAs Schottky barrier [37]. Majority spin injection from an FeCo contact also resulted in a large current polarization up to 30% [12]. Recently, even sign reversals of the spin polarization with varying bias voltage were found for an epitaxial Fe contact on GaAs(001) [38]. This subject will be addressed in Sec. 4.1.3 in more detail together with the bias dependence of electrical spin injection from Fe into n-GaAs.

2.6. (Ga,Mn)As/n-GaAs Esaki diode

Before focusing on spin-dependent tunneling through the Esaki barrier, the ferromagnetic semiconductor (Ga,Mn)As will be briefly introduced. (Ga,Mn)As is a dilute magnetic semiconductor (DMS) which shows ferromagnetism for a large enough concentration of Mn atoms replacing the Ga atoms in the crystal. The discovery of ferromagnetism in (Ga,Mn)As was presented in 1996 with a Curie temperature T_C of about 60 K [39]. Since the distance of the randomly distributed Mn atoms is relatively large, ferromagnetism in (Ga,Mn)As is not based on direct exchange coupling. In contrast, the ferromagnetic order arises from a indirect exchange interaction via the induced hole carriers in the valence band. In that case, holes mediate the spin-correlation between the localized magnetic moments of the Mn atoms. This indirect exchange coupling is substantially weaker than the direct exchange coupling for example in Fe, which qualitatively explains the relatively low T_C in (Ga,Mn)As. The Curie temperature is basically limited by the maximum possible p-doping with Mn on Ga sites. So far, Curie temperatures around 190 K could be realized [5, Chap. 19]. Details about the origin of ferromagnetism and the influence of Mn on the GaAs band structure are discussed elsewhere [40]. A recent introduction into magnetic semiconductors including (Ga,Mn)As is given in Ref. [5, Chap. 19].

An Esaki diode or tunnel diode describes a semiconductor p-n junction where tunneling between the valence band of the p-type semiconductor and the conduction band of the n-type semiconductor is possible. This was first shown by Esaki in 1958 with a Ge-based p-n junction [41]. Tunneling also occurs when (Ga,Mn)As is grown on highly n-doped GaAs. Since Mn^{2+} replaces the Ga^{3+} ion in the GaAs crystal, Mn acts as an acceptor and thus donates a hole. Due to the relatively large Mn concentration of about 5.5% for the investigated samples, the (Ga,Mn)As layers consist of a large hole concentration in the order of $10^{20}\,\mathrm{cm}^{-3}$ [42] and the Fermi energy lies in the valence band of the (Ga,Mn)As [40].

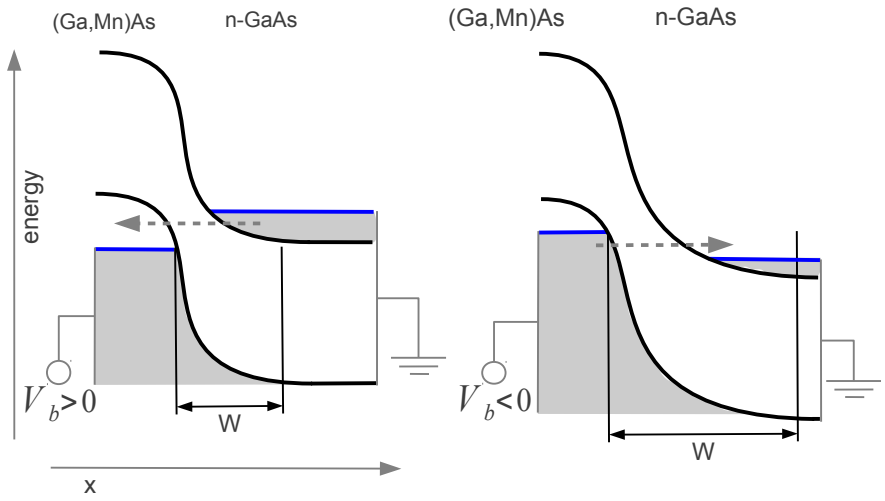

Figure 2.14.: Esaki diode in forward (left) and reverse direction (right) illustrating the band-bending and the depletion width W in the n-GaAs.

When connecting the (Ga,Mn)As with the n-GaAs, electrons from the n-GaAs conduction band flow into the (Ga,Mn)As valence band until the Fermi level is balanced across the junction. As for the Schottky barrier described above, the space-charge region builds up an electric field causing band bending in the heterostructure. Fig. 2.14 illustrates the energy diagram of an Esaki diode under forward (left) and reverse bias (right). In contrast to Fe having the Fermi energy in the middle of the GaAs bandgap (see Fig. 2.10), the difference in Fermi energy between (Ga,Mn)As and n-GaAs is in the order of the bandgap, i.e. about 1.52 eV at cryogenic temperatures. Compared to the Fe/n-GaAs Schottky contact, more electrons need to move from the n-GaAs into the (Ga,Mn)As until the Fermi energy is balanced. As a consequence, band-bending on the GaAs side is more pronounced as for Fe on GaAs. Since the effective p-doping in (Ga,Mn)As is one order of magnitude larger than the n-doping on the GaAs side, band-bending in the (Ga,Mn)As is relatively weak (see Eq. (2.13)). Therefore the above presented formulas for the Schottky barrier can be used to calculate the depletion zone in the n-GaAs (see Eq. (2.14)), only the barrier hight $e\Phi_{SB}$ has to be adapted to the GaAs bandgap.

2.6.1. Spin-dependent tunneling

Spin injection from (Ga,Mn)As into GaAs by interband tunneling from the valence band of (Ga,Mn)As into the conduction band of n-GaAs was first shown by Kohda et al. in 2001 [43]. In 2004, a large current polarization of about 80% was obtained for such heterostructures by measuring the circular polarization

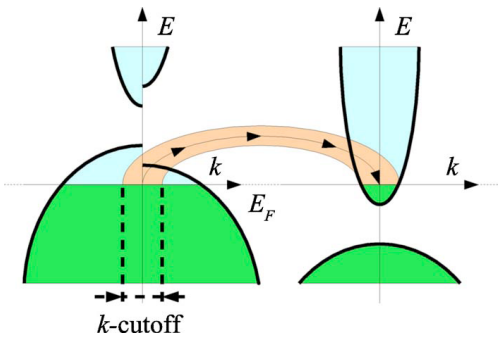

Figure 2.15.: Sketch of the tunneling process from the (Ga,Mn)As valence band into the n-GaAs conduction band (from [46]).

from a (Ga,Mn)As based Spin-LED [44]. Recently, Ciorga et al. demonstrated electrical injection and detection with a current polarization of 50% [45]. These observations demonstrate that (Ga,Mn)As in conjunction with an Esaki diode is a well suited spin injector material and provides a large current polarization. A further advantage of (Ga,Mn)As is the possibility to integrate it in GaAs based heterostructures with epitaxial growth. The growth conditions of (Ga,Mn)As on GaAs are described in Sec. 3.1.2. However, the disadvantage of (Ga,Mn)As compared to Fe as injector material is the low Curie temperature, which is still below room temperature.

A theoretical model for spin-dependent tunneling through the Esaki barrier was developed by Sankowski et al. [46]. As for the calculation of Fe/n-GaAs shown before, a conservation of the in-plane wave vector $\vec{k}_{\|}$ was assumed. The tunneling process is sketched in Fig. 2.15. In the low bias limit, the total current is dominated by states near the Γ-point, i.e. under normal incidence. This is, because for small biases, $\vec{k}_{\|}$ also has to match the small $\vec{k}_{\|}$ values in the conduction band of n-GaAs, which is indicated in Fig. 2.15. However, the calculations also show a strong anisotropy of the tunneling polarization as a function of the in-plane wave vector. Depending on the hole concentration in the (Ga,Mn)As layer, larger in-plane wave vectors are responsible for the high tunneling polarization. The reverse bias dependence was calculated in a previous publication [47], matching well with the experimentally observed decrease of current polarization with increasing negative bias voltage.

3. Methods

In this chapter the measurement principle and the sample geometry will be introduced. In the present work experiments on spin injection and spin accumulation in GaAs were mainly investigated by pMOKE measurements at the cleaved edge of the sample. This technique was first demonstrated by Kotissek et al. in 2007 [12]. The advantages of this method will be explained in Sec. 3.2 after describing the film growth and the sample preparation. The third section then discusses the observed depth range of this optical detection technique and the influence of the incident light on the electronic properties in the n-GaAs. Finally, the Hanle measurement principle will be explained which is important for the estimation of the spin lifetime.

3.1. Film growth

In this section the film growth of the studied samples will be described. Different samples with Fe and (Ga,Mn)As as ferromagnetic injector material were investigated within this work, grown on GaAs layers with a special doping profile. Since the doping profile and the layer thickness slightly differ from sample to sample, both will be listed together with the experimental results in Chap. 4. The general layer stack, however, is similar for all samples.

The semiconductor layers were grown by Martin Utz in the group of Prof. D. Bougeard. All layers were grown by molecular beam epitaxy (MBE) on undoped (semi-insulating) GaAs(001) substrates. The general procedure was as follows: First of all, the oxide from the GaAs surface was removed by annealing in UHV[1]. After that, in order to clean and flatten the GaAs(001) surface for epitaxial growth, a 300 nm thick GaAs layer was grown at temperatures above 620 °C. The subsequent GaAs layers are relevant for spin injection and were grown at temperatures of about 620 °C. First, the n-GaAs layer where spin accumulation takes place was grown on the undoped GaAs buffer layer. The thickness of this Si-doped layer was usually 1 µm, which was adjusted to the laser spot diameter for the optical measurements of the spin polarization. Wafers with a thicker n-GaAs layer up to 4 µm were also investigated. For the maximum spin lifetime

[1] ultrahigh vacuum

in the n-GaAs layer, a doping density close to the metal-insulator transition was chosen for most samples, i.e. $n \approx 2.5 \cdot 10^{16}\,cm^{-3}$ (see Sec. 2.2).

On top of the n-GaAs layer a 15 nm thick transition layer $n \rightarrow n^{++}$ was grown with a gradual increase of doping density followed by a n^{++}-GaAs layer with a doping density of $4 - 6 \cdot 10^{18}\,cm^{-3}$ and a thickness between 8 and 15 nm. The large doping density is crucial for the formation of a narrow tunnel barrier between the ferromagnetic material and the n-GaAs (see Sec. 2.5). Consequently, the thickness of the n^{++}-GaAs layer should be similar to the width of the depletion zone for the corresponding doping density (see Eq. (2.13)).

3.1.1. Fe/GaAs

For the growth of Fe on the n^{++}-GaAs layer, it was necessary to transfer the samples into another MBE system after the semiconductor growth. In previous spin injection experiments done by P. Kotissek the samples had to be transferred in atmosphere into a metal MBE system. Therefore, the samples were capped with an arsenic layer in order to protect the n^{++}-GaAs layer from oxidation. After removing the As capping layer in the metal MBE system by annealing ($\sim 300\,°C$), FeCo and Au could be epitaxially grown on the n^{++}-GaAs [16].

In order to circumvent this critical sample transfer, a transportable metal MBE system was modified within this work. This MBE chamber could be directly connected to the semiconductor MBE chamber, enabling sample transfer under UHV conditions. Hence, after the semiconductor film growth, the samples could be directly transferred into the metal MBE chamber without the need of an arsenic capping layer. There, 2-3 nm of Fe were deposited on the n^{++}-GaAs layer at room temperature. Since the magnetic anisotropy of Fe on GaAs(001) changes with Fe thickness [48], it was important to limit the thickness of the Fe layer to about 3 nm. This guarantees a magnetic easy axis along the [110] direction which is convenient for the optical detection on the cleaved edge, as will be shown later. Finally a Au layer (5 nm) was grown in order to prevent the Fe from oxidation. A photo of the MBE system when connected to the semiconductor MBE chamber can be found in the appendix.

3.1.2. (Ga,Mn)As/GaAs

For the samples with (Ga,Mn)As as injector material no transfer into a second MBE system was necessary. The ability to grow (Ga,Mn)As layers is integrated in the semiconductor MBE chamber. The growth was also done by Martin Utz. For the investigated spin injection samples a Mn concentration of about 5.5% was chosen. This corresponds to a Curie-temperature of $\sim 50\,K$. Usually, 50 nm

of $Ga_{95}Mn_5As$ were grown at relatively low temperatures of 240 °C (with respect to the GaAs growth temperature at 600 °C) on the n^{++}-GaAs layer. In order to prevent back-diffusion of manganese into the GaAs, a 2.2 nm thick $Al_{36}Ga_{66}As$ layer was added in between the n^{++}-GaAs and the (Ga,Mn)As layer. The scope of these samples was not a maximum Curie-temperature, rather reproducible growth conditions and a high quality interface with epitaxial growth. A detailed introduction into the semiconductor MBE system and the growth conditions of (Ga,Mn)As is given in the work of M. Utz [42].

3.1.3. Optical access to the cleaved edge plane

After the layer growth contacts were defined on the sample by standard optical lithography or e-beam lithography, Ar ion milling and a wet etching technique. Details about the contact geometry are given for each sample in the corresponding section of Chap. 4. Finally, for the optical measurements, the samples were cleaved across the ferromagnetic contact pads. For that purpose a small scratch was made at the border of the sample with a diamond cutter. This scratch had to be along the natural breaking axis of GaAs, that is [110] or [1-10]. By slightly applying a pressure from the rear side, the sample breaks along the crystallographic axis and provides a perfect flat cleaved edge plane (see Fig. 3.1). This enables a direct optical access to the n-GaAs channel even beneath the ferromagnetic contacts.

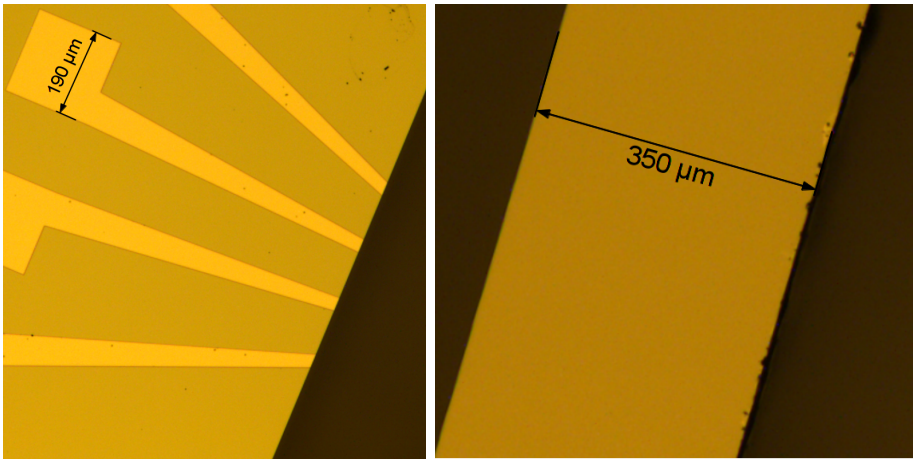

Figure 3.1.: Light microscope pictures of a simple sample design with 4 Au/Fe contacts from top view (left) and of the cleaved edge plane (right). There the left edge corresponds to the sample surface.

The position of the diamond cutter could be well adjusted under a microscope so that an accuracy of ±10 µm could be achieved. Since the magnetic easy axis of

the Fe samples is along the [110] direction, the samples with Fe were cleaved along the [1-10] direction. Thus the (110) surface is exposed and the polar magneto-optic Kerr effect on the cleaved edge is sensitive to the [110] direction. Hence, the remanent magnetization of the Fe layer already aligns the injected spins along the measuring axis [110] as illustrated in Fig. 3.2. In contrast, for (Ga,Mn)As, the magnetic anisotropy is more complex depending on growth properties, temperature and a patterning induced magnetic anisotropy [49, 50]. The different contributions may result in a tilted remanent contact magnetization with respect to the measurement geometry. The influence on the experimental results will be discussed later in Sec. 3.5.

3.2. Experimental setup

For the optical detection of the spin polarization in GaAs, a scanning Kerr microscope was constructed within this work. A sketch of the measurement principle and the sample geometry is shown in Fig. 3.2.

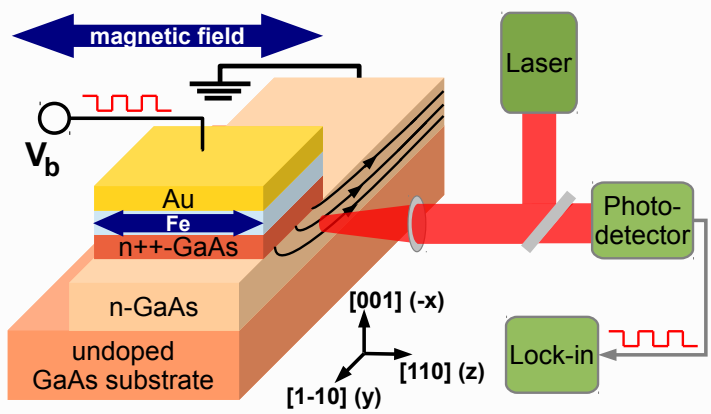

Figure 3.2.: Measurement principle and sample geometry.

The probe laser beam is shining under normal incidence on the cleaved edge of the sample. Thus, by scanning across the cleaved edge plane along the n-GaAs channel the distribution of the spin accumulation can be observed. The working principle of the polar magneto-optic Kerr effect (pMOKE) in GaAs was already explained in Sec. 2.1.1. One of the advantages of the cleaved edge detection is the possibility to observe the injected spin polarization without applying an external magnetic field. For Fe the injected spins are already aligned with the axis of the laser beam for pMOKE measurements, as denoted by the solid blue arrow in Fig. 3.2 which indicates possible directions of the remanent Fe magnetization. In other approaches, when measuring pMOKE at the sample surface [38, 51],

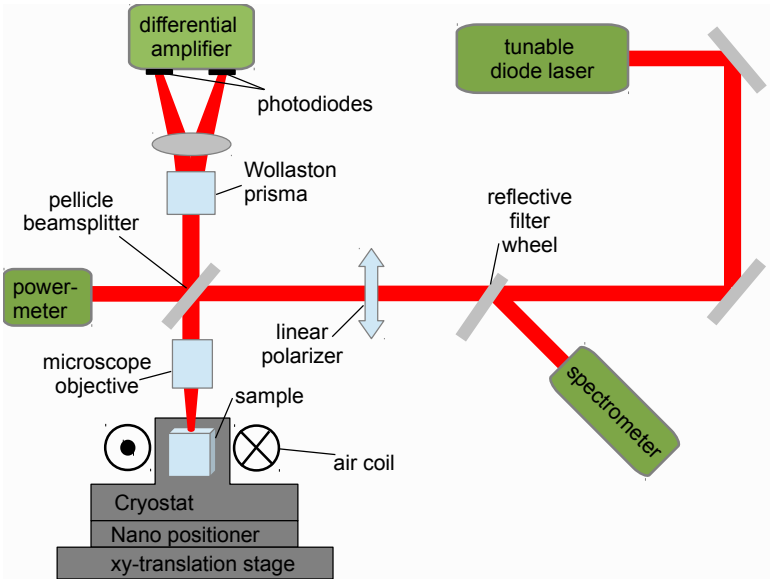

Figure 3.3: Schematic of the scanning Kerr microscope illustrating the essential components for the detection of the spin polarization in GaAs.

an external magnetic field was necessary to rotate the spins in the out-of-plane direction which does not allow measurements in the remanent state.

Another advantage of this measurement geometry is the ability to observe the spin polarization even below the ferromagnetic contacts. This is a unique feature of this imaging technique that proved to be very helpful for a better understanding of spin injection and the distribution of spins in the n-GaAs channel, as demonstrated in the next chapter. In addition, by means of this method, a new and efficient way for the optical generation of spins in semiconductors could be established as shown in Sec. 4.3.

A schematic representation of the optical setup is given in Fig. 3.3. A photo of the setup can be found in the appendix. For the optical measurements the sample is mounted in a He flow cryostat where silver conductive epoxy is used to glue the sample on the cold finger. The cryostat itself is mounted on top of a nano positioner, thus two-dimensional scans can be performed by moving the sample under the static laser beam. The nano positioner allows to move in the x- and y-direction within a range of 100 µm and an accuracy better than 100 nm. In addition, a movement range of 20 µm in z-direction is given. For pMOKE measurements a tunable diode laser (Toptica DL pro) with a wavelength range from 810 to 860 nm was used. This corresponds to a photon energy between 1.53 eV and 1.44 eV. It allows to adjust the wavelength to the GaAs bandgap in order to maximize the Kerr rotation (see Sec. 2.1.1). The diode laser has a typical linewidth of 100 kHz and a maximum output power of 80 mW. The axis of the linearly polarized light is defined by a Glan-Thompson polarizer. An uncoated pellicle beamsplitter is then used to reflect 8% of the linearly polarized light on the microscope objective. The objective has a magnification factor of

60, corrections for the coverglass of the cryostat and a working distance of about 2.5 mm. The z-component of the electron spin polarization in the n-GaAs channel is then detected via pMOKE by splitting the reflected laser light from the sample with a Wollaston prism into two orthogonal linearly polarized beams on two balanced photodiodes. The difference signal of the two diodes representing the Kerr rotation is then amplified by a factor of 10^6.

For the measurements a square-wave bias voltage alternating between zero and V_b is applied between two ferromagnetic contacts and the Kerr rotation is detected synchronously with a lock-in technique (see Fig. 3.2). Thus, the spin accumulation in the n-GaAs is modulated, which ensures that the (quasistatic) magnetization of the ferromagnetic contacts does not contribute to the Kerr signal. In addition, magneto-optical effects in the cryostat window or the objective induced by the external magnetic field are not detected as well.

The Kerr rotation angle in the n-GaAs, θ_K, versus the magnetic field applied along the [110] direction (z-direction) is shown in Fig 3.4 for spin injection from a (Ga,Mn)As contact. The resulting hysteresis loop reproduces the magnetiza-

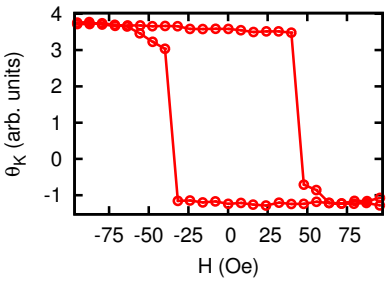

Figure 3.4: Kerr rotation in the n-GaAs channel versus applied magnetic field along z-direction for electrical spin injection from a (Ga,Mn)As contact.

tion curve of the contact. Thus, due to the modulation technique mentioned before, the observation of a hysteresis curve is a direct proof for a spin-polarized current from the ferromagnet into the n-GaAs. The exact correspondence between the magnetization loop of the ferromagnetic contact and the spin density in the n-GaAs has been proven earlier by Kotissek et al. for an FeCo contact [12]. The same correspondence for an (Ga,Mn)As contact will be corroborated by the switching field observed in the electric detection of the spin accumulation discussed in Sec. 4.3 (see Fig. 4.24).

However, as plotted in Fig 3.4, the signal of the hysteresis loop is not symmetric around zero Kerr rotation. This means, due to the modulation of the injection current, that an offset Kerr rotation arising from electro-optic effects is usually observed [52]. However, the pure spin signal can be extracted from the height of the hysteresis loop. In this manner, to eliminate any electro-optic background, the measurements presented in Chap. 4 were performed in remanence after saturation along [110] and [-1-10], respectively and only the difference between both remanent values was used as a measure of the spin polarization in the GaAs

layer. This value is strictly proportional to the spin accumulation in the n-GaAs at the laser spot position. It is also labeled as θ_K in the following, since only the electro-optic offset signal was removed.

The magnetic field in z-direction for the magnetization reversal of the ferromagnetic contacts (see Fig. 3.2) is created by an air coil that is placed outside the cryostat. The sample affixed to the cold finger is in the center of this air coil as illustrated in Fig. 3.3. In addition a Helmholtz coil is attached to the air coil that allows to apply a magnetic field along the x-axis, necessary for Hanle measurements (see Sec. 3.5).

3.3. Depth of pMOKE detection

The previous section has shown the advantages of the optical detection at the cleaved edge. This section now discusses the penetration depth of the incident laser beam in the n-GaAs. Fig. 3.5 illustrates the absorption coefficient in n-GaAs as a function of the photon energy for a doping density of $n \approx 10^{16}\,\mathrm{cm}^{-3}$. For pMOKE measurements, as explained in Sec. 2.1.1, the photon energy of the linearly polarized laser beam must be close to the absorption edge of the n-GaAs (about 1.515 eV at 10 K). Fig. 3.5 shows the strong variation of the absorption coefficient in this regime. For photon energies below 1.52 eV ($\approx 816\,\mathrm{nm}$) the absorption coefficient falls below $0.5 \cdot 10^4\,\mathrm{cm}^{-1}$, corresponding to a penetration

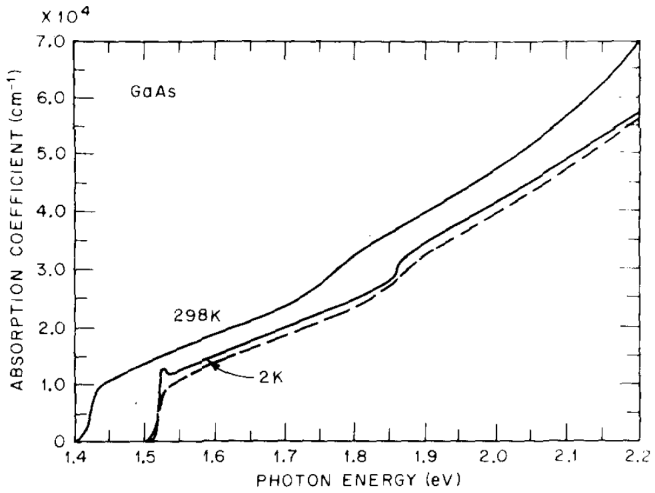

Figure 3.5.: Photon energy dependence of the absorption coefficient for n-GaAs with a doping density around $10^{16}\,\mathrm{cm}^{-3}$ (from [53]). The dashed line describes the absorption spectrum measured at room temperature but shifted by +95 meV.

depth[2] of 2 µm. The penetration depth rises dramatically with increasing wavelength until the absorption becomes zero for photon energies below the GaAs bandgap. Interference effects can appear for a large penetration depth due to back-reflections at the border of the n-GaAs channel. Thus, depending on the depth of the n-GaAs layer in z-direction (see Fig. 3.2), smaller wavelengths are more suitable for the optical detection on the cleaved edge.

Besides interference effects, the penetration depth is important for two other reasons. On the one hand a depletion zone in the n-GaAs layer exists due to Fermi level pinning of the air-exposed GaAs(110) surface in the center of the bandgap [54]. For the used doping densities above $n = 2.5 \cdot 10^{16}\,cm^{-3}$ the resulting width of the depletion zone is in the oder of 200 nm or below (see Eq. (2.13)). Within this region no charge carriers are available. Consequently no current is flowing and no injected spin accumulation builds up in this zone. For probing the spin polarization in the n-GaAs layer at about 10 K, wavelengths between 816 and 819 nm were used where the penetration depth and therefore the detecting depth range is between 2 and 10 µm. Therefore, the penetration depth of the light is significantly larger than the depletion zone at the n-GaAs surface. Hence, for the analysis of the experimental data it can be simply ignored. On the other hand the penetration depth is important for the estimation of the absorbed laser power density and the resulting influence on the GaAs electronic system. This is discussed in the next section.

3.4. Absorbed laser power

In this section the absorbed laser power in the GaAs and the influence on the electronic system will be estimated. The latter of course depends on the absorbed laser power, but also on the penetration volume, i.e. the penetration depth and the spot size of the laser beam. Since the incident light is used for probing the spin polarization, the influence on the material should be as low as possible. Experimentally, a good signal to noise ratio for pMOKE measurements was obtained with an intensity in the order of 12 µW and a spot size of about 1 µm diameter.

First of all, in order to estimate the absorbed power density the spot size is important. It can be determined by scanning the laser beam in x-direction across the sample edge while detecting the reflected light intensity (see measurement geometry in Fig. 3.2). This linescan is illustrated by the red curve in Fig. 3.6. The derivative of this curve gives the laser spot profile with a full width at half maximum (FWHM) of 1.04 µm, as shown by the green curve in Fig. 3.6.

[2]The penetration depth corresponds to the reciprocal absorption coefficient.

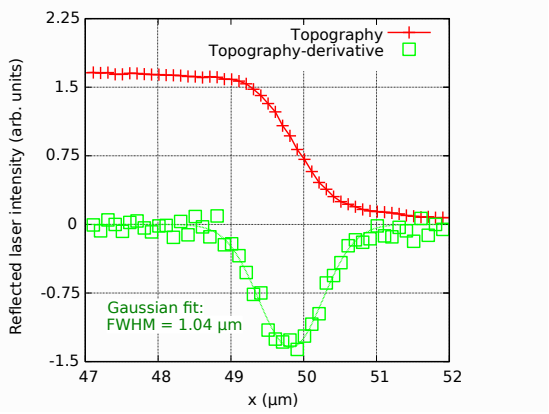

Figure 3.6.: Linescan of the reflected laser intensity across the sample edge (x-direction). The derivative of the topography gives the laser spot profile.

Due to the refractive index of about 3.5 for GaAs at low temperature and photon energies close to the bandgap [55], 31% of the incoming laser intensity is reflected under normal incidence. The penetration depth of the transmitted 69% of the incident light strongly depends on the wavelength with respect to the n-GaAs bandgap as shown before [53]. Therewith the penetration depth can easily vary between 1 µm and 100 µm within a few nm change of the wavelength. For a rough estimation of the absorbed power density a wavelength of 819 nm with a penetration depth of about 10 µm is chosen. In order to calculate the absorbed laser power density the transmitted light has to be normalized to the spot size area of 1 µm diameter. Assuming that 50% of the laser intensity is located within the FWHM of the two-dimensional Gaussian spot profile results in an absorbed power density in the order of $5\,\mu W/\mu m^2$. For 10 µm penetration depth, the average volume density of the absorbed power is in the order of $0.32\,\mu W/\mu m^3$.

The absorbed laser energy generates electron-hole pairs in the GaAs and thus additional electrons in the conduction band. The recombination lifetime in the n-GaAs is about 100 ps (for $n = 1.5 \cdot 10^{16}\,cm^{-3}$ at 10 K [56]). In equilibrium between generation and relaxation, the additionally generated electron density in the conduction band is given by

$$N = \frac{G}{1.51\ \text{eV}} \cdot 100\ \text{ps}. \tag{3.1}$$

For an absorbed power density G of $0.32\,\mu W/\mu m^3$, this results in an electron increase of about $1.3 \cdot 10^{14}\,cm^{-3}$. This rough estimation shows that the electron increase in the conduction band should be well below 1% with respect to the doping density. Experimentally no influence on the spin density distribution could be observed with this laser power. Also for larger laser intensities, no significant change in the spin density distribution occurred. However, the increase

of the electron density in the conduction band with increasing laser power can be observed in the Kerr spectrum, which is shown later in Sec. 4.3.

3.5. Hanle effect

Hanle measurements have been shown to be very useful as an additional proof for spin injection into semiconductors and for the estimation of the spin lifetime. The measurement principle corresponds to the depolarization of spins when applying an external magnetic field aligned perpendicular to the injected spin direction. Thus, an injected spin ensemble is forced to precess around this field during its lifetime. When measuring the spin polarization at a certain distance from the continuously injecting contact, one therefore collects spins in a broad time of flight range and thus with different precession angles, arising from the diffusive transport. This is sketched in Fig. 3.7 by two spin paths between the ferromagnetic contact in the middle and the red circle which represents the laser spot that observes the local spin polarization. By sweeping the external magnetic field indicated by the blue arrow, a Lorentzian shaped curve of the spin polarization can be observed at the laser spot position as shown in Fig. 3.7 on the right hand side. The spin lifetime is basically determined by the width of the Hanle curve. The larger the spin lifetime the narrower is the Hanle lineshape. This can be qualitatively understood by taking into account the average time of flight of a spin ensemble. With increasing spin lifetime the average time of flight increases, and hence the time under the influence of the external magnetic field increases. Thus, lower magnetic fields are necessary in order to observe the same precession angles of the injected spins at the point of detection. Consequently the depolarization curve becomes narrower.

For most cases the description of spin dynamics can be simplified by a model with diffusive transport along a one-dimensional channel. In general, the z-component of the spin density at a distance y from the point of spin injection can be described by [17]

$$S_z(y,t) \sim \frac{1}{\sqrt{4\pi Dt}} e^{-(y-v_d t)^2/4Dt} e^{-t/\tau_s} \cos(\omega_0 t). \tag{3.2}$$

Here, v_d describes the drift velocity, D the diffusivity and τ_s the spin lifetime. The external magnetic field B is included in the Lamor frequency $\omega_0 = \frac{g\mu_B}{\hbar} B$, where the g-factor is fixed at -0.44 for n-GaAs. Since spins are injected continuously, the function has to be integrated over all transport times t in order to count all electrons reaching the detection point at position y. For fitting the experimental data with this one-dimensional model an analytic solution of the problem can be

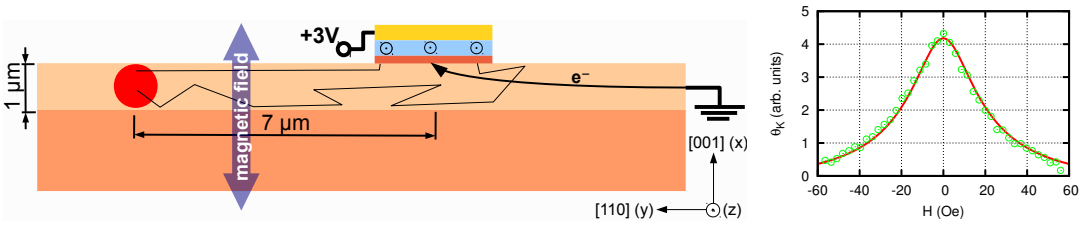

Figure 3.7.: Left: Hanle measurement geometry - the red circle represents the laser spot position for the pMOKE measurement while spins are extracted from the ferromagnetic contact which is biased at +3 V relative to the reference contact on the right. Right: Hanle measurement showing the Lorentzian lineshape of the spin polarization as a function of the magnetic field in x-direction. Red curve illustrates the fitted function with a spin lifetime of about 25 ns.

used, derived in Ref. [17] (Eq. II.239, P.617):

$$S_z(y) = J_0 \cdot e^{-\alpha_1 y/L_s} \cdot \left[\frac{2\kappa + \alpha_1}{(2\kappa+\alpha_1)^2 + \alpha_2^2} \cos\left(\frac{\alpha_2}{L_s} y\right) - \frac{\alpha_2}{(2\kappa+\alpha_1)^2 + \alpha_2^2} \sin\left(\frac{\alpha_2}{L_s} y\right) \right]$$
$$\alpha_1 = \frac{1}{\sqrt{2}} \sqrt{1 + \kappa^2 + \sqrt{(1+\kappa^2)^2 + (\omega_0 \tau_s)^2}} - \kappa$$
$$\alpha_2 = \mathrm{sgn}(\omega_0) \frac{1}{\sqrt{2}} \sqrt{-1 - \kappa^2 + \sqrt{(1+\kappa^2)^2 + (\omega_0 \tau_s)^2}} \tag{3.3}$$

Here, $L_s = \sqrt{D \cdot \tau_s}$ describes the spin diffusion length, $\kappa = \frac{v_d \cdot \tau_s}{2L_s}$ the ratio of drift to diffusion, and J_0 a scaling factor that was used as a fitting parameter. For Hanle measurements performed on the diffusion side, i.e. left of the ferromagnetic contact as illustrated in Fig. 3.7, no electron drift is present in the one-dimensional case and $\kappa = 0$ can be used. In addition, to take into account the width of the contact and hence all possible injection-detection distances, the fitting function must be numerically integrated over the contact width. The 1 µm wide laser spot is small compared to the contact width and hence can be neglected. Since the spin diffusion length L_s can be independently extracted from linescans along the n-GaAs channel without external magnetic field, the spin lifetime τ_s is the only remaining fitting parameter beside the scaling factor J_0. Numerically fitting the measured $S_z(y)$ curve, therefore, provides a convenient way to determine the spin lifetime in the n-GaAs.

3.5.1. Magnetic anisotropy

The analytic solution shown in Eq. (3.3) is based on spin injection at $y = 0$ with spins pointing in z-direction. However, for (Ga,Mn)As, due to a superposition of different magnetic anisotropies, an in-plane tilt of the magnetization with respect

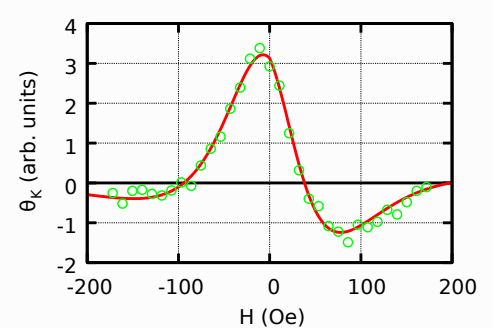

Figure 3.8.: Hanle measurement with an in-plane tilt of the magnetization of the injecting contact with respect to the z-axis. The red curve illustrates the fitted function $S(\phi, y)$ with a magnetization tilt $\phi = 23°$.

to the laser beam axis has to be considered. The complex magnetic anisotropy in (Ga,Mn)As leads to reorientation of the easy axis with varying carrier concentration and temperature. Since all measurements are performed in remanence, the magnetization of the injecting contact is aligned along the magnetic easy axis which may have a certain angle ϕ with respect to the z-axis. For Hanle measurements, due to the tilted magnetization, the injected spins either start to precess into the laser beam axis or away from it, depending on whether a positive or negative magnetic field in x-direction is applied. This must result in asymmetric Hanle curves when detected by pMOKE, which is experimentally observed for (Ga,Mn)As contacts, where a patterning induced anisotropy [49, 50] relevant for narrow contacts also comes into play.

Fig. 3.8 shows an example for an asymmetric Hanle curve. Due to the tilted magnetization of about 23° (from fit, see below) the maximum Kerr rotation is not observed at zero magnetic field but slightly shifted to about -10 Oe. At this magnetic field value the average precession angle of the injected spins counters the initial in-plane tilt of 23° and hence the z-component of the spin polarization is maximized. The larger the magnetization tilt, the more asymmetric is the Hanle curve in this measurement geometry. In a special case with a magnetization tilt of 90°, where the initial spin direction is perpendicular to the z-axis, a point symmetric Hanle curve without Kerr rotation at zero magnetic field would be observed.

In order to describe the data points in Fig. 3.8, also the analytic solution of the y-component of the spin polarization is required, which is also derived in Ref. [17] (Eq. II.238):

$$S_y(y) = J_0 \cdot e^{-\alpha_1 y/L_s} \cdot \left[\frac{2\kappa + \alpha_1}{(2\kappa + \alpha_1)^2 + \alpha_2^2} \sin\left(\frac{\alpha_2}{L_s} y\right) + \frac{\alpha_2}{(2\kappa + \alpha_1)^2 + \alpha_2^2} \cos\left(\frac{\alpha_2}{L_s} y\right) \right] \tag{3.4}$$

Since the analytical solution relies on spin injection at $y = 0$ with spins pointing in z-direction, the magnetization tilt can be considered by assuming to probe the projected spin polarization along the tilted direction, i.e. using $S(\phi, y) = \cos(\phi) \cdot S_z(y) + \sin(\phi) \cdot S_y(y)$ as fitting function. Therefore, with the combination of both components the function for each in-plane direction can be expressed and ϕ can be used as an additional fitting parameter. The red curve in Fig. 3.8 illustrates the fitted function $S(\phi, y)$ with a magnetization tilt $\phi = 23°$. Details on this sample are discussed later in Sec. 4.1.4.

3.5.2. Influences on Hanle lineshape

The value of the spin lifetime in GaAs is often extracted from Hanle curves obtained from non-local voltage measurements or by optical means using the one-dimensional spin drift-diffusion model described above [38, 45, 57, 58]. In order to extract the correct spin lifetimes from Hanle lineshapes with the above formulas in Eq. (3.3) and Eq. (3.4), the correct distance to the injecting contact and the exact spin diffusion length are crucial. In addition, other influences on the Hanle lineshape need to be ruled out:

Beside the magnetization tilt of the injecting contact, parasitic contributions such as dynamic nuclear polarization (DNP) have to be taken into account, where a large magnetic field arises from polarized nuclear spins, induced by the injected electron spins through hyperfine interaction [59]. The effect of DNP at low temperatures should be avoided by fast periodic magnetization reversal of the injecting contact [60]. This also applies to the experiments presented here since the external magnetic field and injected spin polarization are switched fast (2-3 Hz) compared to the nuclear spin relaxation time (10 min) [61]. The influence of DNP on the Hanle lineshape, that in general enhances depolarization, was already discussed elsewhere [58, 62, 63].

In addition, the influence of the out-of-plane magnetic field on the contact magnetization needs to be considered. This is determined by the magnetic anisotropy of the thin (Ga,Mn)As or Fe layer. For thin layers of Fe on GaAs the shape anisotropy creates a hard magnetic axis along the out-of-plane direction with an anisotropy field of $4\pi M_s = 21\,\text{kOe}$. Correspondingly, in Spin-LED experiments a magnetic field of about 20 kOe was necessary to saturate the Fe magnetization in the out-of-plane direction [64]. For (Ga,Mn)As, where the magnetization is two orders of magnitude smaller compared to Fe ($\sim 20\,\text{G}$ vs. $1700\,\text{G}$ [65]), the shape anisotropy is proportionately weaker. However, since (Ga,Mn)As grows compressively strained on GaAs(001) it exhibits a strong perpendicular magnetic anisotropy which favors an in-plane magnetization [39]. Hanle experiments on similar samples as used in Sec. 4.1.4 with a 20 nm thick (Ga,Mn)As layer have

shown that the magnetization rotation in the out-of-plane direction becomes visible for magnetic fields above 700 Oe [45, 66]. For other samples with a 50 nm thick (Ga,Mn)As layer magnetic fields between 1.5 and 3 kOe are necessary for a significant out-of-plane magnetization [67]. Thus, for the relatively small magnetic fields in Hanle measurements used in this work (<180 Oe), the influence on the contact magnetization is negligible.

Furthermore, the injected spins may be affected by magnetic stray fields in the GaAs arising from the ferromagnetic contact. However, this influence is not significant for smooth interfaces, especially for (Ga,Mn)As with its small magnetization, since the stray field decays within a few nm [68]. In contrast, is has been shown for rough interfaces that the injected spin accumulation in the semiconductor can be slightly depolarized due to magnetic stray fields [69]. The initial spin polarization in the semiconductor could be recovered in this work by applying an external magnetic field along the contact magnetization in order to suppress spin precession about the stray fields. This so called inverted Hanle effect could not be observed in the work presented here, indicating a smooth interface between semiconductor and ferromagnet. The inverted Hanle effect corresponds to the measurement geometry for the observation of hysteresis curves as shown for instance in Fig. 3.4. If the injected spin polarization was depolarized due to stray fields, the Kerr rotation would not be constant before and after the magnetization reversal.

Spin-orbit effective fields from the Dresselhaus-effect (see Sec. 2.2.1) may also influence the Hanle lineshape. On the one hand the Dresselhaus term is responsible for spin relaxation via the D'yakonov-Perel' mechanism, on the other hand it can cause a net spin precession if spin-polarized electrons are drifting along a crystal direction with a nonzero effective magnetic field, e.g. the [110] or [1-10] direction. However, for the samples used here a spin precession length in the order of centimeters can be expected from this effect [15]. Since Hanle measurements are usually observed in a distance of a few µm to the injecting contact, this effect is not relevant.

Altogether, the present measurement geometry and measurement principle should allow to extract correct spin lifetimes from Hanle lineshapes. However, in some cases the one-dimensional model is not sufficient to describe the spin density distribution along the n-GaAs channel. Thus, in order to extract the correct spin lifetimes from Hanle data, a two-dimensional model has to be used. This influence had not been considered so far and is discussed in detail in Sec. 4.2.

4. Experimental results

In this chapter the experimental results will be discussed. The results are starting in Sec. 4.1 with a qualitative comparison between different injector materials as Fe and (Ga,Mn)As, focusing on the bias dependence and the different spin density distributions in the n-GaAs channel. The next section then shows that a more complicated spin density distribution can also occur due to a nonuniform current density in the n-GaAs channel. In Sec. 4.3, a novel method for the efficient generation of spins will be presented, the spin solar cell effect together with the spin photodiode effect. In addition, experiments on thermal spin injection were performed and are discussed in Sec. 4.4, together with the attempt to optically observe spin pumping into GaAs. Finally the first optical results for electrical spin injection into a two-dimensional electron gas are demonstrated and analyzed in Sec. 4.5.

4.1. Fe and (Ga,Mn)As as injector materials

Electrical spin injection from Fe and (Ga,Mn)As into n-GaAs will be demonstrated in this section by pMOKE measurements on the cleaved edge. For these first experiments a simple contact design was chosen. On the one hand, this minimizes the influence of patterning processes, on the other hand the results are comparable to previous results from Kotissek et al. in 2007 [12, 16], where FeCo was used as injector material. The subject of this section was published in Journal of Applied Physics 109, 07C505 (2011) [70]. Therefore parts of this section directly reproduce our publication from April 2011.

4.1.1. Sample preparation

For the Fe and (Ga,Mn)As sample standard proceedings with optical lithography were used to define the contact pads. The process steps were performed partly in the yellow room of Prof. C.H. Back and in the clean room of Prof. D. Weiss.

The sample with Fe consists of a 4 µm thick n-GaAs layer for the electron transport and spin accumulation (nominal doping density $n = 2 \cdot 10^{16}\,cm^{-3}$). Between

the n-GaAs layer and the 2 nm thick epitaxial Fe(001) layer a 15 nm thick transition layer $n \rightarrow n^{++}$ and a 15 nm n^{++}-GaAs layer for the creation of a narrow Schottky barrier were grown (see Sec. 2.5). For the contact patterning, a photoresist was first spun on the cleaned surface of the Au covered Fe/GaAs sample. The exposure to light was done with a mask-aligner in order to define the contact pads. After developing the photoresist the contact areas were uncovered. 150 nm of Au were then deposited on the sample. After the lift-off process the evaporated Au layer was only left on the exposed areas defined by the mask. The thin MBE-grown Au and Fe layer on the remaining area was then removed with Ar ion etching. After that, chemical etching with acetic acid was used to remove the n^{++}-GaAs layer and the transition layer to confine the electron transport to the n-GaAs layer. To ensure a complete removal of the highly doped GaAs, 50 nm of the n-GaAs layer were removed, too. The chemical wet etching also reduces the damage at the contact edges from ion sputtering, which was shown by Spitzer et al. with citric acid [71].

The (Ga,Mn)As sample was grown by Martin Utz and prepared by Andreas Einwanger. The 3 µm thick n-GaAs channel has a nominal doping density of $4 \cdot 10^{16}\,\mathrm{cm}^{-3}$. For the creation of the Esaki diode (see Sec. 2.6) a 15 nm thick transition layer $n \rightarrow n^{++}$ and a 8 nm n^{++}-GaAs layer were grown between the n-GaAs and the 20 nm thick $Ga_{95}Mn_5As$ layer. Details on growth conditions are given in Sec. 3.1.2. Spin injection on similar samples has already been investigated in electrical detection [45,66], where a Curie temperature of about 65 K was found for the (Ga,Mn)As layer. The contacts were defined by optical lithography as shown above for the Fe sample. Since the (Ga,Mn)As samples are not covered with Au, the wet etching technique could be directly used after the evaporation of the Au pattern. As for the Fe sample, etching was stopped in about 50 nm depth of the n-GaAs layer.

4.1.2. Spin density distribution

Both samples were finally cleaved across the ferromagnetic contact pads, which enabled a direct optical access to the n-GaAs layer (see Sec. 3.1.3). The optical measurements on the cleaved edge were done at 10 K using a wavelength of 819 nm. The measurements were carried out in remanence after magnetic saturation along the z-directions [110] and [-1-10], respectively, and the difference between both remanent values was used as a measure of the spin polarization in GaAs, as described in Sec. 3.2.

Fig. 4.1 shows two-dimensional scans of the Kerr rotation in the n-GaAs, illustrated as a color coded map for the injection and the extraction case from a (Ga,Mn)As contact. The top panel in Fig. 4.1 illustrates the spin density distribution in the n-GaAs channel for electrical spin injection, i.e. a negative bias

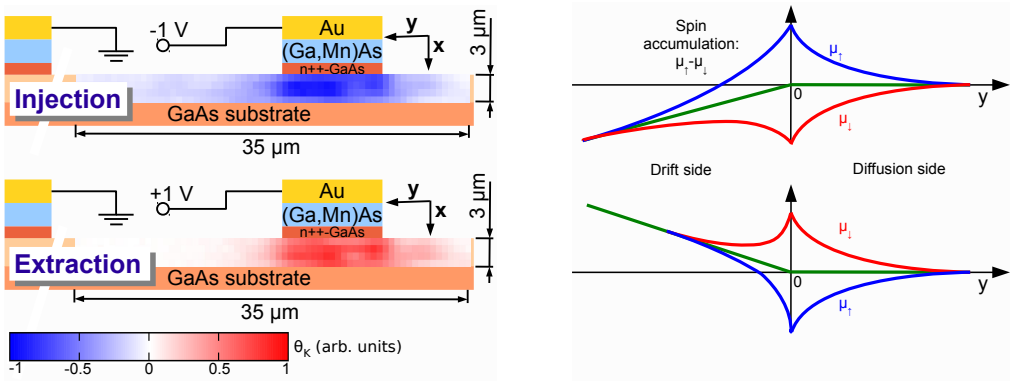

Figure 4.1.: Left: Two-dimensional scans of the Kerr rotation in the n-GaAs channel, shown as a color coded map for spin injection and extraction from a $Ga_{95}Mn_5As$ contact. Right: One-dimensional model of the spin accumulation along the n-GaAs channel with a spin generating point contact at y = 0. The spin accumulation is defined by the chemical potential for spin up (blue) and spin down electrons (red) and describes an exponential decay on both sides of the contact. The green line illustrates the electric potential along the channel for spin injection (top) and extraction (bottom).

voltage was applied between the injecting (Ga,Mn)As contact and a second contact on the left hand side at a distance of 0.5 mm. The negative bias continuously drives the spin polarized electrons tunneling from the (Ga,Mn)As layer into the n-GaAs channel. The created spin accumulation at the interface then diffuses in all directions. The decay of the spin polarization in both directions away from the injecting (Ga,Mn)As contact can be well fitted with an exponential as shown in Fig. 4.2. Due to the applied bias voltage the decay to the left is a superposition of electron drift and spin diffusion. For a negative bias voltage, the electric field in the n-GaAs channel accelerates the injected spins towards the left resulting in an effective decay length L_{eff} of 6.5 µm for spin injection with $V_b = -1$ V. In contrast, no electric field is present on the right hand side of the contact. Thus, the spin diffusion length L_s can be extracted from the exponential decay to the right resulting in about 3.3 µm for this sample.

The bottom panel of Fig. 4.1 illustrates the spin density distribution for a positive applied bias voltage. There, majority spin electrons are extracted out of the n-GaAs leaving a minority spin accumulation behind. Due to the positive bias voltage the electrons are now flowing from the left into the (Ga,Mn)As contact. Thus, electron drift and spin diffusion are opposed to each other on this side of the contact, leading to a reduced spin decay length. On the right hand side of the contact where no electric field is present the decay is again determined by the spin diffusion length L_s. The spin density distribution for both cases shown in Fig. 4.1 can be well described with a one-dimensional model, since almost no variation of the spin accumulation along the x-direction in the 3 µm thick channel is visible. Fig. 4.1 illustrates on the right hand side the spin accumulation in a

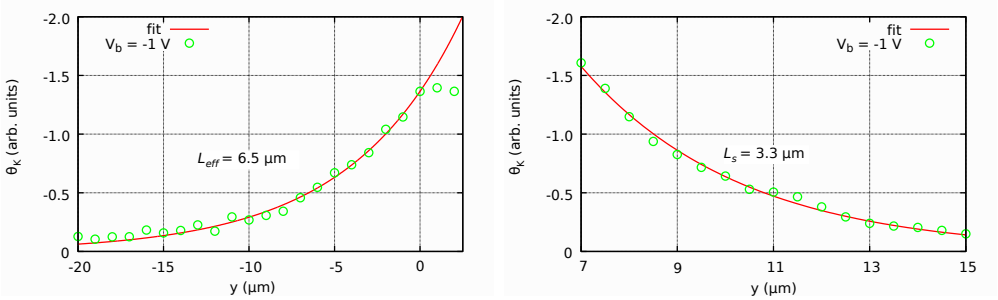

Figure 4.2.: One-dimensional linescan of the Kerr rotation along the n-GaAs channel for electrical spin injection ($V_b = -1\,V$) on the drift side left of the injecting contact (left) and on the diffusion side to the right of the contact (right). Exponential fit provides the effective decay length L_{eff} and the spin diffusion length L_s.

one-dimensional channel assuming a spin generating point contact at y = 0. As for the experiment shown on the left in Fig. 4.1, an electric field is assumed in the channel left to the contact due to the applied bias voltage, influencing the spin accumulation on this side of the contact.

Fig. 4.3 shows two-dimensional scans of the Kerr rotation with Fe as injector material, again for both, spin injection and extraction. Here, a significant difference can be observed in the spin density distribution compared to (Ga,Mn)As. While the spin polarization for the (Ga,Mn)As sample shows only slight variations below the contact for injection and extraction, the spin injection from Fe is mainly concentrated at the edge of the contact. A similar behavior was seen earlier for an FeCo contact [12]. Interestingly, spin extraction is even more confined to the Fe contact edge than injection and the spin polarization decays to a negligible value at about 10 µm from the edge below the contact.

The spatial spin density distribution for both contact materials can be qualitatively understood with the following assumptions:

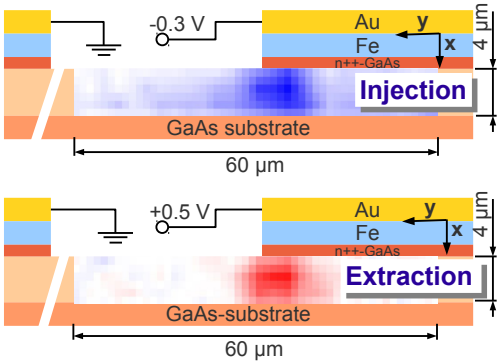

Figure 4.3.: Two-dimensional scans of the Kerr rotation in the n-GaAs channel, shown as a color coded map for spin injection and extraction from an Fe contact.

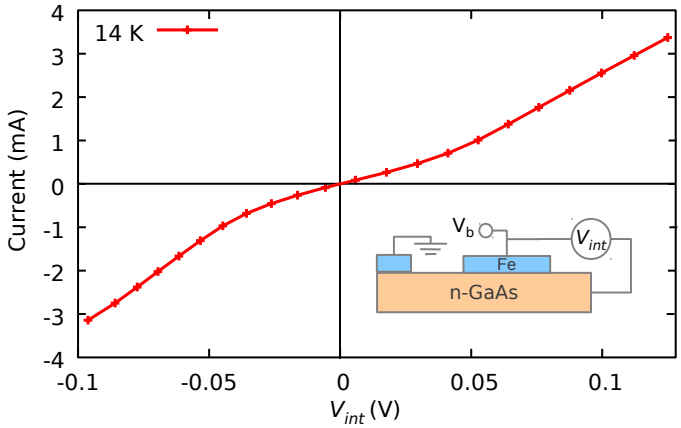

Figure 4.4.: *I-V* characteristic of the Schottky contact between Fe and n-GaAs.

1. the injecting contact represents an equipotential surface.

2. the voltage drop along the n-GaAs channel and the current density distribution are affected both by the channel resistance and the interface resistance.

For the (Ga,Mn)As sample the interface resistance is Ohmic and much larger than the channel resistance. As a consequence, the voltage drop and, hence, the current density j_x across the interface is essentially uniform along the channel. Thus, the current density j_y along the channel should increases from right to left below the contact. The spin density distribution results from the interplay between current density and spin relaxation. Experimentally, this leads to a nearly uniform spin density below the entire contact with a weak tendency to an increase from right to left as seen in Fig. 4.1 for spin injection.

In contrast, for the Fe sample (or FeCo sample in Ref. [12, 16]) the interface resistance of the Schottky barrier for a bias voltage of 0.5 V is of the same order of magnitude as the channel resistance. Therefore, the voltage drop across the metal/GaAs interface decreases from left to right and, due to the nonlinear I(V) characteristic of the Schottky contact, the current density and spin polarization show a drastic decrease away from the left contact edge. The *I-V* characteristic of the Schottky barrier is shown in Fig. 4.4, where the current is plotted against the voltage drop across the Schottky barrier V_{int}. The inset illustrates the measurement geometry. Since no current flows on the diffusion side of the n-GaAs channel right to the injecting Fe contact, V_{int} describes the potential drop across the Schottky barrier. V_{int} was measured while sweeping the bias voltage V_b used for the spin injection experiments shown in Fig. 4.3 from -0.5 V to 0.5 V.

The spin density distributions seen in Figs. 4.1 and 4.3 are of considerable relevance for spin injection experiments. For Hanle measurements the assumed

position of spin injection and the distance to the point of detection directly affects the extracted spin lifetime (see Sec. 3.5). In a non-local voltage geometry the effective distance between the injecting and the sensing contact may be different from the geometric contact pattern and shift with applied bias voltage. A unique feature of our imaging technique is the possibility to directly evidence the actual position of spin injection in such a case. The strong influence of the spin density distribution on the spin lifetime extracted from Hanle lineshapes is shown later in Sec. 4.2. There, two-dimensional simulations of the electron drift and spin diffusion were used to describe the spin density distribution in the n-GaAs channel and to extract the correct spin lifetime.

4.1.3. Bias dependence

The bias dependence of the injected spin polarization is shown in Fig. 4.5 for Fe (left) and (Ga,Mn)As (right). For (Ga,Mn)As the bias dependence was measured in the center below the contact (see Fig. 4.1) while for the Fe sample it was measured at the left edge of the contact (see Fig 4.3). Both graphs clearly show the expected sign reversal discussed in Sec. 2.4 when switching from spin injection (negative bias range) to spin extraction (positive bias range). In contrast to Fe as injector material, the bias dependence for the (Ga,Mn)As sample is almost symmetric. This behavior depends on the sample properties and is strongly connected with the band structure of (Ga,Mn)As and the band bending of the Esaki diode (see Sec. 2.6). (Ga,Mn)As samples with different interface properties and a strong asymmetric bias dependence will also be presented in the following sections. The flattening of the function with increasing positive or negative bias voltage shows the decrease of the spin injection efficiency, i.e. the decrease of the current polarization. This has been studied in detail by Ciorga et al. in 2009, using electrical detection in a non-local voltage geometry [45]. For a similar (Ga,Mn)As/n-GaAs heterostructure a current polarization of 50% was found, which also showed a decrease with increasing positive or negative bias voltage.

In 2007, majority spin injection into GaAs(001) from Fe epitaxial contacts has been observed [38], where a complex bias dependence of the injected spin accumulation was found changing from sample to sample. All samples showed an additional sign reversal of the spin polarization in the GaAs as a function of bias voltage indicating a sign reversal of the current polarization. It was suggested that surface bands are created by disorder from which the preferred extracted spin polarization is opposite to that from the bulk conduction band [72], or that the observed sign reversal results from an interface resonant band which strongly contributes to the tunneling conductance [73]. However, the fact that no sign reversal of current spin polarization was seen by Kotissek et al. [12] for injection

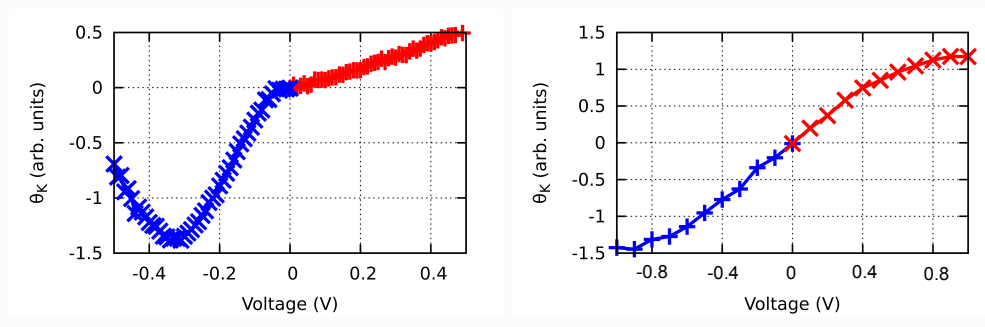

Figure 4.5.: Comparison of the bias dependence of the injected spin polarization below the contact for Fe/n-GaAs (left) and (Ga,Mn)As/n-GaAs (right).

from an epitaxial FeCo contact raised the question whether the different behavior was due to the larger band filling expected for bcc FeCo compared to bcc Fe, or due to interface-related electronic states. Since the present results for an Fe contact as seen in Fig. 4.5 show a similar behavior as for the FeCo contact, showing only the expected sign reversal at zero voltage when switching from spin injection to spin extraction, the different band filling can not be the main reason for the different behavior found in Refs. [12] and [38]. Instead, this indicates that the metal/GaAs interface resulting from the particular sample preparation conditions plays a decisive role. The strong influence of the interface between Fe and GaAs was confirmed by Schultz et al. in 2009 by studying the effect of growth and annealing temperature on the sign of the injected spin polarization [74]. Their Spin-LED experiment showed that the current polarization differs with varying growth temperatures and can even be reversed by post-growth annealing. In 2011, a comparison between spin injection from Fe and FeCo into n-GaAs directly showed that an additional sign reversal of injected spin polarization with bias voltage can occur for both injector materials [75]. Only a slight shift in the detected spin accumulation as a function of applied bias voltage was visible between both injector materials in this experiment.

Recently, no polarization inversion for spin injection from Fe into GaAs(001) with an abrupt interface was observed [76], as for the sample presented here and for the FeCo contact in Ref. [12]. The authors suggest a mixed interface as an explanation for the polarization inversion observed elsewhere, that they partially found in their sample by electron microscopy. By using the experimentally determined atomic distances, their calculations show that resonance states of minority spins do not contribute to the transport for an abrupt interface. However, minority spin injection can be enhanced in the low bias regime due to intermixing at the interface [76]. The experiment and the calculations in Ref. [76] imply that the Fe sample presented here also consists of an abrupt interface, as well as the FeCo sample in Ref. [12]. Altogether, the discrepancy in current polarization as a function of bias voltage observed in the experiments mentioned above can clearly

be ascribed to the particular interface between Fe and GaAs.

4.1.4. Hanle effect measurements

We now want to estimate the spin lifetime in the n-GaAs channel via Hanle measurements. The theory of the Hanle effect for a spin injection experiment, which describes the depolarization of the injected spin accumulation in a perpendicular magnetic field, was introduced in Sec. 3.5. Fig. 4.6b shows a Hanle curve measured at a distance of 7.5 µm to the center of the (Ga,Mn)As contact. The detection position is indicated by the red dot in Fig. 4.6a.

In order to extract the spin lifetime from the Hanle measurement, all parameters responsible for the spin transport along the n-GaAs channel must be identified (see Sec. 3.5). Since the Hanle measurement shown in Fig. 4.6b was taken left to the injecting contact, within the current path, the electron drift has to be taken into account. The strength of the electron drift with respect to spin diffusion can be described by the dimensionless parameter κ [17]:

$$\kappa = \frac{L_d}{2L_s} = \frac{v_d \cdot \tau_s}{2L_s}. \tag{4.1}$$

Here, L_s is the spin diffusion length and L_d the spin drift length, defined by the drift velocity v_d and the spin lifetime τ_s. κ can be extracted from the spin density distribution shown in Fig. 4.6a via L_s and the effective decay length L_{eff} on the left hand side of the contact:

$$\kappa = \frac{L_{eff}^2 - L_s^2}{2L_s \cdot L_{eff}}. \tag{4.2}$$

The asymmetric shape of the Hanle curve stems from the fact that the remanent magnetization is not aligned along the z-axis but tilted in plane (discussed in Sec. 3.5). Thus, the angle ϕ describing the in-plane tilt of the magnetization with respect to the laser beam axis must be used as an additional fitting parameter. For $L_{eff} = 6.5$ µm and $L_s = 3.3$ µm, the fit according to Eq. (3.3) and (3.4) illustrated by the red curve in Fig. 4.6b provides a spin lifetime of 8 ns and a magnetization tilt of 23°. The magnetization tilt is also visible in the observed hysteresis loop of the injected spin polarization shown in Fig. 4.6c, where the magnetic field was swept along the z-direction. The curve reproduces the magnetization loop of the (Ga,Mn)As contact along the z-axis. Although a magnetic field of 180 Oe is not sufficient to saturate the magnetization with the external magnetic field along the z-axis, the hysteresis loop confirms the tilted magnetization: when lowering the magnetic field the curve shows a coherent rotation of the magnetization until it switches in a reversed field of about -30 Oe. A magnetization tilt of 23° would

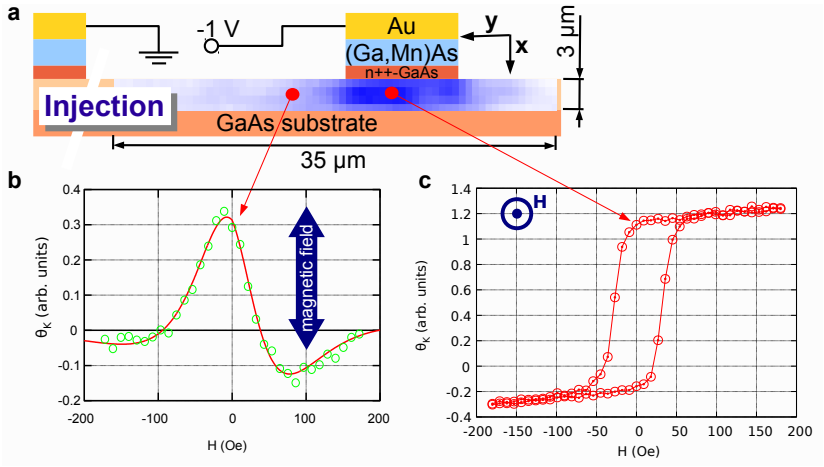

Figure 4.6.: (a) Contact geometry and spin density distribution in the n-GaAs channel for electrical spin injection. (b) Observed Hanle measurement at 7.5 µm distance to the contact center. Numerical fit based on Eq. (3.3) and (3.4) (red curve) yields a spin lifetime of about 8 ns. The asymmetric behavior stems from a tilted contact magnetization with respect to the z-direction. (c) Kerr rotation beneath the contact while sweeping the external magnetic field along the z-direction. The resulting hysteresis curve of the injected spin polarization reproduces the magnetization loop of the (Ga,Mn)As contact.

corresponds to a remanent magnetization of $\sim 87\%$ along the z-direction. This is qualitatively in good agreement with the observed hysteresis loop in Fig. 4.6c. Since the saturation of the magnetization along the z-direction ([110]) requires larger external magnetic fields an accurate value of the remanent magnetization can not be extracted from the data.

The extraction of the spin lifetime from Hanle measurements is based on a model with one-dimensional spin transport from the point of injection to the point of detection (see Sec. 3.5). Since the injected spin density distribution illustrated in Fig. 4.6a shows almost no variation in x-direction, the n-GaAs channel can be well described by a one-dimensional channel, as illustrated in Fig. 4.1. However, even more important for the legitimation of the one-dimensional model is the fact that the spin transport from all positions beneath the contact to the detection position can be described by a constant drift velocity in y-direction, which is assumed in the one-dimensional model. This is garatueed by the large interface resistance of the (Ga,Mn)As contact, causing a homogeneous electric field E_y in the n-GaAs channel (on the drift side and beneath the contact area). Therefore, the (Ga,Mn)As sample is well suited for this investigation. In contrast, when E_y is not constant for the spin transport from the point of spin injection to the point of detection, the estimation of the spin lifetime becomes more complicated. This is analyzed in detail in Sec. 4.2, where for larger bias voltages a nonuniform

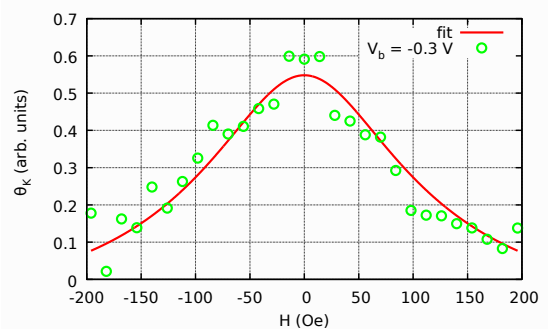

Figure 4.7.: Observed Hanle measurement in the n-GaAs channel at the left edge of the injecting Fe contact (see Fig. 4.3) for a bias voltage $V_b = -0.3\,V$. Numerical fit based on Eq. (3.3) and (3.4) (red curve) yields a spin lifetime of about 6 ns.

current around the extracting contact significantly influences the spin density distribution.

A more complicated spin density distribution in the n-GaAs channel was also observed for the Fe sample as illustrated in Fig. 4.3. Due to the lower interface resistance of the Fe contact, the current density across the Schottky barrier is not homogeneous, and hence the injection-detection distances are not well defined. In addition, E_y is not constant beneath the contact and thus, the extraction of the spin lifetime from Hanle measurements is less precise on this sample. Fig. 4.7 shows a Hanle curve for electrical spin injection with $V_b = -0.3\,V$, measured at the left edge of the Fe contact in the center of the n-GaAs channel (see Fig. 4.3). For the numerical fit (red curve) a spin diffusion length of 6 µm and a drift-diffusion ratio $\kappa = 0.5$ was used, which provides a spin lifetime of about 6 ns. Similar samples from the same Fe/GaAs wafer were analyzed later within the diploma thesis of Stefan Merz [77]. There, the temperature dependence of spin injection was investigated, demonstrating electrical spin injection up to room temperature. At 10 K, a spin diffusion length of about 6 µm and a spin lifetime of about 7 ns were found [77].

A hysteresis loop in the n-GaAs due to spin injection from the Fe contact is shown in Fig. 4.8. For thin layers of Fe on GaAs(001), the [110] direction (z-direction) is the magnetic easy axis due to a strong uniaxial in-plane anisotropy for Fe on GaAs(001) [48]. This is reflected by the rectangular switching behavior shown in Fig. 4.8. The 100% remanence of the Fe contact in z-direction is consistent with the symmetric shape of the Hanle curve shown in Fig. 4.7. Further examples of Hanle curves with asymmetric shape and a large magnetization tilt of the corresponding (Ga,Mn)As contact of almost 40° can be found in Sec. 4.3.2.

It should be noted that due to the measurement in remanence the Kerr rotation observed on the (Ga,Mn)As sample, e.g. in Fig. 4.6a, only corresponds to about 85% of the saturation Kerr rotation (see Fig. 4.6c). However, this has no influence

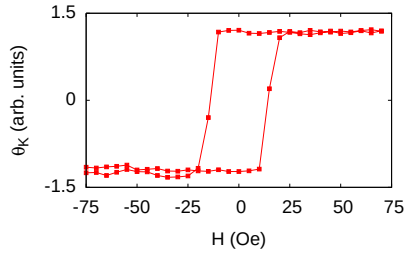

Figure 4.8: Hysteresis loop of the injected spin polarization representing the magnetization loop of the Fe contact along the [110] (z) direction.

on the observed spin density distribution since the magnetization curve of the (Ga,Mn)As contact should not change during the measurement. Consequently, the observed Kerr rotation in remanence is still proportional to the local spin accumulation as discussed in Sec. 3.2.

4.2. Nonuniform current density and spin accumulation in the n-GaAs channel

The previous section has shown how the spin density distribution in the n-GaAs changes when the current density across the interface of the injecting contact is not homogeneous anymore (compare Fig. 4.1 and 4.3). Here we show that, in addition, the electric field near the injecting contact strongly influences the spin density distribution around it. As a result a one-dimensional picture of drift and diffusion along the channel leads to incorrect spin lifetime values. This becomes obvious by comparing fitting results of Hanle data from a one- and a two-dimensional model. This topic is discussed in our publication in Applied Physics Letters 100, 092405 from March 2012 [78].

For the investigation an extended sample design was used, where the n-GaAs layer is confined into a n-GaAs channel. This also confines the current and the injected spin accumulation. A micrograph picture of the (Ga,Mn)As contact and the n-GaAs channel is shown in Fig. 4.9. The sample preparation was done by Mariusz Ciorga. The layers of the sample were grown by molecular beam epitaxy on a semi-insulating GaAs(001) substrate. The layer stack is similar as for the (Ga,Mn)As sample shown in the previous section, sketched in Fig. 4.6. The 1 µm thick n-GaAs channel for the electron transport and spin accumulation has a doping density of $2.7 \cdot 10^{16}\,\mathrm{cm}^{-3}$. Spin injecting contacts are formed by a 50 nm thick layer of $Ga_{95}Mn_5As$, a 8 nm thick layer of n^{++}-GaAs doped up to $5 \cdot 10^{18}\,\mathrm{cm}^{-3}$ and a 15 nm thick $n^{++} \rightarrow n$ transition layer. The large doping density in the n^{++}-GaAs layer and the transition layer, between the (Ga,Mn)As layer and the n-GaAs channel, is necessary for the creation of an Esaki diode (see Sec. 2.6). Details about film growth are described in Sec. 3.1.

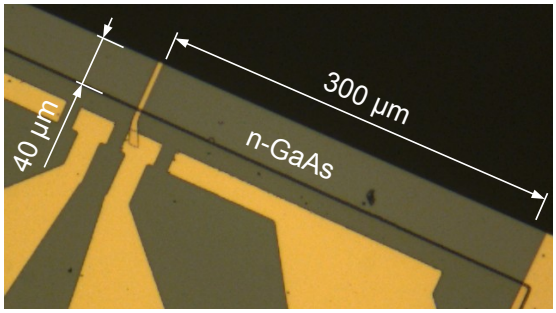

Figure 4.9.: Micrograph picture of the cleaved sample showing the 40 µm wide n-GaAs channel with the $4 \times 40\,\mu m^2$ large (Ga,Mn)As contact. Part of the reference contact on the right end of the n-GaAs channel in a distance of $\sim 300\,\mu m$ is visible as well.

The fabricated lateral device has a 50 µm wide mesa channel, one 4 µm×50 µm injecting contact and two large reference contacts located at a distance of 300 µm to the (Ga,Mn)As contact (see Fig. 4.9). By cleaving the sample along the [110] direction across the mesa channel and the ferromagnetic pad, the contact area is reduced to 4 µm×40 µm. The wavelength of the linearly polarized laser beam was chosen at 816 nm for the following measurements at 9 K. The confinement of the n-GaAs layer requires the use of this relatively small wavelength. Otherwise, for a larger wavelength with a larger penetration depth (see Sec. 3.3), back-reflections at the border of the n-GaAs channel and interference effects would occur.

4.2.1. Spin density distribution

Fig. 4.10 shows one-dimensional scans of the Kerr rotation along the n-GaAs channel for different applied positive voltages between the (Ga,Mn)As contact in the middle and the reference contact at the right hand side. As illustrated in Fig. 4.10, this denotes that unpolarized electrons in the channel are accelerated to the left and the spin accumulation is generated by an electron flow into the (Ga,Mn)As contact. Thus, spins are extracted from the n-GaAs layer. To eliminate any electro-optic background, the measurements were performed in remanence after saturation along [1-10] and [-110], respectively, and the difference between both remanent values was used as a measure of the spin polarization in the GaAs layer as described in Sec. 3.2.

The observed spin density distribution in Fig. 4.10 shows an unexpected maximum spin polarization that is located outside the contact opposite to the maximum charge current density. This peak shifts even further to the left with increasing bias voltage. On the left hand side of the contact the spin density distribution should be solely driven by diffusion. However, the measured decay

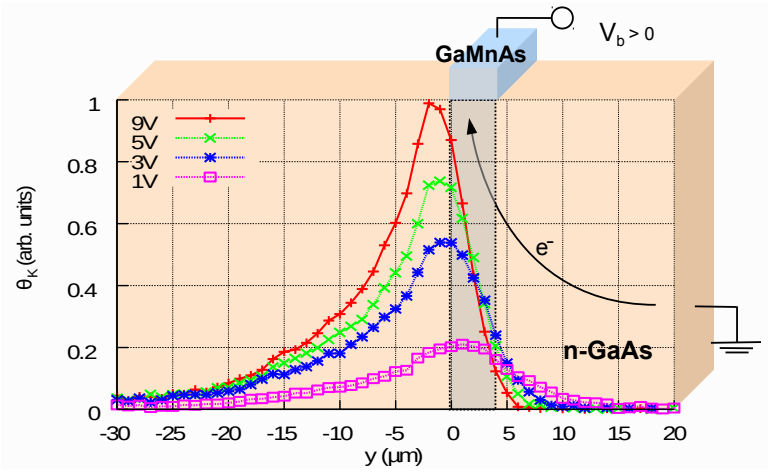

Figure 4.10.: Representation of the local spin polarization by one-dimensional linescans of the Kerr rotation along the n-GaAs channel for electrical spin extraction under various applied voltages.

of the spin polarization on the diffusion side cannot be described by a single exponential decay as expected. Depending on the bias voltage, a faster decay close to the contact edge was observed, as illustrated in Fig. 4.11. Since the decay constant defines the spin diffusion length $L_s = \sqrt{D \cdot \tau_s}$, either the spin diffusivity or the spin lifetime must be reduced in this area. A small bias dependence is still visible when fitting the curves from y-position -30 µm to -7 µm, where a spin diffusion length of 8.2 µm was extracted for the largest bias (9V / 750 µA) and 9.2 µm for the smallest bias (1V / 25 µA) (see Fig. 4.11). On the right hand side of the contact, the drift side, the spin distribution can be described by a superposition of drift and diffusion. This explains the shortened effective decay length with increasing bias voltage, but it does not explain the decay of the spin

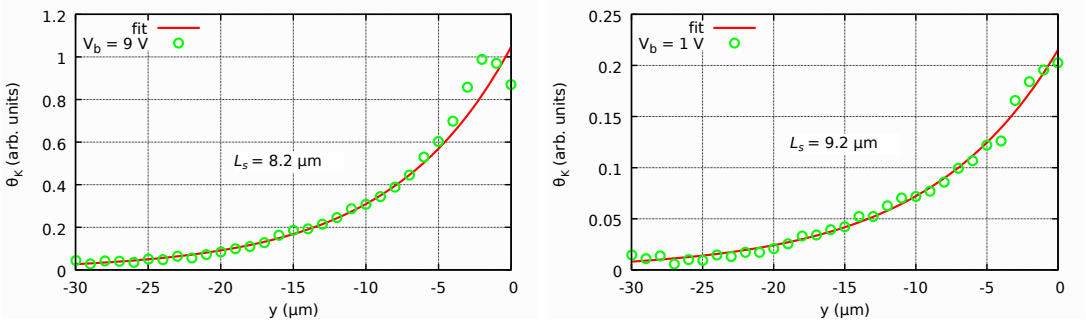

Figure 4.11.: One-dimensional linescan of the Kerr rotation on the diffusion side for electrical spin extraction using $V_b = 9\,V$ (left) and $V_b = 1\,V$ (right). Exponential fit from y-position -30 µm to -7 µm provides a different spin diffusion length L_s for both bias voltages.

polarization that already shows up beneath the contact area. The origin of this phenomenon will be discussed in the following sections.

4.2.2. Hanle measurements

For a better understanding of the observed spin density distribution and its bias dependence we also performed Hanle measurements at y-position -5 µm and -10 µm for different applied voltages, illustrated in Fig. 4.12. The curves were fitted using a one-dimensional function based on Eq. (3.3) and (3.4) (see Sec. 3.5). Assuming pure spin diffusion from the contact area to the measurement position, the only free parameter left is the spin lifetime, as the spin diffusion length is well known from the spin density distribution shown in Fig. 4.10. However, this approach leads to spin lifetimes depending significantly on the applied bias voltage and the injection-detection distance. The spin lifetime is directly connected to the width of the Hanle curves, while the height of the curves, i.e. a scaling factor, has no influence on the spin lifetime. The values are changing from 14 ns for a large voltage and small distance ($y = -5\,\mu m$ and $V_b = 9\,V$) to 46 ns for a small voltage and large distance ($y = -10\,\mu m$ and $V_b = 1\,V$). The bias dependence is less pronounced when measuring further away from the contact, but still a factor of two difference in the resulting spin lifetime is observed. However, even the 1V-data with a current of 25 µA yield different values at both positions (42 and 46 ns).

Since the spin lifetime should not depend on the applied bias voltage for spin extraction, the result indicates that the one-dimensional model is insufficient to correctly describe the spin transport in the n-GaAs channel. This is also reflected by the observed spin density distribution shown in Fig. 4.10 which can not be fully described by the one-dimensional model as well. To shed light on this behavior we performed numerical simulations using a two-dimensional model for electron drift and spin diffusion as shown in the following.

4.2.3. Two-dimensional simulation

The two-dimensional simulations of the spin density distribution in the n-GaAs channel were done in collaboration with Robert Wagner using COMSOL Multiphysics. A detailed description of the simulation and a step-by-step instruction are given in his thesis [79]. The simulation was done in two steps: first the current density distribution was simulated in the n-GaAs channel that in principle depends on the interface resistance of the Esaki diode and the channel resistance. Both values could be determined experimentally, e.g. the voltage drop across the interface was detected via the second reference contact. At 9 K, the channel's

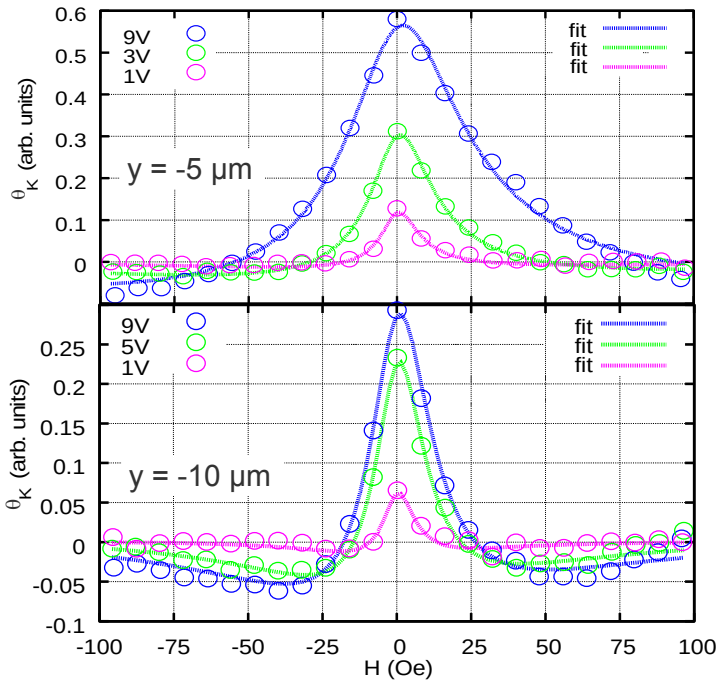

Figure 4.12.: Hanle-curves for different applied bias voltages, measured at y-position -5 µm (top) and -10 µm (bottom) (see Fig. 4.10). Fits using a one-dimensional (1D) model yield different values of the spin lifetime which are shown in Table 4.1.

conductivity is 1500 S/m, resulting in an electron mobility μ of 0.35 $m^2/(s \cdot V)$ in the n-GaAs channel. In the simulation, the Esaki diode was represented by a 10 nm thick layer with a conductivity of 0.025 S/m, matching with the experimentally determined resistance. Based on the result for the current density distribution, the spin density distribution was then calculated in a second step. There, a spin current across the interface was assumed that is proportional to the local charge current density. The generated spin accumulation in the simulation then spreads due to diffusion and the electron drift previously calculated for this sample geometry until a steady state was found. A derivation of the used differential equations and boundary conditions can be found in Ref. [17]. The spin diffusivity in the simulation is defined by the spin diffusion length, extracted from the measurements shown in Fig. 4.10, and the spin lifetime (42 ns), estimated by Hanle measurements.

Fig. 4.13 illustrates the simulated spin density distribution for a large positive applied bias voltage at the (Ga,Mn)As contact. The color-coded spin polarization reproduces the observed spin density distribution shown in Fig. 4.10 quite well: the pronounced nonuniform current density beneath the contact area shifts the spin accumulation towards the diffusion side. Thus, depending on the applied bias voltage, the polarization peak shifts towards the left as observed in the experimental results shown in Fig. 4.10. The simulation also directly explains

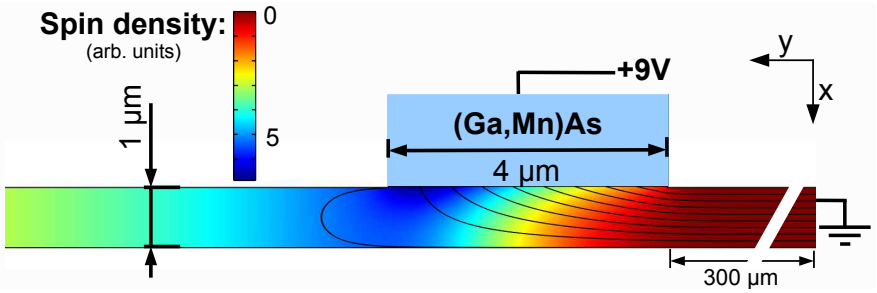

Figure 4.13.: Two-dimensional drift-diffusion simulation of the spin accumulation in a 1 µm thick n-GaAs channel. Black lines represent the local current direction with an electron flow from right to left except for the leftmost trajectory.

the extremely fast decay of the spin polarization on the right hand side of the contact, where the decay already begins beneath the contact area.

A direct comparison of the simulated spin density distribution and the experimental data is shown in Fig. 4.14. There, a one-dimensional linescan was extracted from the simulated distribution using the spin density values in the center of the n-GaAs channel (red squares) in order to fit the data to the Kerr rotation along the n-GaAs channel (blue circles) via the spin diffusion length and a scaling factor. Fig. 4.14 shows that the experimental data can be nicely reproduced by our two-dimensional model. Small deviations only occur beneath the contact area for larger bias voltages, e.g. the simulation provides a polarization peak which is closer to the contact edge than experimentally observed. The fitted spin diffusion length L_s is mainly determined by the exponential decay on the diffusion side. Due to the deviations close to the contact, the values slightly differ from the spin diffusion length extracted above (see Fig. 4.11) where only the experimental data from $y = -30\,\mu m$ to $y = -7\,\mu m$ was used to extract L_s. A fixed spin lifetime was used for each simulation as denoted in Fig. 4.14. Since the influence of the spin lifetime on the spin density distribution is rather weak, the integration of the spin lifetime as an additional fitting parameter is not useful [79]. A variation of the spin lifetime could not resolve the small deviations of the two-dimensional model and the experimental data. Also a convolution of the simulated spin density distribution in order to take into account the averaging of the Gaussian laser beam does not reduce the small deviations close to the contact area [79]. Possible reasons are shown below. Nevertheless, the two-dimensional model nicely explains the main features of the one-dimensional linescans of θ_K.

An important point to note is the nonuniform current density on the diffusion side and underneath the contact area. As illustrated in Fig. 4.13 by the black lines representing the local current direction, the n-GaAs channel on the diffusion side, i.e. left to the (Ga,Mn)As contact, can be divided into a bottom channel where electrons are flowing to the left away from the contact and a top channel

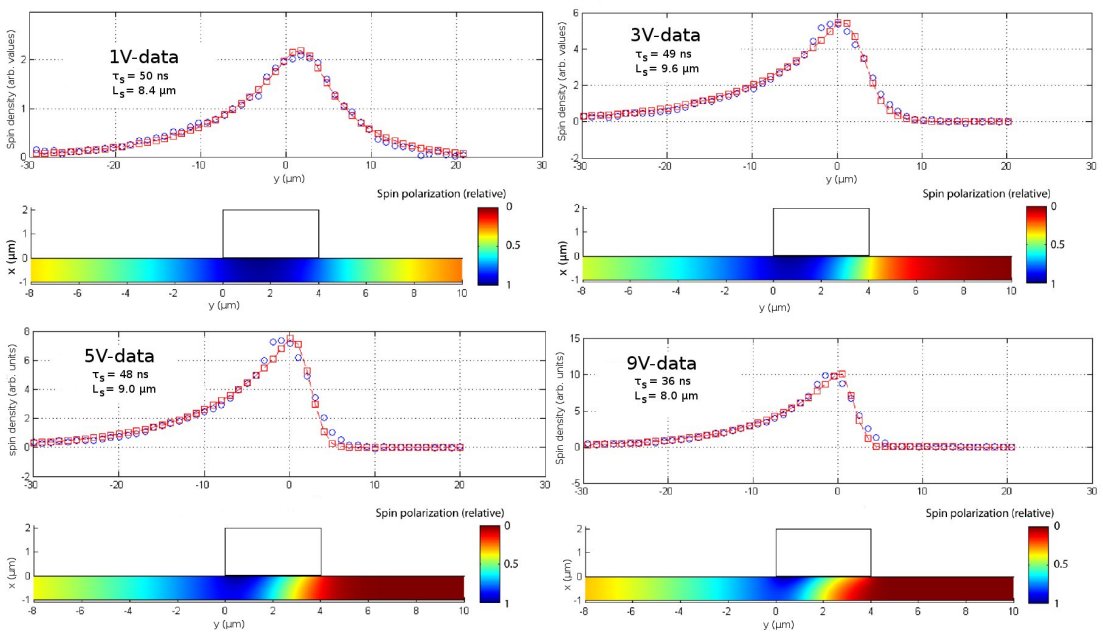

Figure 4.14.: Fit of the observed spin density distribution (blue circles) with the two-dimensional model (red squares) via the spin diffusion length L_s (from [79]). The corresponding two-dimensional spin density distribution for each bias voltage is shown beneath the graphs.

with a back-flow towards the contact. This nonuniform current density decays rapidly with increasing distance to the contact but cannot be neglected within the first micrometer on the diffusion side. Due to this inhomogeneous current density it is not sufficient to describe the electron spins solely by diffusion on this side of the channel, which was done before when fitting the Hanle curves with the one-dimensional model. In particular, the electric field beneath the contact area generates a positive drift velocity towards the Hanle measurement positions left to the contact at $y = -10\,\mu m$ and $y = -5\,\mu m$ (see Fig 4.10). This additional drift widens the Hanle curves and therefore the fit provides lower spin lifetimes. This effect becomes apparent when the Hanle data shown in Fig 4.12 is fitted with the two-dimensional model where the bias dependent spin density distribution and the nonuniform drift is taken into account, as described in the following.

In order to fit the Hanle data using the two-dimensional simulation, spin precession about an external magnetic field was included in the second simulation step [79]. For each out-of-plane magnetic field value that was used in the Hanle measurement a simulation of the spin density distribution was carried out and compared with the experimental data at positions $y = -10\,\mu m$ and $y = -5\,\mu m$. Then a variation of the fitting parameters including the spin lifetime was performed until a least square fit to the experimental data was found. As in the one-dimensional case a spin diffusion length L_s of $9\,\mu m$ was used for all curves.

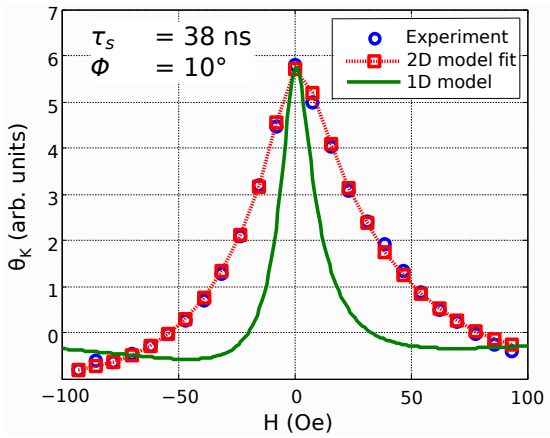

Figure 4.15.: Fit of the experimental Hanle data at position $y = -5\,\mu m$ with an applied bias voltage of 9 V. The red curve represents the fit with the two-dimensional model which yields a spin lifetime of 38 ns and a magnetization tilt of 10°. The green curve illustrates the lineshape of the one-dimensional model for the same spin lifetime.

A slight asymmetry arising from the magnetization tilt was also found in all Hanle measurements and had to be taken into account in the fitting procedure. A magnetization tilt ϕ of about 10° could be extracted from the curves (for details see Sec. 3.5.1). Fig. 4.15 shows an example of the two-dimensional model fit for the 9V-data. It also shows the discrepancy when using the 1D-model with the parameters extracted from the 2D-model fit. Table 4.1 shows a direct comparison of the spin lifetimes obtained from the two-dimensional model (2D) and the frequently used one-dimensional model (1D) introduced in Sec. 3.5.

A spin lifetime of 38 ns was extracted from the 9V-data using the 2D-model, in contrast to 14 ns for the 1D-model. Thus, the strong bias dependence of the spin lifetime from the one-dimensional model (from 14 ns for 9 V to 42 ns for 1 V) can be primarily attributed to the neglect of the nonuniform current. However, a variation of the spin lifetime with bias voltage and contact distance of about 20% remains (see Table 4.1), which needs an explanation.

The dominant spin relaxation mechanism for n-doped GaAs above the metal-insulator transition is the D'yakonov-Perel' mechanism [18]. This mechanism strongly depends on the electron energy in the conduction band, for instance on the doping density or the temperature (see Sec. 2.2.1). Thus, a small temperature increase due to Joule heating might be responsible for the observed decrease of the spin lifetime with increasing bias voltage. However, only a weak temperature dependence of the spin lifetime was found below 50 K for metallic n-GaAs [7, 20], where the thermal energy is small compared to the electron energy in the conduction band (see Sec. 2.3).

Besides the temperature, also the electric field has an influence on the spin life-

		1 V	3 V	5 V	7 V	9 V
y = −5 µm	1D	42 ns	25 ns	20 ns	16 ns	14 ns
y = −5 µm	2D	46 ns	47 ns	46 ns	41 ns	38 ns
y = −10 µm	1D	46 ns		29 ns		23 ns
y = −10 µm	2D	53 ns		53 ns		47 ns

Table 4.1.: Spin lifetimes from numerical simulations based on 1D and 2D drift-diffusion models at two different distances, y, from the contact edge and different bias voltages.

time, as has already been shown for optically pumped spins in 2006 [80, 81]. The reason is the increased energy of the electrons when accelerated in electric fields leading to a more efficient spin relaxation due to the D'yakonov-Perel' mechanism (see Sec. 2.2.1). In addition the momentum relaxation time τ increases with electron velocity (see Sec. 2.3), which also enhances the D'yakonov-Perel' mechanism. A detailed calculation of this effect was reported by Beck et al. [80].

From the one-dimensional scans and the simulation it is evident that electric fields are present around the contact area. Even for the 1V-data, the electric field in the n-GaAs channel is in the order of 10 V/cm, that, according to Refs. [80] and [81] should already reduce the spin lifetime. Since strong electric fields are only located beneath the contact area and the electric field intensity decreases rapidly on the diffusion side, larger spin lifetimes and a less pronounced bias dependence can be expected when measuring further away from the contact, as observed in the experiment.

In summary, it is shown that a nonuniform current density in the n-GaAs channel affects the spin density distribution. The pronounced electric field beneath the contact area generates a drift towards the diffusion side and therefore widens Hanle curves when measured on this side of the contact. As a consequence, extracting the spin lifetime with the frequently used one-dimensional model assuming pure spin diffusion leads to a strong bias and contact distance dependence. Hence a two-dimensional model has to be used to yield correct spin lifetimes. The remaining variations with distance and bias can be attributed to Joule heating or the presence of electric fields around the contact area.

As a final note, the discrepancy between the diffusion of spins and electrons observed earlier will be addressed. It was reported in 1999 that the spin diffusivity resulting from the spin diffusion length and the spin lifetime ($D_s = L_s^2/\tau_s$) exceeds the electron diffusivity D_e extracted via the mobility (see Sec. 2.3) by more than one order of magnitude [9]. Since n-GaAs with a doping density below the metal-insulator transition was used in this experiment ($n = 1 \cdot 10^{16}\,\mathrm{cm}^{-3}$), the

thermal energy at 1.6 K was used to obtain D_e via the mobility (see Eq. (2.7)). The sample investigated here has a carrier concentration of $2.7 \cdot 10^{16}\,\mathrm{cm}^{-3}$ and a mobility of $3.5 \cdot 10^3\,\mathrm{cm}^2/\mathrm{Vs}$. Using Eq. (2.9) to estimate the density of states at the Fermi energy gives an electron diffusivity of $D_e \approx 5\,\mathrm{cm}^2/\mathrm{s}$. Using Eq. (2.10) to estimated the density of states at the Fermi energy gives an electron diffusivity of $D_e \approx 11\,\mathrm{cm}^2/\mathrm{s}$. Extracting the diffusivity from the spin diffusion length and the spin lifetime ($D_s = L_s^2/\tau_s$) gives $D_s \approx 16\,\mathrm{cm}^2/\mathrm{s}$ for $L_s = 9\,\mu\mathrm{m}$ and $\tau_s = 50\,\mathrm{ns}$, which is approximately a factor of two larger. However, taking into account the amount of parameters for the calculation of D_e and D_s and the approximations used for the density of states, both values are in fair agreement. No difference between electron and spin diffusion was found recently in n-GaAs at room temperature [82]. A possible explanation for the larger D_s with respect to D_e found in Ref. [9] at 1.6 K is given in Ref. [83], where the authors predict that due to the charge-neutrality of a spin packet, the diffusion of it in the conduction band is not inhibited by holes and thus has a larger diffusivity than a charge packet [83]. A further theoretical discussion is including the influence of Coulomb interactions on spin diffusion [84], e.g. the spin Coulomb drag effect which reduces the spin diffusion coefficient. The authors also predict that D_s is larger then D_e at 1.6 K for the doping densities used here. However, at 20 K their calculations show almost no deviation between D_s and D_e.

4.3. Spin solar cell and spin photodiode effect

The last section has shown the influence of electric fields on the spin density distribution in the n-GaAs channel. The ability to displace the spin accumulation by an electric field opens new possibilities for modulation, which will be used in the following to demonstrate the spin solar cell and spin photodiode effect.

One of the main quests in spintronics research today is the efficient and energy conserving generation of pure spin currents. Ideally, and mainly in order to reduce energy consumption, pure spin currents should be generated without the use of charge currents which cause Joule heating. Modern concepts avoiding charge currents in the conventional sense range from spin pumping (generated by microwaves into Pt [85] or GaAs [86], or by temperature gradients or phonons [87]) to thermal injection [88], which will be both discussed in Sec. 4.4. In contrast, electrical spin injection requires the use of charge currents, as shown before. In direct bandgap semiconductors, optical spin pumping is also a convenient way to generate spins without the need of charge currents (see Sec. 2.1). Due to the optical selection rules this method usually calls for circularly polarized light at a well defined wavelength.

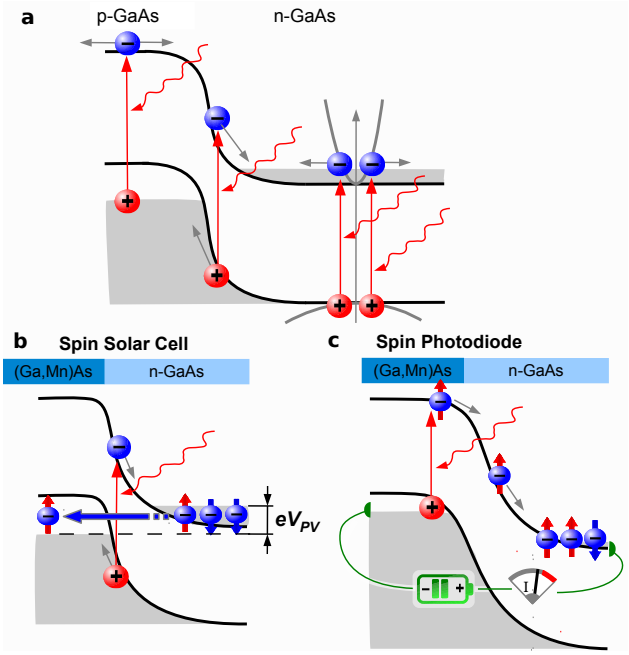

Figure 4.16: (a) Influence of illumination on a GaAs p-n-junction illustrated via the energy diagram. (b) Working principle of the spin solar cell: The light induced photovoltage V_{PV} drives an electron tunneling current (blue arrow) across the gap resulting in a spin accumulation on the n-GaAs side. (c) Working principle of the spin photodiode: At reverse bias the width of the tunnel barrier increases and tunneling is suppressed. Photoexcited spin-up electrons from the (Ga,Mn)As are drifting to the n-GaAs and generate an oppositely oriented spin accumulation. Only the electron-hole pairs which are responsible for the corresponding effect are illustrated in (b) and (c).

New effects can be expected when instead of a homogeneous semiconductor a p-n-junction is illuminated. A spin-voltaic effect has been predicted for a magnetic/nonmagnetic p-n-junction where either the p-type or the n-type semiconductor is magnetic, i.e., has a spin-split band [89, 90]. This effect has recently been experimentally demonstrated in a non-magnetic n-GaAlAs/p-GaInAs/p-GaAs junction in the presence of a magnetic field allowing to convert circularly polarized light into an electric signal [91]. Additional functionalities (e.g. magneto-amplification) have also been proposed [92, 93] and observed [94] for magnetic transistors.

Here, the spin solar cell is introduced as a novel spintronic device which combines the principle of a solar cell with the creation of spin accumulation. It will be demonstrated that efficient optical spin injection can be achieved with **unpolarized** light by using a p-n-junction where the p-type region consists of a **ferromagnetic semiconductor**. The discovered novel mechanism opens the window for the optical generation of a sizeable spin accumulation also in semiconductors without direct band gap such as Si or Ge. Moreover, it will be shown that the device can be used as a photo-sensor presenting an additional degree of freedom, namely the generated spin polarization, which can be set by the magnetization direction and, for instance, read out by the inverse spin Hall effect [95, 96].

Fig. 4.16a shows the energy diagram of a p-n-junction based on GaAs. When illuminated by photons with an energy larger than the band gap, electron-hole

pairs in all three regions - p-type semiconductor, p-n transition region and n-type semiconductor - are generated. While the optically excited electrons within the p- and n-side of the junction diffuse in all directions and mostly recombine, the electron-hole pairs created at the interface in the band-bending region are separated by the built-in electric field. This effect is used in a conventional solar cell for the generation of a photo-voltage or photo-current. The same working principle holds for the device demonstrated here, except that the p-side of the junction is replaced by the dilute magnetic semiconductor (DMS) (Ga,Mn)As in the ferromagnetic state (see Sec. 2.6). In addition a large doping density at the interface of the n-GaAs is used in order to create a tunnel diode or Esaki diode (see Sec. 2.5). Due to the heavily p-doped (Ga,Mn)As, the band bending region is mostly confined to the n-GaAs. If such a p-n-junction is illuminated the resulting photo-current will mostly consist of photo-excited electrons from the n-GaAs side and only a small fraction of spin-polarized electrons created in the (Ga,Mn)As. Thus, the spin polarization of the photo-current is small. The charge accumulation in the n-GaAs leads to a photo-voltage V_{PV} which in turn causes electrons to tunnel across the narrow barrier into the (Ga,Mn)As, as illustrated in Fig. 4.16b. Due to the different tunneling currents for spin up and spin down electrons, the generation of a spin accumulation can be expected in the n-GaAs. This means, the incident light not only creates a voltage due to the photo-voltaic effect, but also a spin current across the interface and hence spin accumulation in the GaAs, i.e. light-induced spin extraction should occur (see Fig. 4.16b).

Moreover, a second working mode can be expected by applying a negative voltage to the p-side of the junction (reverse bias). In a common p-n-junction, the current is suppressed in reverse direction unless the junction is illuminated. Thus a common p-n-junction can be used as a photo-sensor converting light into current. In our device, light creates electron-hole pairs in the (Ga,Mn)As layer as well, which are spin polarized due to the spin-dependent density of states [40]. The electric field at the p-n-junction drives the optically generated spins from the (Ga,Mn)As conduction band into the n-GaAs layer. At the same time the negative bias suppresses the spin-polarized current tunneling from the n-GaAs into the (Ga,Mn)As as sketched in Fig. 4.16b, thus the sign of the spin accumulation is expected to be reversed (Fig. 4.16c compared to Fig. 4.16b).

The experimental realization of a spin solar cell and a spin photodiode will be presented in the following on two samples from two different wafers. Both samples were prepared by Mariusz Ciorga using optical and e-beam lithography and a wet etching technique. An overview of the performed measurements is sketched in Fig. 4.17. The p-n-hetero-junction is designed as a tunnel diode consisting of a (Ga,Mn)As p-layer and a 1 µm thick n-GaAs channel. The spin solar cell effect will be first demonstrated in Sample A by using the laser-beam simultaneously for the generation of electron-hole pairs and as a detector for the generated spin accumulation via pMOKE (Fig. 4.17b). Furthermore the spin solar cell effect will

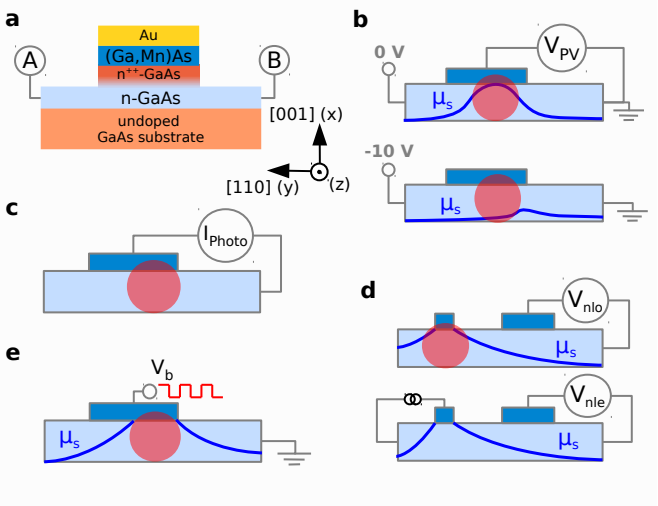

Figure 4.17.: Layer stack and contact geometry of Sample A (a) and measurement principles of the spin solar cell and the spin photodiode effect. The red circle illustrates the position of the laser spot with 1 µm diameter. (b) Optical detection of the spin solar cell effect by pMOKE. The two modulated states of the spin accumulation are illustrated by the blue curves. (c) Determination of the photo-current in closed circuit. (d) Electrical detection of the spin accumulation in a non-local voltage geometry for the spin solar cell effect and electrical spin injection on Sample B, having the same layer stack as Sample A (a). (e) Optical observation of the spin photodiode effect by applying a negative voltage to the (Ga,Mn)As contact, modulated by a square wave bias voltage.

be analyzed electrically in Sample B in a non-local voltage geometry illustrated in Fig. 4.17d. There, the photo-current is used (Fig. 4.17c) in order to compare the spin solar cell effect with electrical spin injection. The layer stack of Sample A and B is similar, only the doping density at the interface is slightly increased in Sample B. Therefore, the spin photodiode effect will be demonstrated on Sample A where the tunneling current is suppressed in reverse direction. This means, electrical spin injection is suppressed in Sample A and the spin photodiode effect can be directly observed as illustrated in Fig. 4.17e.

4.3.1. Spin solar cell

The effect of spin extraction due to laser illumination is demonstrated in the following by measuring the local Kerr rotation underneath the ferromagnetic contacts at 15 K. The layer stack and contact geometry of Sample A are sketched in Fig. 4.17a. The spin accumulation is observed in a 1 µm thick n-GaAs channel with a doping density of $2.5 \cdot 10^{16}\,\mathrm{cm}^{-3}$. This layer is followed by a 15 nm thick transition layer where the doping density is gradually increased and a 8 nm

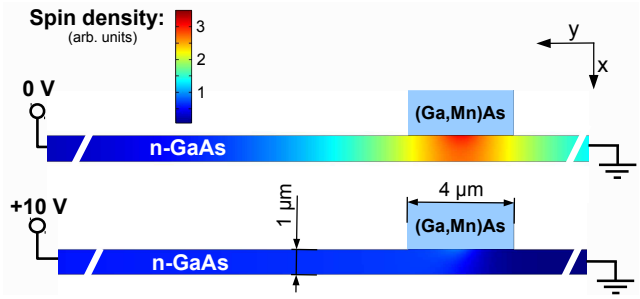

Figure 4.18.: Two-dimensional simulation of the spin density distribution due to the spin solar cell effect with (bottom) and without (top) applied electric field along the n-GaAs channel (600 µm length, conductivity of 1500 S/m). Details about the simulation procedure can be found in Sec. 4.2.3. The constant spin current density across the (Ga,Mn)As/n-GaAs interface generated by the laser light is described by using a Gaussian function around the contact center with a FWHM of 1 µm. In addition, a spin diffusion length of 6 µm and a spin lifetime of 10 ns are assumed in the n-GaAs.

thick layer of n^{++}-GaAs with a nominal doping density of $5 \cdot 10^{18}\,\mathrm{cm}^{-3}$. This creates a tunnel diode between the 50 nm thick $Ga_{95}Mn_5As$ layer and the n-GaAs layer as described in Sec. 2.5. In addition a 2 nm thick (Al,Ga)As layer was inserted between the GaAs and the (Ga,Mn)As (see Sec. 3.1). The electron transport in the lateral device is confined to a 50 µm wide mesa channel with a 4 µm×50 µm (Ga,Mn)As contact on top and two reference contacts at both ends of the channel with a distance of 300 µm to the injecting contact. By cleaving the sample along the [110] direction across the mesa channel the contact area is reduced to 4 µm×40 µm. In addition the cleaving process exposes the GaAs(1-10) surface and enables direct optical access to the n-GaAs channel (see Sec. 3.1.3).

In order to observe the spin solar cell effect in Sample A, the modulation technique used for electrical spin injection (see Sec. 3.2) must be adapted. Since the spin solar cell effect works without any electrical connection to the (Ga,Mn)As contact, the spin accumulation in the n-GaAs was modulated by applying a square-wave bias voltage V_{AB}, alternating between zero and ±10 V, between the two reference contacts A and B on the left and the right end of the GaAs channel (see Fig. 4.17a). The situation for zero voltage is shown in Fig. 4.17b in the upper panel where the generated spin accumulation is located at the laser spot. In contrast, when ±10 V are applied, the large electric field that builds up along the channel shifts the laser-induced spin accumulation $\mu_s = \mu_\uparrow - \mu_\downarrow$ away from the spot position as sketched in Fig. 4.17b in the lower panel. Thus, for large enough electric fields, the spin accumulation is almost zero at the laser spot position since the spins are subsequently drifting away. The principle of this modulation technique can also be shown by two-dimensional simulations of the electron drift and spin diffusion in the n-GaAs channel, as introduced in Sec. 4.2.3. Fig. 4.18 shows the simulated spin density distribution due to the spin solar cell effect,

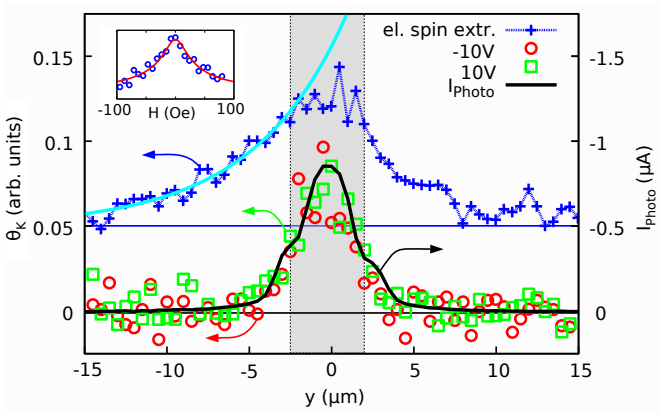

Figure 4.19.: Kerr rotation along the n-GaAs channel showing a comparison between the spin solar cell effect (green, red) and electrical spin extraction (blue, 0.7 V / 12 µA, spin diffusion length of 6 µm, offset added for clarity) using the same absorbed laser power (816 nm - 35 µW/µm^2 - 15 K). Positive and negative applied voltages (-10 V, 10 V) along the channel are only used for modulation. The shaded area indicates the contact position. The position-dependent photo-current along the channel was measured separately in closed circuit (black). The inset shows Hanle depolarization of the spin solar cell effect in an out-of-plane magnetic field. The fit yields a spin lifetime of about 13 ns.

with and without an electric field along the n-GaAs channel. The spin solar cell effect was simulated by assuming a constant spin current density across the (Ga,Mn)As/n-GaAs interface, described by a Gaussian function around the center of the (Ga,Mn)As contact in order to represent the laser spot at this position. The upper panel of Fig. 4.18 shows the generated spin accumulation without electric field, i.e. pure spin diffusion with a spin diffusion length of 6 µm. The lower panel illustrates the situation when 10 V are applied between the reference contacts at both ends of the 600 µm long n-GaAs channel, which significantly reduces the spin accumulation beneath the (Ga,Mn)As contact by about a factor of 10. The Kerr rotation in this state therefore can be used as a reference signal for the case when almost no spin accumulation is present at the laser spot. Beside the adapted electrical modulation, the measurement principle is the same as for electrical spin injection (see Sec. 3.2) using only the difference in Kerr rotation of both remanent magnetization values along the z-axis. This results in a signal θ_K which is strictly proportional to the spin accumulation in the n-GaAs channel at the laser spot position.

Fig. 4.19 shows linescans of the Kerr rotation along the n-GaAs channel obtained by the technique described above (red and green symbols: $V_{AB} = 10\,\mathrm{V}$ (□) and $-10\,\mathrm{V}$ (O)). The position of the (Ga,Mn)As contact is indicated by the shaded area. Due to the absence of spin accumulation at the laser spot for ±10 V (see Fig. 4.18), the traces of θ_K for +10 V and -10 V are equivalent. Both curves clearly

show that a spin accumulation can only be observed when the laser spot is placed at the contact. The signal immediately vanishes when the laser spot is moved away from the contact area, indicating that the spin accumulation is induced by laser illumination. Due to the large interface resistance of the (Ga,Mn)As contact and a relatively large capacitance a modulation frequency of only 187 Hz was chosen for the measurements of the spin solar cell effect. For larger frequencies, due to the floating potential of the (Ga,Mn)As contact, charging and decharging effects of the (Ga,Mn)As contact can be observed which correspond to electrical spin injection and extraction. However, the signal from this effect changes sign when the modulation voltage is reversed and therefore cannot be responsible for the observed Kerr rotation. The Hanle depolarization of the spin solar cell effect is shown in the inset of Fig. 4.19 where the fit yields a spin lifetime of 13 ns in the n-GaAs channel. This additionally confirms the presence of spin accumulation in the n-GaAs. The fitting procedure is described in Sec. 3.5.

When the laser spot is located at the contact region ($y = 0\,\mu m$ in Fig. 4.19) the photo-voltaic effect can be observed, resulting in a positive voltage V_{PV} of 130 mV between the (Ga,Mn)As contact and the n-GaAs channel for the used laser power (absorbed power density of $35\,\mu W/\mu m^2$, see Sec. 3.4). The corresponding photo-current flows when short-circuiting the (Ga,Mn)As contact and the n-GaAs channel (see Fig. 4.17c). It is plotted as the black curve in Fig. 4.19. The good agreement of this trace with the Kerr rotation signal is further evidence of the spin solar cell effect, since the photo-current in closed circuit directly reflects the laser-induced tunneling current in open circuit. The direct connection between the photo-current and the spin extracting tunneling current is shown experimentally later. It can also be understood in a simple picture: when illuminating the contact region, part of the laser-light ($\sim 1\,\mu m$ spot size) is absorbed in the band-bending regime where electrons and holes are separated in the built-in electric field (see Fig. 4.16). This gives rise to a negative current in closed circuit, the so-called photo-current, signifying an electron flow into the n-GaAs and a hole flow into the (Ga,Mn)As. In a stationary state, the generation rate of electron-hole pairs within the band-bending region should be equal to this photo-current. Since the resistance of the tunnel barrier is more than a factor of 10 larger than the channel resistance ($\sim 15\,k\Omega$), the tunneling current is suppressed in closed circuit (see Fig. 4.17c). In open circuit, a photo-voltage builds up until in equilibrium the tunneling current should also match the generation rate of electron-hole pairs in the band-bending region. Consequently, photo-current in closed circuit and tunneling current in open circuit should be similar.

The dependence of the photo-current and the photo-voltage on the absorbed laser power is shown in Fig. 4.20. As expected, the photo-current shows an almost linear dependence contrary to the photo-voltage which already starts with a value of about 100 mV for the lowest laser power and saturates with increasing power density at about 200 mV. This shows that the interface resistance decreases

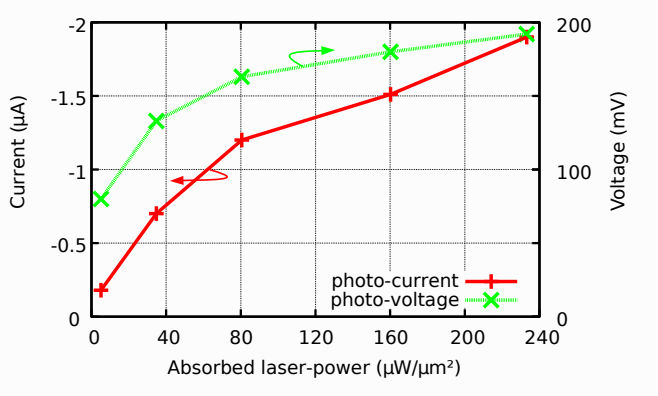

Figure 4.20: Influence of the absorbed laser power density on photo-current and photo-voltage for 816 nm wavelength and at 15 K (Sample A).

when illuminated, which is reasonable since both the photo-excited electrons in the n-GaAs and the photo-generated holes in the (Ga,Mn)As effectively reduce the tunnel barrier thickness. Due to the reduction of the tunnel barrier with increasing laser power the photo-voltage can be balanced more easily by the tunneling electrons. This is important for the analysis of the spin solar cell effect since it ensures that the laser-induced spin extraction process mostly takes place at the laser spot position.

Fig. 4.19 also illustrates the spin density distribution for electrical spin extraction (blue), where a bias voltage of 0.7 V was applied between the (Ga,Mn)As contact and the reference contact B on the right end of the GaAs channel. The forward bias voltage causes an extraction of spin up electrons at the interface from the n-GaAs into the (Ga,Mn)As contact, leaving behind a spin down accumulation diffusing in both directions along the n-GaAs channel. On the right hand side of the (Ga,Mn)As contact, due to the application of the bias voltage, the spin density distribution is determined by the superposition of electron drift and spin diffusion opposing each other. On the left hand side of the contact the spin transport is purely diffusive and a spin diffusion length of 6 µm can be extracted from the exponential decay of θ_K. Interestingly, the maximum Kerr rotation angle for the solar cell effect in Fig. 4.19 for a laser intensity producing a photo-current of 0.9 µA in short-circuit is essentially the same as for electrical spin extraction with a current of 12 µA. This somehow unexpected observation can be understood by taking into account that the photo-current and the equivalent tunneling current are confined to a cross section defined by the laser spot diameter of 1 µm and the penetration depth of the laser beam of a few µm. In the case of electrical spin extraction the cross section of the current is given by the dimension of the (Ga,Mn)As contact of 4 µm × 40 µm. Apparently, the accumulated spin density due to the effective current densities and spin diffusion in both cases is nearly the same.

Fig. 4.21 shows the influence of laser power on the n-GaAs via the Kerr spectrum. With increasing laser power the Kerr spectrum is altered by the additional

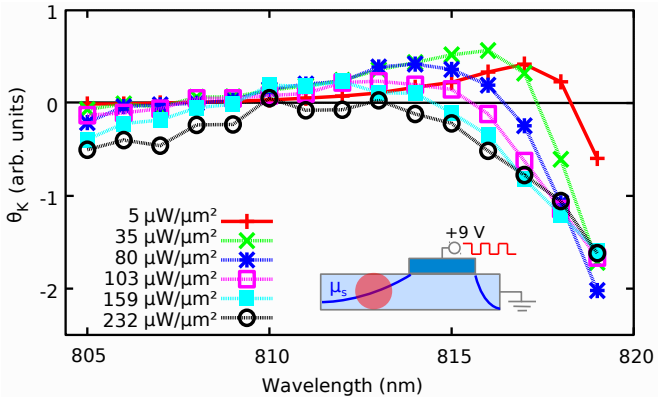

Figure 4.21.: Kerr-spectra for various laser intensities (absorbed power density) taken at the diffusion side next to the contact (see inset) while directly extracting spins electrically.

optically generated electrons that increase the electron density in the GaAs conduction band (see Sec. 3.4). Therefore, a quantitative dependence of the spin solar cell effect on laser power via the Kerr rotation is not trivial. The Kerr spectra were determined in a reference experiment on the same sample where the spin accumulation was created by direct electrical spin extraction ($V_b = 9\,V$). The spectra were observed on the diffusion side a few µm away from the (Ga,Mn)As contact in order to rule out any influence of the laser light on the contact resistance. The data clearly shows a shift to shorter wavelengths with increasing laser intensity. A shift of 1 nm corresponds to about 2 meV shift of the absorption edge or a 1 meV shift of the Fermi energy in the conduction band. Compared to the generated photo-voltage, the increase of the Fermi energy in the n-GaAs conduction band by the optically generated electrons of a few meV is negligible. In fact, the Fermi energy increase is balanced across the whole p-n-junction in equilibrium. The additionally generated electrons and holes therefore act as an increased doping density in the p-n-junction and hence illumination will solely result in a narrower tunnel barrier as shown before. For the lowest laser power of $5\,\mu W/\mu m^2$ no spin solar cell effect could be observed. However, a well defined Kerr spectrum is visible as shown in Fig. 4.21 by the red curve so that this laser intensity can be used as a probe for spin accumulation where any other effects due to laser illumination can be ruled out.

Finally - due to the electrical modulation - other effects like thermal spin injection may appear. However, it is easy to prove that no spin accumulation is generated by the relatively large voltage applied along the n-GaAs channel for the modulation of the spin solar cell effect (e.g. thermal spin injection due to Joule heating), since the Kerr rotation signal disappears when the laser power is reduced to a probe beam intensity (corresponding to an absorbed laser power of $5\,\mu W/\mu m^2$). Furthermore a spin density distribution with a spin diffusion length

of 6 µm would be observed and the drift effects from the electric field would be visible. Since the observed Kerr rotation is only visible when the laser spot is at the contact region (see Fig. 4.19), the spin accumulation must be created by the laser light itself. A temperature gradient due to the incident laser light is also not expected since the n-GaAs and (Ga,Mn)As layer are equally illuminated in the experiment. Furthermore, the large photo-voltage in the order of 100 mV which occurs also for low laser intensities can not be explained by a temperature gradient. Assuming that this voltage is mainly of thermo-electric origin, then using a Seebeck coefficient of 0.5 µV/K for GaAs/(Ga,Mn)As given by Naydenova et al. [97] a temperature difference across the junction of nearly $2 \cdot 10^5$ K would be required to generate the observed voltage. Thus, a thermo-electric origin of (photo)voltage and (photo)current can be ruled out, and this should also be true for a conceivable spin accumulation related to the spin Seebeck effect [88]. Altogether, this clearly shows that the observed signal in Fig. 4.19 corresponds to laser-induced spin extraction - the spin solar cell effect. In addition, the signal fits the observed photo-current distribution quite well which is measured when short-circuiting the junction. The electrical detection of the effect in the next section will directly prove the equivalence of the measured photo-current and an electrically applied current.

4.3.2. Electrical detection

To further substantiate the presented spin solar cell mechanism, the effect was measured in electrical detection in a non-local voltage geometry, which allows to separate illumination and detection. This is shown in Sample B, which consists of the same layer stack as Sample A with a slightly increased doping density at the interface. In addition, Sample B has a 0.5 µm wide (Ga,Mn)As injection contact, located at 4 µm distance to the 4 µm wide (Ga,Mn)As detection contact (see inset of Fig. 4.22b). The generated spin accumulation beneath the narrow contact with a spin diffusion length of 6 µm (corresponding spin lifetime of 15-20 ns, see below) can therefore be observed by measuring the non-local voltage signal between the 4 µm wide detection contact and a reference contact placed at a distance of 300 µm. In Fig. 4.22a we compare the non-local voltage signal from electrical spin injection (V_{nle}) to the optically induced signal V_{nlo}. Electrical spin injection is demonstrated by applying a negative voltage V_b to the narrow (Ga,Mn)As contact (red curve, −1 µA injection current). When decreasing the external magnetic field starting from +150 Oe, a jump of the non-local voltage signal was observed at -50 Oe, corresponding to the magnetization reversal of the 4 µm wide detection contact at the right. At this magnetic field value, the magnetization directions of injector and detector switch from a parallel to an antiparallel configuration. The corresponding change of the non-local voltage ΔV_{nle} is proportional to the spin accumulation in the GaAs channel [98]. At -100 Oe,

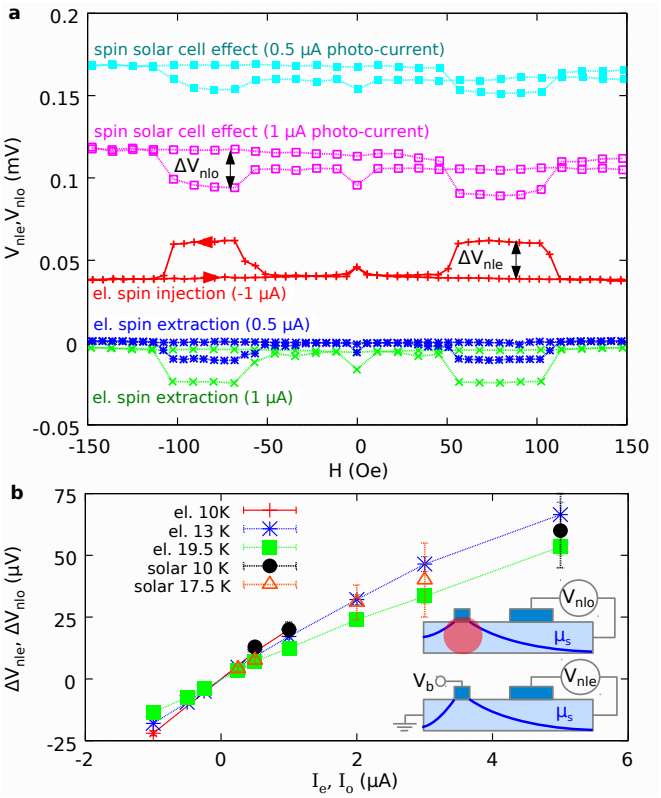

Figure 4.22: Electrical detection of the optically and electrically created spin accumulation in a non-local voltage geometry. The top figure shows the observed non-local voltage while sweeping the magnetic field along the z-direction (offset subtracted from spin solar cell curves for clarity: 0.2 mV and 0.6 mV respectively). The bottom figure illustrates the extracted spin valve signal ($\Delta V_{nle}, \Delta V_{nlo}$) from the solar cell effect and electrical spin injection versus the applied current or measured photo-current (adjusted by the laser intensity). The inset illustrates the measurement geometry for both cases.

when the narrow injector reverses its magnetization, both contacts are again in a parallel configuration and the non-local voltage signal returns to the starting value. The same occurs for +50 Oe and +100 Oe when sweeping the magnetic field back to +150 Oe. The small peak at zero magnetic field originates from dynamic nuclear polarization (DNP) that slightly depolarizes the spin accumulation [58, 59, 61–63]. The increase of the non-local voltage in the antiparallel configuration for electrical spin injection corresponds to a spin-up accumulation. In contrast, when reversing the bias voltage and now extracting spins, the spin valve signal ΔV_{nle} is also reversed, corresponding to a spin down accumulation as shown by the blue and green curve for the extraction currents of 0.5 µA and 1 µA.

If instead of applying an electrical voltage, the laser spot is placed below the narrow injection contact, the spin solar cell effect generates the spin accumulation, as illustrated in the upper pictogram of Fig. 4.22b. Two spin-valve curves are plotted in Fig. 4.22a (light blue and magenta curve), where the absolute value of the photo-current (0.5 µA and 1 µA, measured independently as sketched in Fig. 4.17c) reflects the different absorbed laser power. The larger noise level and slight drift can be ascribed to illumination and the limited long-term mechanical stability of the optical setup.

The qualitative comparison of the non-local voltage generated by the spin solar

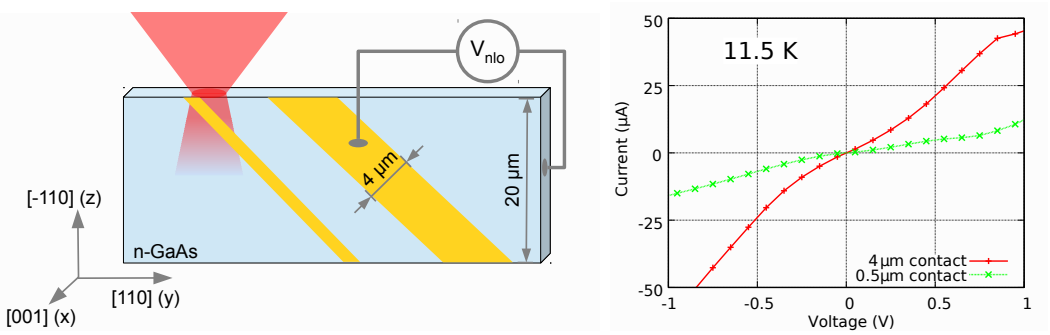

Figure 4.23.: Left: Geometry of Sample B from top view. Right: *I*-*V* characteristic at 11.5 K of the 0.5 µm wide and the 4 µm wide contact.

cell effect with the one observed for electrical spin injection clearly shows that the spin accumulation induced by illuminating the contact ($\propto \Delta V_{nlo}$) has the same sign as the spin accumulation resulting from electrical spin extraction ($\propto \Delta V_{nle}$) and the opposite sign compared to electrical spin injection (red curve, $\propto \Delta V_{nle}$). In Fig. 4.22b both spin valve signals ΔV_{nle} and ΔV_{nlo} are plotted versus the electrically applied current I_e or photo-current I_o, respectively. The data shows that the magnitude of the non-local signals is similar when the photo-current matches the electrically applied current. This suggests that the photo-current indeed reflects the laser-induced tunneling current, since it creates a similar spin accumulation as an electrically applied current. The same correlation between the photo-current and the generated spin accumulation is also indicated by the optical results shown in Fig. 4.19. Altogether, the excellent agreement of the sign and the amplitude of the spin accumulation with respect to the photo-current confirms the described mechanism of the spin solar cell effect.

For the electrical detection of the spin solar cell effect, the (Ga,Mn)As contacts of Sample B were patterned along the [100] direction with an angle of 45° to the mesa channel oriented along [110]. Fig. 4.23 shows on the left a sketch of the two (Ga,Mn)As contacts (yellow) from top view. The advantage of this geometry is on the one hand the reduction of stray-light or incoming laser-light on the detecting contact in the non-local voltage geometry (otherwise, due to the photo-voltaic effect a large offset voltage would be created even for very small light intensities). On the other hand the tilted contacts were used to check the penetration depth of the incident laser light as a function of the wavelength (see below in Fig. 4.27). Fig. 4.23 shows on the right the *I*-*V* characteristics for both contacts. In contrast to Sample A (see Fig. 4.30), a lower interface resistance and a more symmetric bias dependence is visible, indicating the larger doping density at the interface.

Fig. 4.24 shows on the left hand side the hysteresis curves measured magneto-optically when electrically injecting spins from the narrow (0.5 µm) and the wide contact (4 µm). The curves clearly show the different switching fields of the two

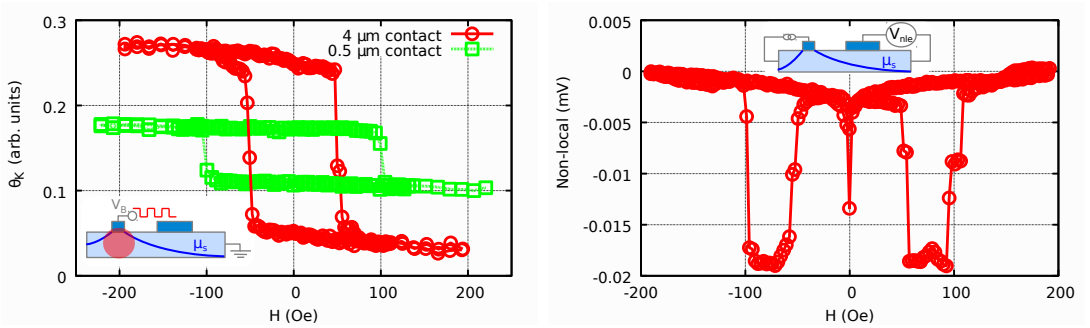

Figure 4.24.: Left: Kerr rotation in the n-GaAs channel vs. applied magnetic field (z-direction) for electrical spin injection from the 0.5 µm wide and the 4 µm wide contact at 11.5 K. Right: Detection of the electrically injected spins via the non-local voltage signal (see inset) with the same magnetic field sweep at 11 K.

contacts at 11.5 K when sweeping the external magnetic field along [-110] (z-direction). The switching fields of 50 Oe and 100 Oe together with the almost rectangular switching behavior are in good agreement with the spin valve signal from the electrical detection (Fig. 4.24 right). The fact that the remanent magnetization of both contacts is not 100% shows that the [-110] direction is not exactly the magnetic easy axis. Without external magnetic field the magnetization is therefore oriented at a certain angle ϕ to the [-110] direction, as discussed in Sec. 3.5.1. This angle can be estimated by measuring the depolarization of the spin accumulation in an out-of-plane magnetic field along the x-direction (Hanle measurement). Due to the tilted magnetization the injected spins either start to precess into the laser beam axis or away from it, depending on the magnetic field direction. This must result in asymmetric Hanle curves when detected by pMOKE which are illustrated for both contacts in Fig. 4.25.

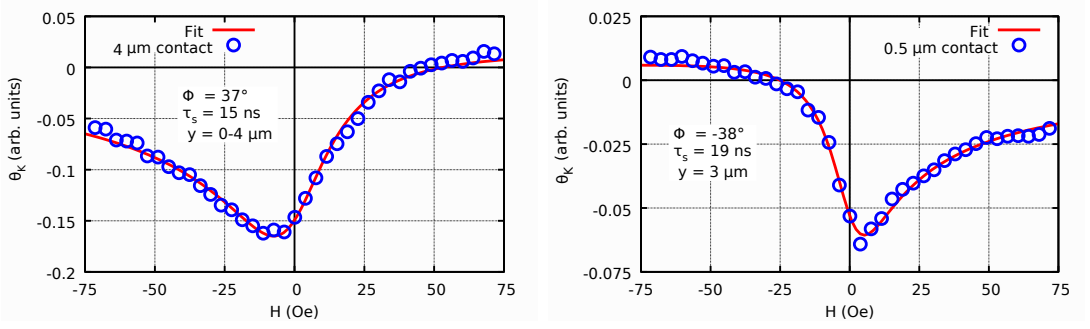

Figure 4.25.: Optically detected Hanle curves for spin injection from the wide (-1 V applied) and the narrow contact (-0.5 V applied) showing the spin lifetime and the tilt ϕ of the magnetization with respect to the laser beam axis [-110], as obtained from a numerical fit according to Eq. (3.3) and Eq. (3.4).

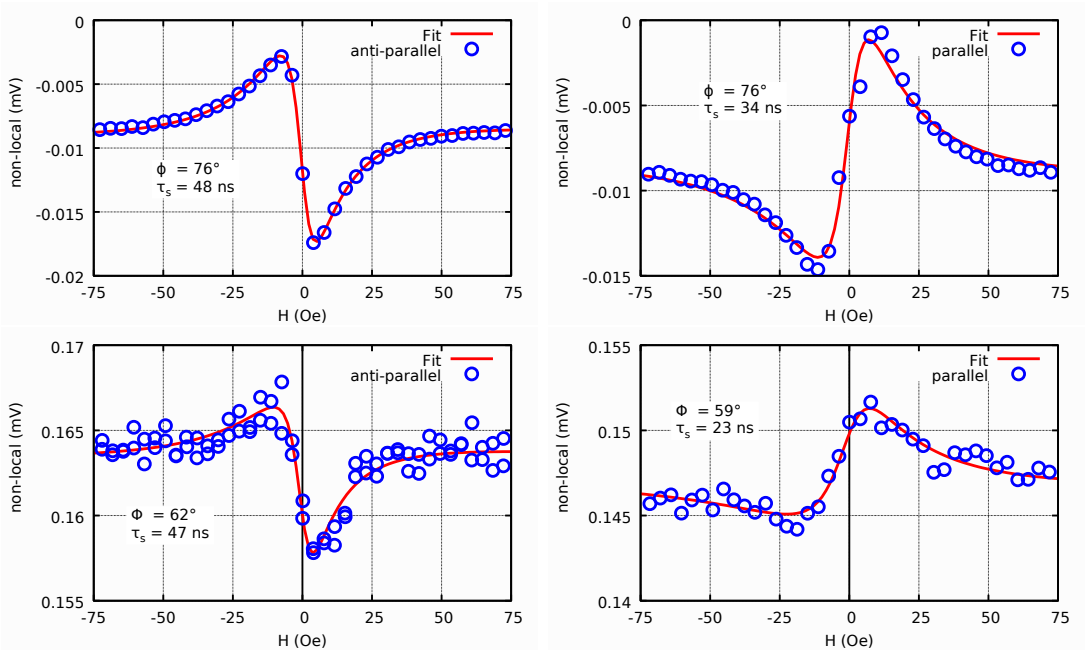

Figure 4.26.: Hanle measurements in the non-local voltage geometry for "parallel" and "anti-parallel" configuration of both contact magnetizations. Upper figures show electrical spin injection, the bottom figures show the spin solar cell effect.

Numerical fitting the asymmetric shape of the Hanle curves in Fig. 4.25 yields a magnetization tilt ϕ of 37° for the wide contact and -38° for the narrow contact. Thus, the magnetization of the narrow contact is oriented almost along the patterned contact direction [100] in remanence, which can be explained by the patterning induced anisotropy relevant for narrow contacts discussed in Refs. [49,50], and the magnetization of the wide contact is tilted in the opposite direction, almost along [010]. Consequently, when detecting the spin accumulation generated by the narrow contact electrically using the wide contact as detector, we have an angle between the spin directions of about 75°. Thus, Hanle measurements in the non-local voltage geometry show a strong asymmetry, illustrated in Fig. 4.26. The extracted angle of 76° between the magnetization of both contacts matches with the results obtained by optical detection. The bottom figures in Fig. 4.26 illustrate the electrically detected Hanle signal when generating the spins via the solar cell effect. The graphs again show the strong asymmetry between the contact magnetizations. The reason for the slightly smaller angle ($\sim$ 60°) probably arises from the fact that the generated spins from the solar cell effect are mostly created at the contact edge. The extracted spin lifetime from the electrical detection is usually affected by dynamic nuclear polarization (DNP) [59]. From the optical detection a spin lifetime of 15-20 ns results that should be more reliable since DNP is eliminated in this measurement technique due to the fast periodic reversal of the magnetization direction (see Sec. 3.5.2). The offset-voltage

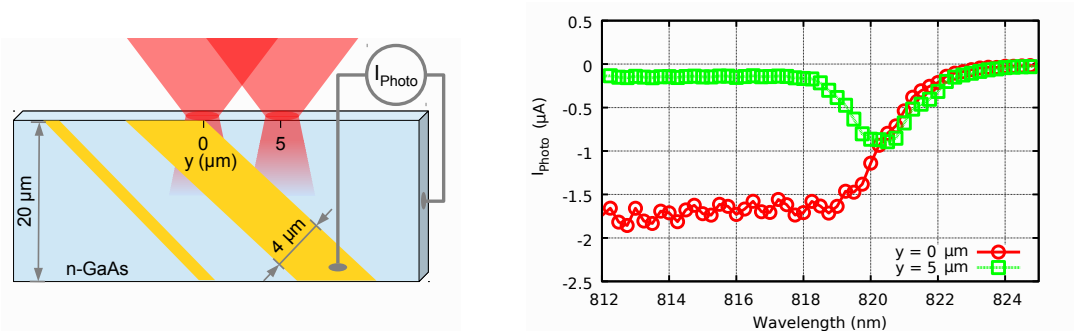

Figure 4.27.: Wavelength dependence of the photo-current (right) with the laser spot a two different positions (illustrated left).

which occurs in the non-local voltage signal also for electrical spin injection may originate on the one hand from a small nonuniform current that passes the detecting contact, which can be shown in 2D simulations (see Sec. 4.2), or from thermo-electric effects due to a small temperature gradient created by the applied current [99].

In addition to the laser-induced spin extraction process also the ferromagnetic proximity polarization (FPP) of the optically excited electrons may be observed [100, 101]. Using time-resolved Faraday rotation, the authors of Ref. [100] and [101] observe a spontaneous spin polarization in n-GaAs close to a ferromagnetic layer when illuminating with linearly polarized light. The origin of FPP is suggested to be spin-dependent reflection at the interface [102]. In our experiments, no significant spin polarization could be observed in a reference sample with a larger doping density ($n = 7 \cdot 10^{16}\,cm^{-3}$) and hence a much smaller photo-voltaic effect. The proximity effect on the other hand should not depend on doping density. Altogether, the excellent agreement of the optical and electrical measurements with the photo-current and with electrical spin injection shows that the spin solar cell effect must be the dominant mechanism in our device.

Finally, Fig. 4.27 illustrates the wavelength dependence of the photo-current. The two positions of the laser spot are illustrated in Fig. 4.27 on the left hand side. The absorbed laser power was already discussed in Sec. 3.4. At laser spot position $y = 0\,\mu m$, the photo-current begins to drop above 819 nm, indicating that the penetration depth of the transmitted laser beam is exceeding the contact region. In contrast, at position $y = 5\,\mu m$, the incoming light has to first penetrate 5 µm of GaAs before reaching the contact area. Here the photo-current is almost zero up to 818 nm and has its maximum at 820 nm. This shows that the penetration depth is below 5 µm for wavelengths below 818 nm. Above 822 nm the photo-current approaches zero for both cases, indicating that the photon energy becomes smaller than the bandgap. Thus, the absorption edge lies in the energy range of 1.51 eV at 19 K. This is consistent with the observed Kerr spectra illustrated in Fig. 4.21

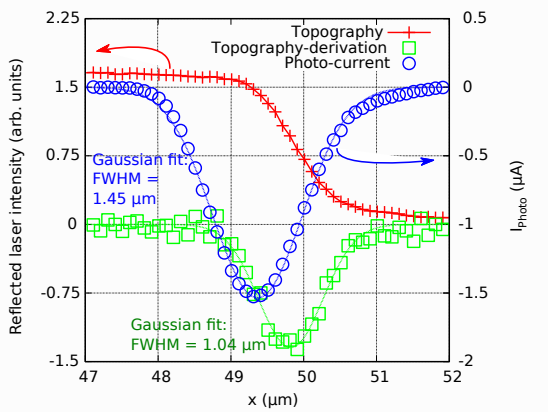

Figure 4.28.: Linescan of the reflected laser intensity and photo-current across the sample edge (x-direction) at 19 K (Sample B, y = 0 µm, 816 nm - 35 µW/µm^2 absorbed power density). The derivation of the topography gives the laser spot profile.

and 4.31, showing a sign reversal at about 818 nm.

Fig. 4.28 shows the reflected light intensity while performing a line-scan across the sample edge along the x-direction (Sample B, y = 0 µm). The derivative of this curve (green curve) gives the laser spot profile with a FWHM of 1.04 µm from a Gaussian fit (see Sec. 3.4). In addition the observed photo-current is illustrated with a FWHM of 1.45 µm. This broadening is probably due to the penetration depth of the light and the re-emission of photons by the recombination of electron-hole pairs. In addition the extended band-bending region leads to a widening of this curve. The maximum of the photo-current is shifted towards the left since the active region, i.e. the band-bending region is not at the sample edge close to x = 50 µm, but shifted to the left due to the 150 nm thick Au layer and the 50 nm thick (Ga,Mn)As layer of the contact.

4.3.3. Spin photodiode

The optical and electrical results shown in the previous sections clearly demonstrate the experimental verification of a spin generating solar cell, where spin accumulation in the GaAs is created solely by light. According to the explanation given in Fig. 4.16, the laser-induced spin extraction process can be eliminated by applying a reverse bias, i.e. a negative voltage to the (Ga,Mn)As contact. The negative bias increases the depletion zone of the p-n-junction and suppresses the tunneling current. However, due to the negative bias, the optically excited spin polarized electrons in the (Ga,Mn)As conduction band are driven into the n-GaAs channel. Fig. 4.29 shows the resulting "spin photodiode effect" via a linescan of the Kerr rotation along the n-GaAs channel while applying -10 V to the (Ga,Mn)As contact. Again, as for the spin solar cell effect (see Fig. 4.19),

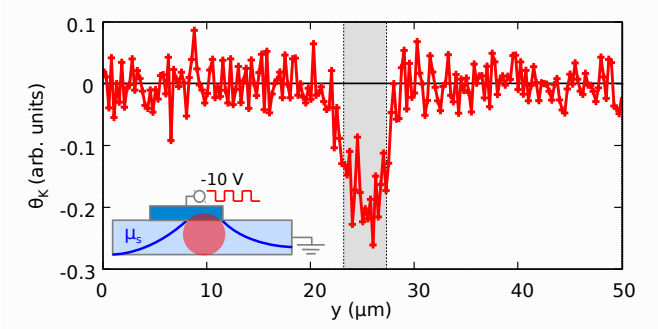

Figure 4.29.: Kerr rotation along the n-GaAs channel while applying a negative bias voltage to the (Ga,Mn)As contact illustrating the spin photodiode effect (815 nm - 103 $\mu W/\mu m^2$). As for the solar cell effect, a spin accumulation can only be observed when the laser spot is located at the contact area.

no spin accumulation can be observed unless the laser spot enters the contact region. However, in contrast to the spin solar cell, this effect creates a spin up accumulation (negative signal in Fig. 4.29), as expected from the explanation illustrated in Fig. 4.16c.

In the following, we show that no additional spin accumulation is generated by the negative bias voltage used for the observation of the spin photodiode effect. Usually, applying a negative bias results in injecting spins from the (Ga,Mn)As into the n-GaAs. To disable electrical spin injection in reverse bias, we adjusted the doping profile of this particular sample (Sample A) such that the tunnel diode almost blocks the current in reverse direction. The I-V characteristic of Sample A is shown in Fig. 4.30 on the left hand side, which resembles the I-V curve of an ordinary diode blocking the current in reverse direction at low temperatures. In conjunction with the decreasing spin injection efficiency with increasing negative bias voltage [45], the spin accumulation from electrical spin injection can be neglected for this sample. This is illustrated in Fig. 4.30 on the right hand side where the bias dependence of the Kerr signal is shown for three relatively low laser powers. In the negative bias range the spin photodiode effect appears only for the largest laser power (red curve in Fig. 4.30). The absence of bias dependence shows that the laser power and not the voltage is decisive for the generated spin accumulation. When reducing the laser power, the Kerr rotation decreases in the negative bias range, as expected, until it becomes zero for the lowest laser power (blue curve). In contrast, for positive bias voltages, electrical spin extraction occurs resulting in a visible Kerr rotation even for the lowest laser power (shaded area in Fig. 4.30). This proves that no spin accumulation is generated by electrical spin injection, i.e., under reverse bias. Thus, the negative voltage can be used to directly observe the spin photodiode effect, where the photo-excited spin-polarized carriers from the 50 nm thick (Ga,Mn)As layer are driven into the GaAs (see sketch in Fig. 4.16c).

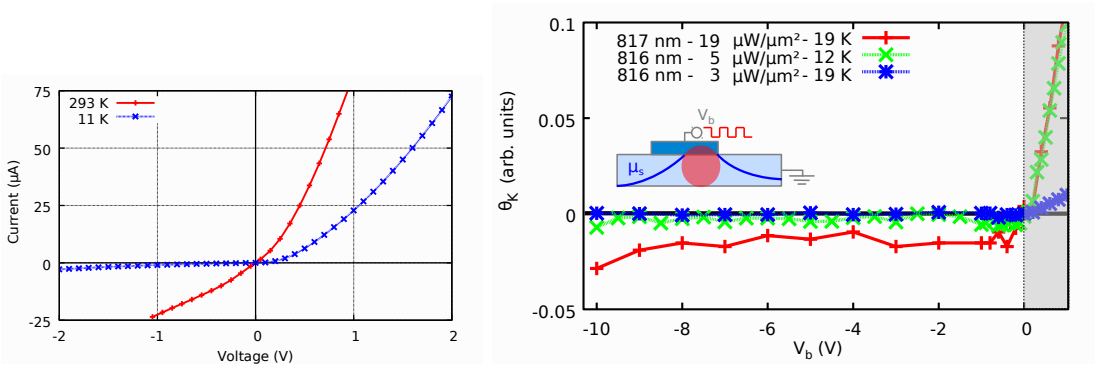

Figure 4.30.: Left: *I-V* characteristic of the tunnel diode (Sample A). Right: Bias dependence of the spin photodiode effect (negative bias range) for low laser intensities. For positive voltages electrical spin extraction occurs (shaded region).

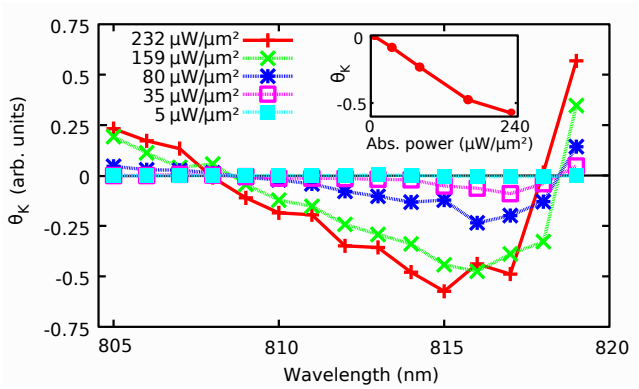

Figure 4.31.: Illustration of the spin photodiode effect via the Kerr spectra for various laser intensities and an applied bias voltage of -10 V. The inset shows the maximum Kerr rotation of each spectrum versus the laser power.

Fig. 4.31 illustrates the laser power dependence of the spin photodiode effect via the Kerr spectra in the n-GaAs beneath the contact. The almost linear laser power dependence is shown in the inset, where the maximum Kerr rotation of each spectrum is plotted vs. laser power. In contrast to the reference Kerr spectra shown in Fig. 4.21, a reduced wavelength shift of the spectra with increasing power density is observed. Only for the largest laser intensity the zero-crossing of the spectrum is slightly shifted to lower wavelengths by 0.5 nm. This confirms that now the spin accumulation is generated when the negative bias is applied, which also broadens the band bending in the n-GaAs and shifts the optically excited electrons away. Thus the increase of the absorption edge due to the additionally generated electrons in the conduction band with increasing laser power is less visible in this geometry.

The spin photodiode effect was already predicted and calculated for a similar case, where the p-side of a nonmagnetic p-n-junction was proposed to be illu-

minated with circularly polarized light [103]. By applying a negative voltage to the junction, it acts as a spin photodiode, converting light into a spin-polarized charge current. In principle the effect should also be present without a negative bias, since some of the optically excited spins in the (Ga,Mn)As should reach the GaAs channel by diffusion. However, the effect seems to be rather small without negative bias since its manifestation is not observed when detecting the spin solar cell effect (see Fig. 4.22).

4.3.4. Towards spintronic application

Finally we would like to discuss possible applications utilizing both the spin solar cell effect and the spin photodiode effect. The presented experimental verification of a spin solar cell and a spin photodiode provides a potential for future spintronic applications. Both effects are prototypical for the basic idea of semiconductor spintronics, where additional features via the spin degree of freedom are added to a classical electronic device. The effects can be used to create a photo-sensor which converts light not only into a voltage or a current, but additionally into a spin current and a spin accumulation. In order to make use of this second information provided by a potential spin photo-sensor, it is necessary to electrically read out the generated spin current. The inverse Spin Hall effect (ISHE) is a potential candidate since it is only sensitive to the spin polarization [95]. The usefulness of the spin Hall effect was recently reviewed by Jungwirth et al. [96]. As a consequence the photo-sensor is capable of controlling an event depending on light intensity and magnetization direction. The magnetization direction itself could be electrically set via the spin transfer torque effect [104–108] in a nano-sized electrode. In contrast to an ordinary photo-sensor, the spin photo-sensor can create two independent outputs (photo-voltage/photo-current and ISHE voltage), controlled by two independent inputs (magnetization direction and light intensity).

Maybe even more important is the very general mechanism behind the spin solar cell effect: a potential device does not require a p-type ferromagnetic semiconductor. In fact any ferromagnetic metal with the Fermi energy within the band gap of the semiconductor could generate the same effect via a Schottky barrier. In addition also a direct semiconductor as GaAs is not necessary, the same working principle should hold for silicon or other semiconductors without direct bandgap as well. Since room-temperature spin injection from various ferromagnetic metals into GaAs [109–113] or Si [114–117] was already achieved, all requirements for a working room-temperature spin solar cell are fulfilled. This enables a new and efficient way for the optical generation of spins in a large material class using unpolarized light, independent from optical selection rules and not limited to specific wavelengths.

4.4. Alternative spin injection methods from Fe into n-GaAs

The efficient injection of spins into semiconductors is one of the main goals within the large field of semiconductor spintronics. Besides the established methods of optical spin pumping (see Sec. 2.1) and electrical spin injection, the previous section has shown that the spin solar cell and the spin photodiode effect provide an efficient way to generate spins in semiconductors. Recently, thermal spin injection from Fe into Si was demonstrated via a temperature gradient across the tunnel barrier between the Fe and the Si layer [88]. The effect was analyzed by electrically probing the depolarization of the generated spin accumulation in a three-terminal geometry [114]. In addition to thermal spin injection, spin pumping via magnetization dynamics is another method that allows to generate pure spin currents from a ferromagnetic layer into the connected nonmagnetic layers. The effect is usually observed in metals by measuring the generated spin current from the ferromagnetic layer in a connected Pt stripe via the inverse Spin Hall effect [85]. Recently, spin pumping into n- and p-doped GaAs could be observed, however, with an unexpected large signal [86].

In the following, attempts to observe thermal spin injection and spin pumping into n-GaAs are discussed. Experiments on thermal spin injection were performed on two Fe/n-GaAs samples at low temperature (Samples A and B). On Sample A also spin pumping was investigated with the attempt to optically observe spin pumping into GaAs. The measurements could be realized with the following contact geometry, illustrated in Fig. 4.32. Here, the sample is already cleaved along the [1-10] direction across the mesa channel and the ferromagnetic pads. For the patterning, first of all, a 200 µm wide mesa channel (n-GaAs channel) was defined on the Fe/GaAs sample with optical lithography. After the lift-off process the photoresist was solely left on the 200 µm wide mesa stripe in the center of the sample. The Au and Fe layer from the exposed area were then removed by Ar ion etching. After that the highly doped GaAs layer at the interface and the 2 µm thick n-GaAs layer were removed by chemical etching so that solely the semi-insulating GaAs substrate remains. Three Fe contacts on the mesa channel were then defined in a similar way by optical lithography and etching by removing the Au, Fe and highly doped GaAs layer on the mesa channel except for the contact areas. This confines the electron transport and spin accumulation to the 200 µm wide n-GaAs channel (see Fig. 4.32). As a last step Au bonding pads for each contact were evaporated, also defined by optical lithography. The fabricated lateral device has a 200 µm wide mesa channel, one 50 µm×200 µm U-shaped contact in the middle and two 20 µm wide contacts located at a distance of 650 µm to the middle contact. Finally the sample was cleaved across the mesa channel cutting the contact length in half (100 µm, see Fig. 4.32).

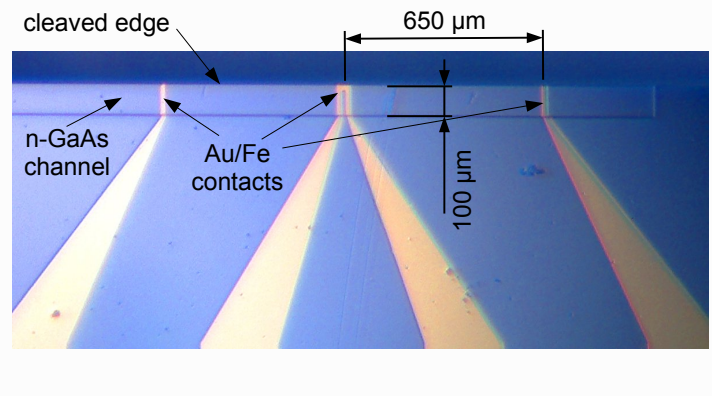

Figure 4.32.: Photo (optical microscopy) of the cleaved sample illustrating the contact geometry.

The 2 µm thick n-GaAs channel for the electron transport and spin accumulation has a nominal doping density of $1.4 \cdot 10^{18}\,\mathrm{cm}^{-3}$. Spin injecting contacts are formed by a 3 nm thick layer of Fe, a 15 nm thick layer of n^{++}-GaAs with a nominal doping density of $6 \cdot 10^{18}\,\mathrm{cm}^{-3}$ and a 15 nm thick $n^{++} \rightarrow n$ transition layer. Together these layers form a narrow Schottky barrier that enables tunneling of spin-polarized electrons between the Fe and the GaAs channel, as described in Sec. 2.5.

4.4.1. Electrical spin injection

Before discussing thermal spin injection and spin pumping into GaAs, electrical spin injection and extraction is demonstrated on Sample A. Fig. 4.33 shows one-dimensional linescans of the Kerr rotation along the GaAs channel for spin injection ($V_b = -3\,V$, red) and extraction ($V_b = 3\,V$, green) at 11 K. The bias voltage was applied between the U-type contact and the 20 µm wide contact on the left. Due to the superposition of electron drift and spin diffusion, the effective decay length of the spin accumulation left to the injecting contact results in 20 µm for the -3V-data. In contrast, for spin extraction, the effective decay length on this side of the contact is strongly reduced. Due to the large electric field, which is still present beneath the contact area (see Sec. 4.2), the spin accumulation is driven towards the right even below the contact area. In addition, Fig. 4.33 shows the spin density distribution while applying a small bias voltage of -100 mV. The observed spin accumulation for the -100mV-data corresponds to a current density across the interface of $1.5 \cdot 10^4\,\mathrm{A/m^2}$. Assuming the current polarization being well below 50%, as discussed in Sec. 2.5.2, the capability is given to detect spin currents in the order of $0.5 \cdot 10^4\,\mathrm{A/m^2}$. Due to the narrow tunnel barrier, this current density corresponds to a voltage drop across the interface of only 0.7 mV (total current of 65 µA).

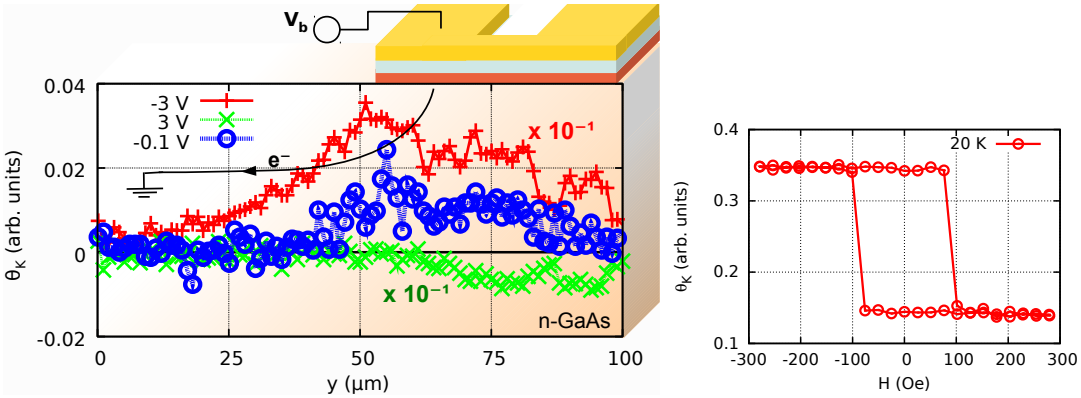

Figure 4.33.: Spin injection/extracion on an Fe contact at 11 K. Left: Kerr rotation along the n-GaAs channel for electrical spin injection (-3 V, -0.1 V) and spin extraction (3 V). The 3V-data and -3V-data are scaled by a factor of 10. Right: Hysteresis loop of the injected spin accumulation reproducing the magnetization reversal of the Fe contact.

Fig. 4.34 shows the I-V characteristic of the Schottky contact. The current is plotted as a function of the voltage drop across the barrier of the U-shaped contact, which is detected via the second 20 µm wide contact on the right hand side of the U-type contact. Due to the high doping level the characteristic looks almost ohmic, only a slight reduction of the interface resistance with increasing bias voltage is visible at low temperature (from 10.5 Ω to 8 Ω). For a contact area of about $40 \times 100\,\mu m^2$, this results in an area resistance of about $R_c \approx 4 \cdot 10^{-8}\,\Omega m^2$. The advantage of a narrow tunnel barrier, i.e. a low interface resistance, is the possibility to yield relatively large currents from small potential differences across the barrier. This is especially useful for the generation of pure spin currents across the interface, which is easier to achieve the smaller the interface resistance is [118].

Fig. 4.35 shows a Hanle measurement at position $y = 30\,\mu m$ i.e. about 20 µm outside the contact for a negative applied bias voltage of -5 V. The numerical fit yields a spin lifetime of 8 ns. Since the injection-detection distances are not

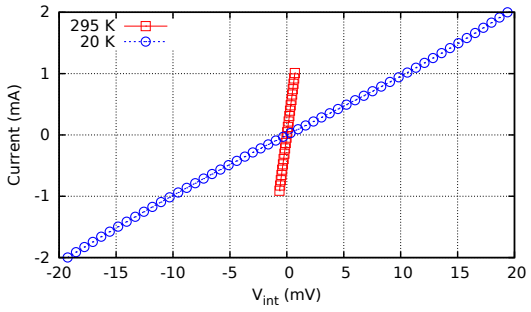

Figure 4.34: I-V characteristic of the Schottky barrier where the current is plotted against the voltage drop across the Schottky barrier. The applied bias range for the 20 K data goes from $V_b = -2.75$ V to $V_b = +2.75$ V.

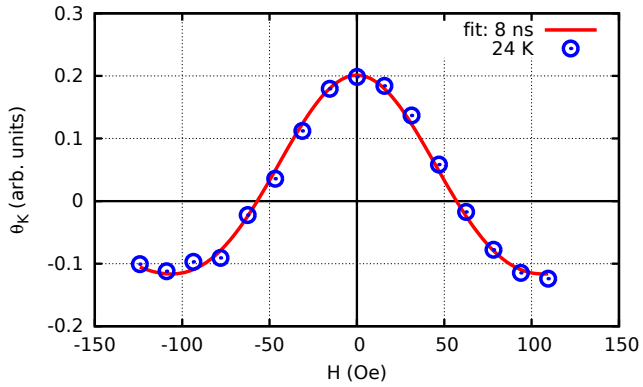

Figure 4.35.: Hanle Depolarization for electrical spin injection at position y = 30 µm and $V_b = -5$ V. The fit yields a spin lifetime of 8 ns.

well defined due to the large contact area and the small interface resistance (see Sec. 4.1.4), the value can be seen as a rough estimation. The spin diffusion length of 7 µm, which is an important fitting parameter, was extracted from linescans as shown in Fig. 4.33: from the effective spin decay length (due to the superposition of drift and diffusion) on the left hand side of the contact for different applied voltages the spin diffusion length and the ratio of drift over diffusion can be estimated (see Sec. 4.1.4). Details about Hanle measurements and the fitting procedure are given in Sec. 3.5.

4.4.2. Thermal spin injection

The possibility to generate spin currents by temperature gradients might be useful for future spintronic devices and also could help to improve energy consumption. The fact that a spin accumulation can be created by a small temperature gradient across a tunnel barrier between Si and Fe was recently shown [88]. The origin of the so-called spin Seebeck tunneling is illustrated in Fig. 4.36. When

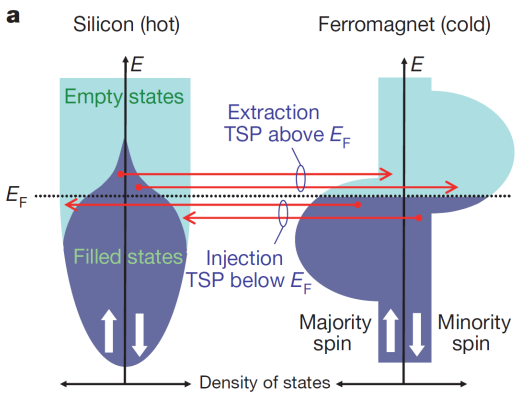

Figure 4.36: Origin of the Seebeck spin tunneling (from [88]). The temperature difference generates electron extraction above the Fermi level and electron injection below the Fermi energy. Both currents are equal but have a different tunneling spin polarization (TSP) so that a spin accumulation in the semiconductor is created (here Si).

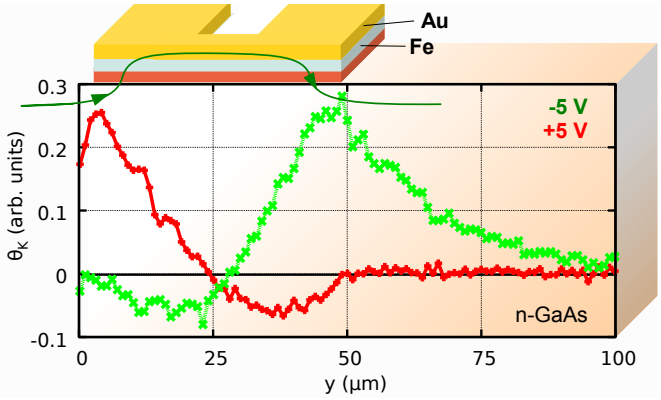

Figure 4.37: One-dimensional linescan of the Kerr rotation along the n-GaAs channel when heating the channel with an e^--current from right to left (+5 V) and vice versa (-5 V).

heating the semiconductor and thus increasing its temperature, the filling of the density of states is changed due to the Fermi-Dirac statistics. Electrons with an energy above the Fermi level are now occupied, in conjunction with empty states below the Fermi level. Hence, by connecting the hot semiconductor with a cold ferromagnet, electrons above the Fermi level are flowing into the ferromagnet while electrons below the Fermi level are flowing from the ferromagnet into the semiconductor. The difference between both currents builds up a Seebeck voltage across the materials until no net charge current is flowing in equilibrium. However, even for equally strong electron currents a spin current can exist if the tunneling spin polarization (TSP) above and below the Fermi level is different. Thus, a temperature gradient can produce a pure spin current across the interface and hence a spin accumulation in the semiconductor.

Fig. 4.37 shows a linescan of the Kerr rotation along the n-GaAs channel below the U-type contact when electrically heating the n-GaAs by applying ±5 V between the two outer contacts (see Fig. 4.32). For the measurements a square-wave bias voltage alternating between 0 V and +5 V or −5 V was used. Thus, optical detection with a lock-in technique as for electrical spin injection is possible (see Sec. 3.2). The results show an opposite behavior for both current directions, indicating that the spin accumulation is not created by thermal effects. Instead, the observation suggests that part of the current is flowing through the Fe contact as sketched by the green current line. Thus, when applying a current along the n-GaAs channel, spins are injected at one side of the contact and extracted at the other side and vise versa for the opposite current direction. Regarding the low interface resistance of the contact (9 Ω) with respect to the channel resistance (38 Ω for the contact width), this current shunting effect can be expected. Consequently, thermal spin injection by electrically heating the n-GaAs channel cannot be directly observed.

Nevertheless, electrical heating of the Fe layer without driving a current into the GaAs should work due to the low resistance of the 140 nm thick Au layer, sputtered on the Fe contact. However, no significant spin accumulation could be

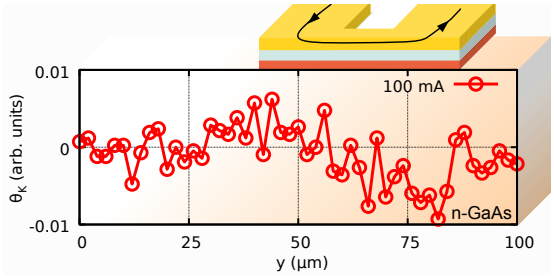

Figure 4.38.: One-dimensional linescan of the Kerr rotation along the n-GaAs channel while driving a heating current along the Fe contact.

detected in the GaAs when heating the Au/Fe layer with currents up to 100 mA (see Fig. 4.38). The small negative Kerr rotation beneath the right part of the Fe contact and the small positive Kerr rotation beneath the left part of the Fe contact can be attributed to a different effect discussed below. For a current of 100 mA, the resistance of the Au leads connecting the U-type contact increases by Joule heating from 9.6 Ω to 10 Ω, corresponding to an average temperature increase of 0.5 K. Hence, due to the confinement of the Au pattern at the contact region, a larger temperature increase can be expected there. Altogether, for this temperature gradient in the order of a few K across the interface, which is similar to the one in Ref. [88] where a thermally induced spin accumulation in Si was detected, no significant thermal spin injection can be observed. This will be investigated in more detail on Sample B in the following.

A reason for the absence of thermally induced spin polarization in the GaAs might be a depolarizing magnetic field arising from the heating current. However, this can be ruled out by simultaneously injecting spins while driving the heating current, for instance by grounding one of the 20 µm wide contacts so that part of the heating current along the U-shaped contact flows into the n-GaAs. Then, a large spin accumulation is still observable as shown in a similar way below.

In order to even more localize the Joule heating, Sample B was prepared with a reduced thickness of the Au layer above part of the Fe contact. In addition, also beneficial for thermal spin injection, the interface resistance of Sample B is a factor 3.5 lower than for Sample A. The layer stack and the contact geometry is identical to Sample A. Fig. 4.39 illustrates the observed spin density distribution for both temperature gradients - when driving a current through the n-GaAs channel (left) and along the Fe contact (right). When heating the n-GaAs channel the same behavior occurs as for Sample A, where part of the current is shunting the Fe contact (see Fig. 4.37). In contrast to Sample A, the current shunting effect in Sample B also dominates when heating the Fe contact, as shown in Fig. 4.39 on the right hand side. This originates on the one hand from the lower interface resistance compared to Sample A, on the other hand from the reduced Au layer thickness in the middle part of the Fe contact (sketched in Fig. 4.39). Both

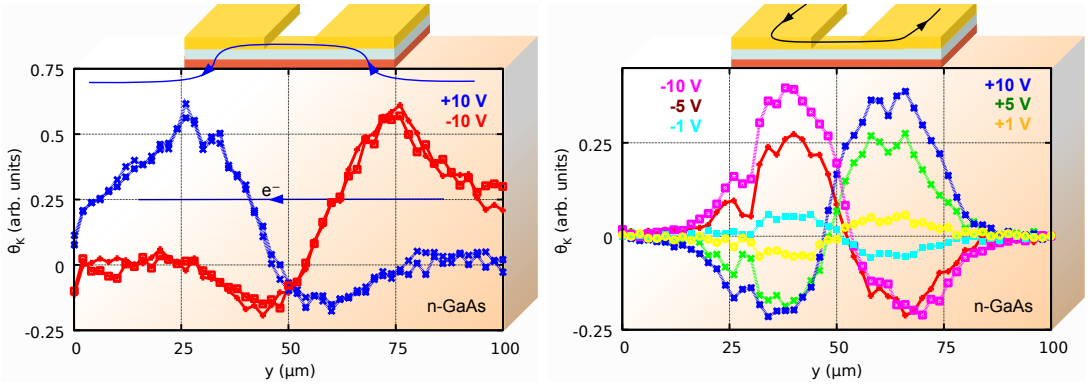

Figure 4.39.: Kerr rotation along the n-GaAs channel when passing the heating current through the GaAs channel (left) and passing the heating current through the contact layers (right). The dip at y = 28 µm corresponds to an impurity on the cleaved edge plane.

figures nicely show that, when reversing the current direction, the spin density distribution is mirrored with respect to the contact center position at y = 50 µm. This is shown in Fig. 4.39 on the right hand side for ±10, ±5 and ±1 V. For ±1 V (yellow, light blue) the absolute spin accumulation from spin injection and spin extraction is similar. However, with increasing voltage spin injection becomes more effective, resulting in an asymmetric spin density distribution. This is also clearly shown in Fig. 4.39 on the left when heating the n-GaAs channel. The behavior is consistent with the bias dependence of direct electrical spin injection from the U-shaped contact, shown in Fig. 4.40. Here, the bias voltage was applied between the U-type contact and the contact on the right. Around zero voltage, the Kerr signal has an almost linear behavior. For larger absolute bias voltages spin injection becomes more efficient than spin extraction. The linear behavior of the injected spin polarization between -1 V and 1 V shows that the current spin polarization, i.e., the tunneling spin polarization (TSP) is constant for small bias voltages. Since for efficient thermal spin injection a strong variation of TSP

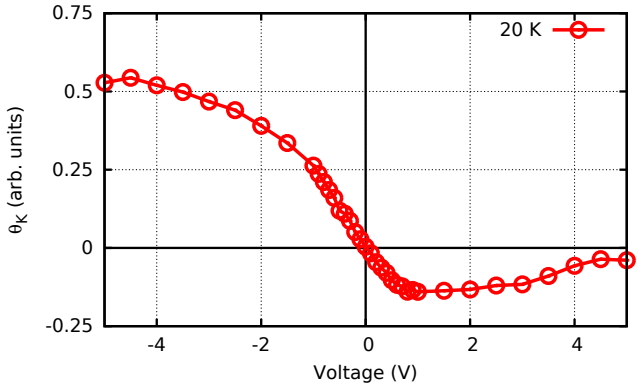

Figure 4.40: Bias dependence of the electrically injected spin accumulation by applying a voltage between the U-shaped contact and the contact on the right hand side. The signal was observed beneath the contact area of Sample B at y = 70 µm (see Fig. 4.39).

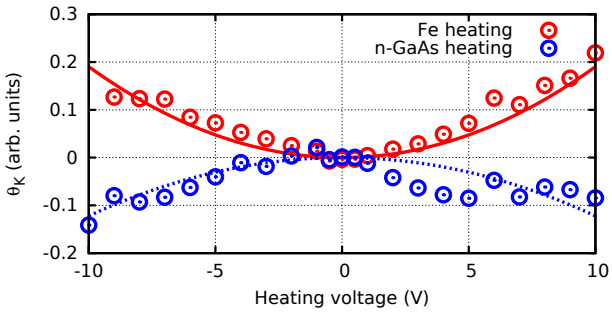

Figure 4.41.: Observed spin accumulation at y = 50 µm (see Fig. 4.39) for both heating currents.

above and below the Fermi energy is necessary (see Fig. 4.36), only a small spin current can be expected from a temperature gradient on this sample.

Due to the greatly reduced Au layer thickness in the middle part of the Fe contact on Sample B (5 nm instead of 140 nm), a much larger temperature increase with respect to Sample A can be expected when heating the Fe contact (±10 V corresponds to a current of 60 mA along the Fe contact). However, with this approach the current shunting effect dominates and no significant spin accumulation due to the thermal gradient can be extracted from the data.

It is worth noting that the current shunting effect can easily be misinterpreted when the spin polarization is only observed beneath the contact center. Fig. 4.41 shows the Kerr rotation at y-position 50 µm while sweeping the heating current either along the n-GaAs channel (blue) or along the Fe contact (red). The resulting sign reversal and the quadratic behavior is also expected from thermal spin injection. However, the reason for the sign reversal of the spin polarization at this position is the influence of the electric field in the GaAs on the spin accumulation: when heating the n-GaAs channel, the electric field drives the **extracted** spin accumulation towards the contact center, independent of the current direction. Therefore a negative Kerr rotation at the center position is observed when heating the GaAs channel. In contrast, when heating the Au/Fe layer, the electric field in the GaAs shifts the **injected** spins towards the contact center, again for both current directions. Hence, a positive Kerr rotation is observed at this position. Thus, if the spin polarization is only determined at y-position 50 µm, the result can be spuriously interpreted as a thermal spin injection effect as shown in Fig. 4.41. The parabolic shape can be qualitatively explained by the current density across the interface and the electric field in the GaAs, which both increase linearly with the applied heating voltage and both linearly increase the spin accumulation beneath the contact center.

When detecting the spin accumulation in a 3-terminal geometry the same side effect may appear, since the 3-terminal detection method probes the spin ac-

cumulation beneath the whole contact area. Given that spin injection is more efficient than spin extraction for the presented samples, one would expect the current shunting effect to generate more majority spins beneath the contact area for both cases - when heating the semiconductor channel and the ferromagnetic contact. Hence, no sign reversal is expected from current shunting when reversing the temperature gradient. This argument is also used in the supplementary material of Ref. [88] in order to rule out the influence of current shunting on the observed signal. However, due to the influence of the electric field when heating the channel, the extracted spin accumulation is pushed beneath the contact area at the expense of the injected spin accumulation that is shifted out of the contact area (see Fig. 4.39). In this manner a minority spin accumulation may be detected via 3-terminal when heating the channel. Thus, the expected sign reversal when reversing the thermal gradient may also occur due to this side-effect (see Fig. 4.41). In Ref. [88], the current shunting effect was ruled out for several reasons, e.g. the large interface resistance ($3 \cdot 10^7\,\Omega\mu\mathrm{m}^2$). However, here we show that a sign reversal of the spin accumulation by reversing the temperature gradient can be produced without thermal spin injection nevertheless.

In a recent theoretical comparison between electrical spin injection and thermal spin injection [118] it is shown that beside the importance of a narrow tunnel barrier, also the spin polarization of the Seebeck coefficient is decisive for the resulting spin accumulation. The presented results indicate that the spin Seebeck coefficient, i.e. the difference of the Seebeck coefficients for spin up and spin down electrons for the given Fe/n-GaAs Schottky barrier is too small. Since spin currents in the order of $5 \cdot 10^3\,\mathrm{A/m}^2$ can be easily observed (see Fig. 4.33), one can conclude that the spin current generated by the applied thermal gradient across the barrier must be below $5 \cdot 10^3\,\mathrm{A/m}^2$. Based on this experimental limit, the required spin Seebeck coefficient necessary to observe thermal spin injection can be estimated. The following estimation also provides an upper limit for the spin Seebeck coefficients in Sample A and B.

For electrical spin injection, the spin accumulation in the GaAs at the interface can be described by [17]

$$\mu_s^{el} = R_N P_\Sigma j, \tag{4.3}$$

where $R_N = \rho_N \cdot L_s$ is the effective resistance of the n-GaAs, P_Σ the spin polarization of the tunnel barrier conductivity and j the current density. The spin accumulation from thermal spin injection can be described by [119]

$$\mu_s^{th} = R_N S_{sc}(1 - P_\Sigma^2)\Delta T_c/(2\mathcal{R}_c). \tag{4.4}$$

$S_{sc} = S_{\uparrow c} - S_{\downarrow c}$ is the spin Seebeck coefficient of the junction, ΔT_c the temperature drop across the tunnel barrier and $\mathcal{R}_c$ the resistance of the junction, dominated by the tunnel barrier.

By replacing the current density j with the voltage drop across the barrier ΔV_c and the barrier resistance $\mathcal{R}_c$ in Eq. (4.3), the electrically generated spin accumulation as a function of the potential difference ΔV_c is given by

$$\mu_s^{el} = R_N P_\Sigma \Delta V_c / \mathcal{R}_c. \tag{4.5}$$

In order to yield the same spin accumulation from thermal spin injection we can combine Eq. (4.4) and (4.5):

$$S_{sc} = 2P_\Sigma \Delta V_c / [\Delta T_c (1 - P_\Sigma^2)] \tag{4.6}$$

This equation now describes the spin Seebeck coefficient that is necessary to create the same spin accumulation from thermal spin injection (with a temperature gradient of ΔT_c) and electrical spin injection (with a potential drop of ΔV_c across the tunnel barrier). This allows to estimate the required spin Seebeck coefficient for a given temperature gradient in order to generate an observable spin accumulation. For Sample A electrical spin injection with a current density corresponding to a voltage drop ΔV_c of 1 mV can be easily detected. Assuming a temperature gradient of 10 K across the tunnel barrier for Sample A, a spin Seebeck coefficient in the order of 0.1 mV/K is needed to observe the same spin accumulation as for electrical spin injection with a voltage drop ΔV_c of 1 mV. In Sample B the interface resistance is about a factor 3.5 lower than in Sample A and the temperature gradient is much larger. Since no significant indication from thermal spin injection is visible there, the spin Seebeck coefficient must be well below 0.1 mV/K.

For the calculation shown above, the additional resistance due to the spin accumulation in the semiconductor was neglected. This is valid, since we are only interested in a small spin accumulation compared to the voltage drop across the barrier. In addition, the resistance of the tunnel barrier was used for the junction resistance. The effective resistance of the n-GaAs, $R_N = \rho_N \cdot L_s$ ($L_s = 7\,\mu$m, $\rho_N = 3 \cdot 10^{-4}\,\Omega$m), is in the order of $2 \cdot 10^{-9}\,\Omega\text{m}^2$ and thus about a factor of 20 lower than the interface resistance.

Altogether, a larger spin Seebeck coefficient is needed for the efficient generation of spins. However, since values in the order of $10^{-5} - 10^{-6}$ V/K are usually obtained [120], the observation of thermal spin injection is not expected from this point of view. Nevertheless, thermal spin injection was demonstrated in Ref. [88], where the electrical signal from the 3-terminal geometry describing the spin accumulation is orders of magnitude larger than theoretically expected. A reason for this might be the 3-terminal detection technique which seems to be more sensitive to a spin accumulation the larger the interface resistance is [121]. Reasons for the unexpectedly large 3-terminal voltage are discussed elsewhere [122]. Recently, thermal spin injection into n-type Ge was demonstrated [123], however, also via 3-terminal measurements and an unexpected large signal. Despite the not fully

understood 3-terminal voltage, Ref. [88] and [123] both demonstrate that, indeed, thermal spin injection into Si and Ge works. For future experiments in GaAs and for a better understanding of the 3-terminal detection method, a combination of electrical and optical detection of the spin accumulation would be desirable, which is beyond the scope of this thesis.

4.4.3. Spin pumping

Spin pumping is another way for the generation of pure spin currents. In contrast to electrical spin injection, thermal spin injection or the spin solar cell effect, the spin pumping mechanism is based on magnetization dynamics. The effect arises from the precession of the magnetization vector about the effective magnetic field of the ferromagnetic material. The working principle is sketched in Fig. 4.42c together with electrical spin injection shown in Fig. 4.42b and the optical spin orientation in Fig. 4.42a. The precessing magnetization induces spin-dependent reflection of electrons in the nonmagnetic material at the interface to the ferromagnet. The pure spin current can be imagined, as shown in Fig. 4.42c, by assuming the electron spin to flip after being reflected from the interface being equivalent to the creation of a magnon. A more detailed description is given elsewhere [125].

Usually, due to damping, a precessing magnetization will align with the external magnetic field. However, by superimposing a small oscillating field on the static magnetic field, the damping can be canceled leading to a continuous precession. This can be realized by a microwave field with a frequency in the order of 10 GHz. The resonance condition then depends on the damping parameter and the magnetic anisotropy of the ferromagnetic layer in the external static magnetic field. Being in ferromagnetic resonance (FMR), a direct spin current is generated across the interface into the connected nonmagnetic layers. In fact, a spin current flows as long as the magnetization precesses. In resonance, however,

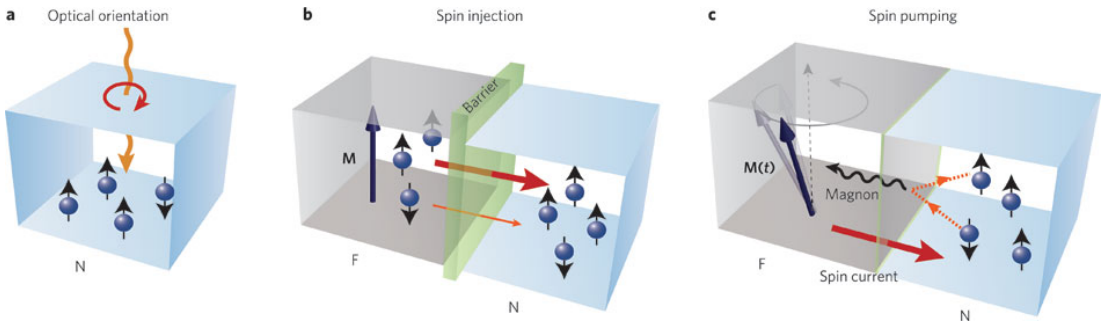

Figure 4.42.: Comparison of the spin pumping mechanism (c) with optical spin pumping (a) and electrical spin injection (b) (from [124]).

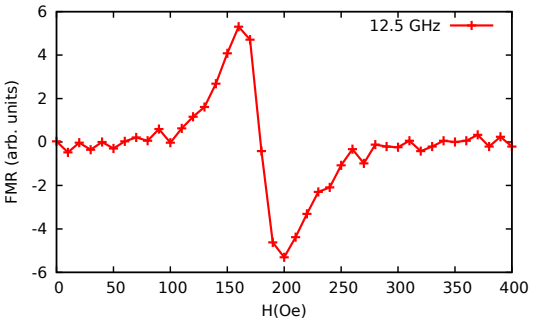

Figure 4.43: First derivative of the resonance curve, i.e. the absorbed microwave intensity at 11 K, measured via lock-in and magnetic field modulation on Sample A (see Fig. 4.32).

the precession amplitude is maximized and thus the spin current is maximized, which reflects the shortening of the magnetization along the precession axis. This generated spin current is usually detected in Pt by measuring a transverse voltage arising from the inverse Spin Hall effect (ISHE) [85]. The same effect was used recently to observe spin pumping from NiFe into n- and p-doped GaAs [86]. Since a tunnel barrier or a large interface resistance should suppress the spin current [126, 127], as for thermal spin injection, the large signal detected in n- and p-doped GaAs [86] is not expected. Moreover, the electrical detection of the ISHE may be superimposed by anisotropic magnetoresistance effects [128] and thermal effects. Thus, an optical verification of the spin pumping mechanism in GaAs is desirable.

In the following the attempt to optically observe spin pumping into n-GaAs will be described. Sample A is a perfect candidate for the experiments, on the one hand due to the low interface resistance, on the other hand since thermal spin injection is negligible as shown before. The oscillating magnetic field at the Fe contact was realized by applying a microwave field between the two Au leads connecting the U-shaped contact (see Fig. 4.32). At the same time the static magnetic field was applied along the z-axis, i.e. along the magnetic easy axis of the Fe layer and the sensitive axis for pMOKE. Consequently, the magnetization of the Fe layer is aligned along the z-direction. Due to the contact geometry with the Au layer directly above the Fe layer, the applied microwaves generate an in-plane (y-z-plane) oscillating magnetic field. Beneath both legs of the U-shaped contact the oscillating magnetic field is pointing in y-direction and thus perpendicular to the magnetization direction, resulting in a magnetization precession and an absorption of microwaves. The resonance condition was determined by measuring the reflected microwave intensity using a Schottky diode in combination with a circulator. Fig. 4.43 shows a sweep of the external magnetic field while applying a 12.5 GHz microwave field. The data shows the first derivative of the resonance curve (measured with a magnetic field modulation and a lock-in). FMR at 11 K occurs for 12.5 GHz at 180 Oe. For a 12 GHz microwave field the corresponding resonance field is at 120 Oe (see below).

The question arises if the spin current generated in resonance into the n-GaAs

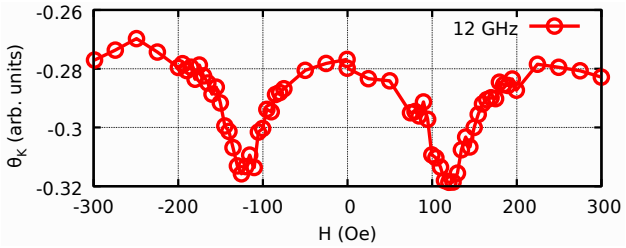

Figure 4.44.: Kerr rotation in the n-GaAs beneath the Fe contact on Sample A while applying a 12 GHz microwave field and sweeping the external magnetic field along the z-direction at 11 K. A decrease of the Kerr rotation occurs for both resonance conditions, θ_K(-120 Oe) and θ_K(+120 Oe).

can be optically detected via pMOKE at the cleaved edge as for electrical spin injection. For electrical spin injection a square wave bias voltage was used in order to enable lock-in detection, which is described in detail in Sec. 3.2. For the following experiments, the microwave field was switched on and off with a kHz frequency which allows an equivalent lock-in detection. Fig. 4.44 shows the detected Kerr rotation in the GaAs beneath the Fe contact when sweeping the external magnetic field along the z-direction. A spin current should be generated depending on the magnetization direction. The magnetization of the Fe layer switches at about 100 Oe as shown in the hysteresis curve of Fig. 4.33. A maximized spin accumulation is expected in the GaAs when the resonance condition is met. Indeed, the signal nicely shows a decrease of the Kerr rotation at −120 Oe. However, since almost the same decrease of the Kerr rotation occurs for +120 Oe where the Fe magnetization already points in the opposite direction, the change in Kerr rotation at both resonance conditions can not be related to a spin accumulation. Since the Kerr rotation in resonance is independent of the magnetization direction, the signal might be connected with a temperature increase due to the enhanced microwave absorption in resonance. An offset Kerr rotation is also visible away from resonance. Since for the lock-in detection the microwave field was modulated by switching it on and off, the offset Kerr rotation must be induced by the microwave field, probably due to an electro-optic effect as discussed in Sec. 3.2 for electrical spin injection. Altogether, as for electrical spin injection, only a difference signal of the Kerr rotation for both magnetization directions, i.e. [θ_K(120 Oe)-θ_K(-120 Oe)], would indicate a spin accumulation in the GaAs, which is below 0.01 in Fig. 4.44.

We now want to perform one-dimensional linescans of the Kerr rotation along the n-GaAs channel. Knowing the resonance field, the spin density distribution can be detected in a similar way as for electrical spin injection. Instead of taking the difference in Kerr rotation for both remanent magnetization directions (see Sec. 3.2), now the difference of the Kerr rotations for plus and minus resonance field is used. This eliminates any offset signal from the microwave field (see

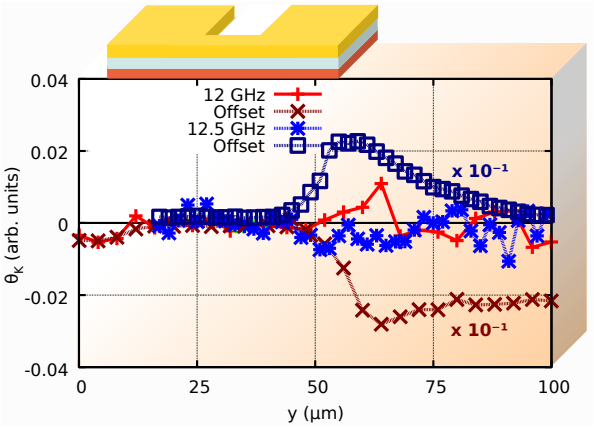

Figure 4.45: One-dimensional linescans of the Kerr rotation along the n-GaAs channel at 11 K while spin pumping (12 and 12.5 GHz). Only an offset signal illustrated by the two darker curves was observed.

Fig. 4.44). Consequently, the measurement principle is equivalent to electrical spin injection. The results are illustrated in Fig. 4.45 for 12 GHz and 12.5 GHz microwave field and the corresponding resonance field of ±120 Oe and ±180 Oe, respectively. The light red and light blue curve correspond to the spin polarization in the GaAs and are almost zero. The darker curves illustrate the distribution of the offset signal (average of the Kerr rotations for plus and minus resonance field). Interestingly, the large offset signal in the GaAs is concentrated at the contact edge. This can be explained by the inhomogeneous magnetization excitation occurring mainly at the edges in this contact geometry. However, the main result is, that no significant spin polarization can be observed in the n-GaAs with this approach, even for microwave intensities of 250 mW. Therefore, one can conclude again as for thermal spin injection, that the generated spin current due to spin pumping must be below $5 \cdot 10^3\,\mathrm{A/m^2}$ in this experiment.

Additionally, the contact geometry of Sample A (see Fig. 4.32) allows detection of the inverse spin Hall effect by probing the voltage between both outer contacts. The dependence of this voltage on the external magnetic field in z-direction while spin pumping is illustrated in Fig. 4.46. The signal contains a large offset voltage with a linear dependence on the applied magnetic field. The linear dependence indicates a small current which may stem from the microwave modulation (see above) while the voltage is detected with a lock-in technique as for the optical measurements. For both resonance conditions a decrease of the signal is clearly visible, as for the optical detection shown in Fig. 4.44. Since the behavior in resonance is similar for both magnetization directions, i.e. spin current polarizations, the signal does not originate from the ISHE. This shows again, as for the optical detection, that an offset effect occurs in resonance independent of the magnetization direction. For a potential spin current the ISHE voltage would reverse when the current polarization reverses which is connected here to the magnetization direction. The inverse spin Hall effect can be in principle hidden in the large offset signal, however, only in the order of about 100 nV. The origin of the symmetric behavior of the voltage for both resonance conditions can be attributed to the

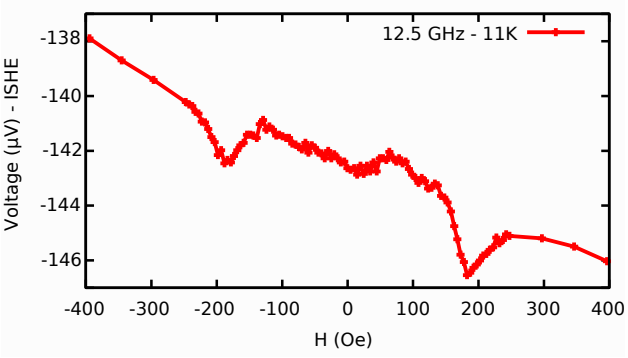

Figure 4.46.: Measurement of the inverse spin Hall effect (ISHE) voltage as a function of the external magnetic field while applying a 12.5 GHz microwave field.

anisotropic magnetoresistance (AMR) effect caused by the oscillating induction current and the oscillating magnetoresistance in the Fe layer [129]. However, since no significant spin accumulation was found optically, it was not expected to observe a large spin current and measure a significant ISHE voltage.

In summary, the comparison of spin pumping and thermal spin injection from Fe into n-GaAs clearly shows that electrical spin injection is still the most convenient way to create a spin accumulation in the semiconductor, at least for this particular sample. Spin injection by applying a thermal gradient did not result in a significant spin accumulation. The comparison with electrical spin injection shows that material systems with larger spin Seebeck coefficients are needed for the efficient generation of spins by temperature gradients. The spin pumping experiment also showed no significant spin accumulation in the n-GaAs. From the electrical spin injection experiments in Sec. 4.4.1 it is shown that a spin current density across the interface in the order of $5 \cdot 10^3\,\mathrm{A/m^2}$ is observable. Saitoh et al., for instance, extracted in their spin pumping experiments from electrical measurements of the ISHE a spin current in the order of $3.3 \cdot 10^6\,\mathrm{A/m^2}$ for NiFe on p-GaAs and $1.1 \cdot 10^5\,\mathrm{A/m^2}$ for NiFe on n-GaAs [86]. Based on this result and due to the lower interface resistance of Sample A with respect to the samples in Ref. [86], a large spin accumulation could have been expected. However, despite the low interface resistance of Sample A and similar microwave intensities in the experiment presented here, the generated spin current across the interface must be below $5 \cdot 10^3\,\mathrm{A/m^2}$, which is about two orders of magnitude lower. A possible reason might be the not optimized magnetization excitation close to the cleaved edge in this contact geometry, which should be addressed in future experiments on new samples. However, an increase of the spin current density by two orders of magnitude is unlikely. Since a potential voltage signal from the AMR effect [129] was not considered in Ref. [86], the extracted spin current densities might be overestimated there. Therefore, an optical verification of spin pumping into GaAs is important.

4.5. Spin injection into a two-dimensional electron gas

In 1990 Datta and Das proposed a novel transistor concept that is based on the manipulation of the electron spin [130]. The device requires a semiconductor heterostructure consisting of a two-dimensional electron gas (2DEG). The 2DEG enables the ballistic charge transport between the ferromagnetic source and drain electrodes. Due to the ferromagnetic contacts, the resistance of the transistor depends on the relative orientation of both magnetizations. In order to modulate the resistance via a gate voltage, as done in a conventional field effect transistor (FET), the so-called Bychkow-Rashba effect is used [131]. This effect generates an effective magnetic field perpendicular to the moving electrons in the 2DEG, which can be varied by an applied gate voltage. This allows to control spin precession and hence the resistance of the transistor. Despite an intense research for the implementation of this concept, the Spin-FET is still waiting for its realization. The working principle was already shown in 2009 [132], demonstrating an oscillatory behavior of the non-local voltage signal with varying gate voltage. However, the stated perfect agreement with a theoretical model is only valid for a one-dimensional transistor [133].

An important step towards the realization of a spin transistor is the efficient electrical spin injection into a 2DEG. Electrical spin injection into 3D semiconductors has been demonstrated in many cases as shown in previous sections and elsewhere [45, 64, 110, 113, 114]. Spin injection into a 2DEG is more difficult to achieve and has not been clearly demonstrated so far, except for the work of Koo et al. [132]. In the following, electrical spin injection from (Ga,Mn)As into a GaAs based heterostructure consisting of a 2DEG is demonstrated. The layer stack is illustrated in Fig. 4.47. In contrast to the samples shown in the previous sections, where spin injection into bulk n-GaAs is analyzed, this heterostructure consists of a 50 nm thick undoped GaAs layer above an undoped AlGaAs spacer layer and a delta doped AlGaAs layer. For the used doping profile, a 2DEG builds

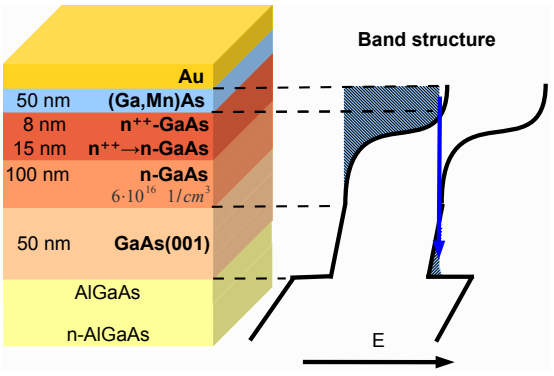

Figure 4.47: Heterostructure for spin injection from (Ga,Mn)As into a GaAs 2DEG. The 2 nm thick AlGaAs layer in between the n^{++}-GaAs ($4 \cdot 10^{18}\,cm^{-3}$) and the (Ga,Mn)As layer is not shown. The corresponding band structure with the triangular shaped potential well is sketched on the right hand side.

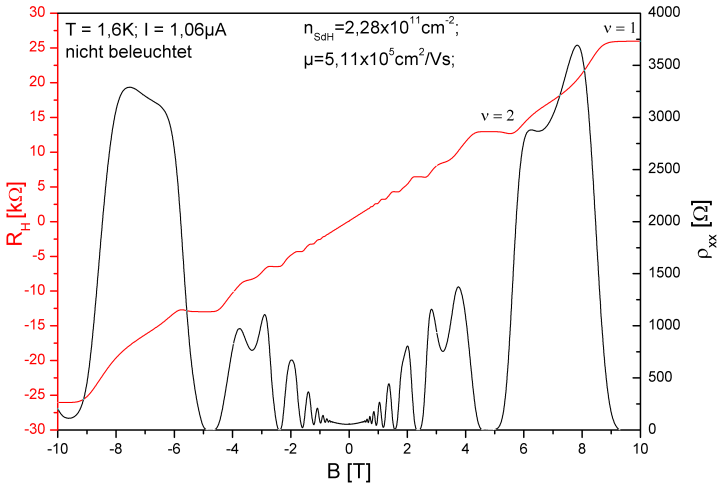

Figure 4.48: Magnetoresistance measurements of the heterostructure revealing the quantum Hall effect (red) and Shubnikow de Haas oscillations (black). In addition the filling factor ν is given for two Hall plateaus (from [134]).

up in the undoped GaAs layer close to the AlGaAs layer as sketched in Fig. 4.47. A critical point for the realization of a device was the persistence of the 2DEG after contact patterning. The sample preparation and contact patterning was done by Martin Oltscher at the chair of Prof. D. Weiss. A detailed description of the device preparation and contact patterning is given in his diploma thesis [134]. The realization of a 2DEG was shown by M. Oltscher via the observation of the quantum Hall effect and Shubnikow de Haas oscillations (see Fig. 4.48).

In the following the results obtained from the optical detection of the injected spin accumulation will be described. A comparison to the results of M. Oltscher where the spin accumulation was detected electrically in a non-local voltage geometry is given below. Fig. 4.49 shows a hysteresis loop of the Kerr rotation in the GaAs at the cleaved edge, demonstrating electrical spin injection into the GaAs based heterostructure. The hysteresis loop also represents the magnetization curve of the (Ga,Mn)As contact showing a slight rotation of the magnetization until it switches at about 50 Oe. The contact geometry will be described below in Fig. 4.50. Compared to the measurements in bulk n-GaAs presented in the previous sections, the Kerr rotation signal is about a factor of 10 smaller and

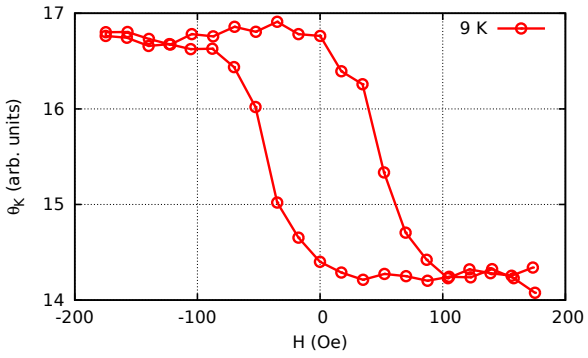

Figure 4.49: Magnetic field sweep along the z-direction while measuring the Kerr rotation at position $y = 35\,\mu m$ (see Fig. 4.50) beneath the extracting (Ga,Mn)As contact ($V_b = 0.5\,V$).

hence the signal to noise ratio is lower. This is on the one hand due to the spatial constraint of the spin accumulation in the 2DEG structure in the order of 50 nm compared to the laser spot diameter of 1 µm. On the other hand the confinement influences the optical transitions as has been shown in Spin-LED experiments by comparing the circular polarization in top-emission, where the electron spins are oriented normal to the surface, and in side-emission (or edge emission) where the electron spins are oriented in plane [64, 135]. First of all, the confinement in narrow quantum wells lifts the degeneracy of the heavy hole and the light hole valence band at the Γ-point. The light hole states are shifted to lower energies and do not contribute to the recombination process at low temperatures [64]. The recombination of spin polarized electrons from the conduction band into the heavy hole band enhances in principle the circular polarization of the emitting light (see Sec. 2.1). However, the reduced symmetry forces the orientation of the heavy hole angular momentum in the out-of-plane direction and thus perpendicular to the injected spin direction for side emission [64]. Therefore, the emission of circularly polarized light is prohibited in this geometry for narrow quantum wells [135]. Almost no circular polarization was found for a 10 nm and a 15 nm wide quantum well [64,135]. However, for the 50 nm and 100 nm wide quantum well a significant circular polarization could be observed in remanence [64]. Consequently, in not too narrow quantum wells, pMOKE on the cleaved edge should be possible but reduced in efficiency.

4.5.1. Spin density distribution

Fig. 4.50 shows a linescan along the 2DEG channel for spin extraction and spin injection. The top sketch illustrates the cleaved edge of the sample with three (Ga,Mn)As contacts. A positive voltage of 0.5 V was applied between the middle contact and the reference contact on the left hand side at a distance of 300 µm. By applying the bias voltage, electrons are flowing from the left into the middle contact where the spin accumulation is created by spin extraction. The red curve describes the spin density distribution, observed by a one-dimensional linescan of the Kerr rotation along the 2DEG channel at 9 K. The spin diffusion length can be extracted by an exponential fit of θ_K on the right hand side of the middle contact, resulting in about 3.5 µm. The effective decay length on the left hand side of the contact is shortened due to the influence of the electron drift towards the positive y-direction.

The bottom sketch in Fig. 4.50 shows the spin density distribution with a negative applied voltage, i.e., spins are injected into the 2DEG. The effective decay length on the left hand side of the contact is now increased with respect to the spin diffusion length since drift and diffusion operate in the same direction. Given that a larger spin diffusion length is extracted from this curve shows the relatively large

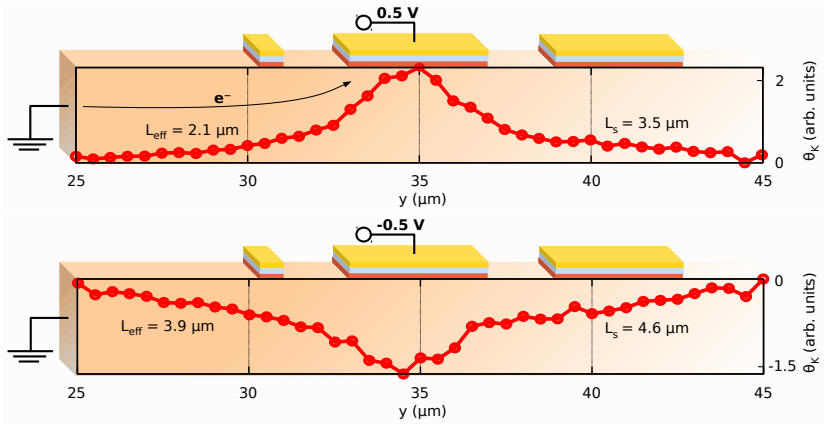

Figure 4.50.: Linescan of the Kerr rotation along the GaAs channel for spin extraction (top, 0.5 V) and spin injection (bottom, -0,5 V) at 9 K. The decay lengths extracted from exponential fits are also given.

error due to the smaller signal compared to the measurements in bulk n-GaAs as discussed above. Taking all decay lengths into account, the spin diffusion length is in the order of $3.5 \pm 1\,\mu m$. This value is consistent with the spin diffusion length found by M. Oltscher when measuring the non-local voltage signal at various distances to the injecting contact at 4.2 K [134].

Fig. 4.51 on the left shows the bias dependence of the electrically injected spin accumulation. The voltage was applied between the injecting contact and a reference contact at the end of the GaAs channel as shown in Fig. 4.50. The curve was measured beneath the injecting contact at 9 K showing the expected sign reversal when going from injection to extraction. The curve also shows a strong reduction of the spin injection efficiency for larger bias voltages above 0.5 V or below -0.5 V. Fig. 4.51 on the right shows the corresponding I-V characteristic. The small dip of the current in forward direction is characteristic for Esaki diodes and matches with the strong decrease of the current polarization at around 0.5 V,

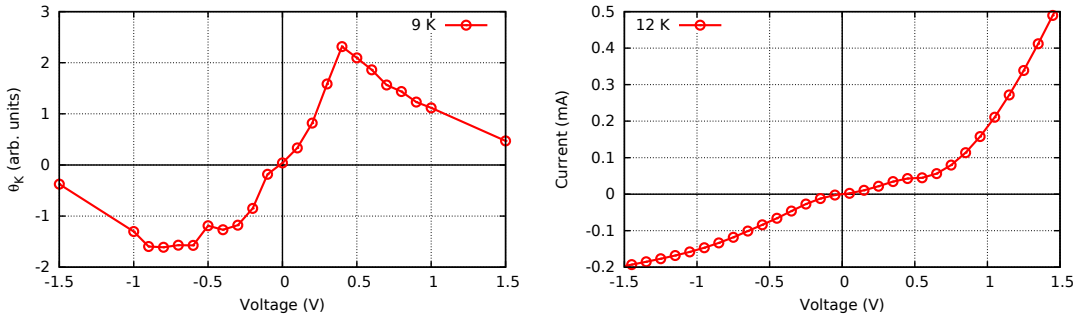

Figure 4.51.: Left: Bias dependence of the injected spin accumulation at position $y = 35\,\mu m$. Right: I-V characteristic using the same bias voltage range.

as observed earlier by Ciorga et al. [45].

4.5.2. Spin lifetime

The spin lifetime in the 2DEG is expected to be much smaller than in bulk n-GaAs. The dominant spin relaxation mechanism in GaAs-based 2DEGs is also the D'yakonov-Perel' mechanism [13]. Besides the Dresselhaus effect (see Sec. 2.2.1), an additional effective magnetic field arises from the electric field in the 2DEG due to the asymmetric confinement (structure inversion asymmetry), which is called the Bychkow-Rashba effect [131]. Since the D'yakonov-Perel' mechanism is more effective the larger the scattering time is, shorter spin lifetimes are expected with respect to bulk n-GaAs. The long scattering times in the 2DEG are indicated by the large mobility shown in Fig. 4.48, which is two orders of magnitude larger than in bulk n-GaAs. Beside the mobility, the spin lifetime also depends on other parameters of the 2DEG such as the growth direction, the quantum well width, the carrier density and the temperature [13]. For GaAs(001)-based quantum wells, spin lifetimes between 20 and 200 ps have been observed [136].

Interestingly, the spin diffusion length extracted from the data in Fig. 4.50 has the same order of magnitude as in bulk n-GaAs. Since the diffusivity D is proportional to the mobility (see Sec. 2.3), a large spin diffusion length $L_s = \sqrt{\tau_s \cdot D}$ can also occur for small spin lifetimes. In the following we want to estimate the spin lifetime τ_s via the diffusivity D and the spin diffusion length L_s ($\tau_s = L_s^2/D$). D is defined by the scattering time and the Fermi velocity (see Eq. 2.6). The scattering time can be determined from the mobility. The Fermi velocity results from the carrier density which is also denoted in Fig. 4.48. This results in a diffusivity $D = 4163\,\mathrm{cm}^2/\mathrm{s}$ for this heterostructure [134]. Consequently, the spin lifetime must be in the order of 30 ps for a spin diffusion length of 3.5 µm. Here we assumed that the electron diffusivity from conductivity measurements is the same as the spin diffusivity, as discussed at the end of Sec. 4.2. However, it has been shown in GaAs quantum wells that the spin Coulomb drag effect can reduce spin diffusion with respect to electron diffusion [137]. Nevertheless, the spin lifetime still should be in the order of 100 ps.

Spin lifetimes in the order of 100 ps or below can not be extracted from Hanle measurements in this setup (see Sec. 3.2) since much larger magnetic fields ($\sim 5\,\mathrm{kOe}$) would be necessary to depolarize the spin accumulation. The small spin lifetime is therefore consistent with the measured Hanle curves showing no significant depolarization within the maximum range of the external magnetic field (see Fig. 4.52). The Hanle measurements were observed next to the injecting or extracting contact at $y = 32\,\mu\mathrm{m}$ (see Fig. 4.50). For electrical spin injection ($V_b = -0.5\,\mathrm{V}$), one Hanle measurement plotted in Fig. 4.52 was performed beneath the contact area, showing no depolarization as well. A slight depolarization was only visible

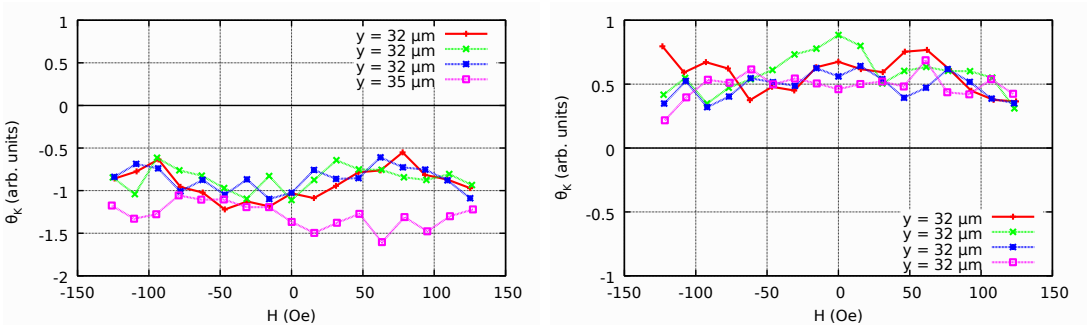

Figure 4.52.: Hanle measurements at y = 32 µm for spin injection (left, $V_b = -0.5\,V$) and spin extraction (right, $V_b = 0.5\,V$). The magenta curve on the left hand side shows the depolarization at position y = 35 µm.

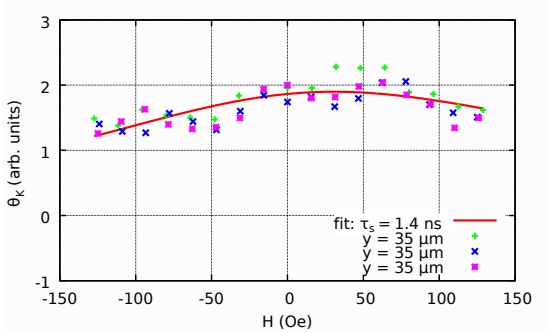

Figure 4.53: Hanle measurements at y = 35 µm for spin extraction ($V_b = 0.5\,V$). The fit yields a spin lifetime of 1.4 ± 0.5 ns.

when, for positive applied voltages, the measurement was performed directly beneath the contact (y = 35 µm). There, a spin lifetime of about 1.4 ± 0.5 ns for $V_b = 0.5\,V$ could be extracted from the Hanle curves (see Fig. 4.53). A possible explanation for this behavior is the change in band-bending when applying a forward bias. The positive voltage reduces the depletion zone in the GaAs so that a spin accumulation may be created in the n-doped region as well when the laser spot is at this position (see Fig. 4.47). Since the spin lifetime in the n-GaAs layer is much larger, a Hanle depolarization can be observed.

A drawback of the optical detection technique is the continuous generation of electron-hole pairs in the heterostructure by the probe laser beam. In contrast to bulk n-GaAs (see Sec. 3.4), the increase of the electron density in the 2DEG is more critical since it can generate a parallel conduction channel [134]. Thus, the question arises if transport also occurs in the n-GaAs layer and if the Kerr rotation originates from the spin accumulation in this region. However, if transport was dominated by the n-GaAs layer and not the 2DEG, a depolarization of the spin accumulation would be visible in the Hanle curves due to the much larger spin lifetime in n-GaAs. Furthermore, the observation of the same spin diffusion length in electrical detection, where a parallel transport channel in the n-GaAs can be excluded [134], indicates that spin injection into the 2DEG is in-

deed demonstrated. However, the electrical results are not fully understood yet: On the one hand the Hanle curves observed in a non-local voltage geometry indicate a spin lifetime of about 10 ns [134]. This relatively large spin lifetime is expected for bulk n-GaAs, not for a 2DEG. However, such narrow Hanle lineshapes were only observed for spin injection using a certain bias voltage. On the other hand the non-local voltage signal was unexpectedly large for these bias voltages, so that the analysis yields a spin polarization of the injection current of more than 100%. A possible explanation might be that the "standard model of spin injection" is not applicable to this close to ballistic regime with a mean free path of a few µm. Further investigations are needed to really clarify this behavior.

Altogether, the optical and electrical results indicate that indeed spin injection into a 2DEG works, which is an important step towards the realization of a spin-FET. A further step will be the integration of a gate contact. If spin precession could be induced by the gate voltage, it would be an additional prove for electrical spin injection into a 2DEG.

5. Summary and outlook

Semiconductor spintronics is an active research field which promises a huge improvement compared to conventional charge-based electronics. By combining ferromagnets with semiconductors the realization of storage, logic and communications capabilities on a single chip should be possible. The basic concept of a spintronic device requires three key features in a ferromagnet/semiconductor heterostructure: spin injection, spin manipulation and spin detection. For spin-based transistors, in particular, the efficient injection of spins is crucial in order to achieve an advantage in power consumption.

In this work spin injection into GaAs from Fe and (Ga,Mn)As was investigated. (Ga,Mn)As is a dilute magnetic semiconductor exhibiting a large spin polarization at the Fermi energy in the ferromagnetic state. Both heterostructures are promising candidates for semiconductor spintronic devices. The advantages of GaAs are on the one hand the large spin lifetime, on the other hand the epitaxial growth of ferromagnetic materials. In addition, GaAs is a direct semiconductor which opens the window for the integration of optoelectronic features. For the realization of any spintronic device the detailed knowledge about the spin lifetime, the spatial distribution of spin-polarized carriers and the influence of electric fields is essential. In the present work all these aspects have been analyzed by optical measurements of the polar magneto-optic Kerr effect (pMOKE) at the cleaved edge of the samples.

First of all, spin injection from Fe and (Ga,Mn)As into n-GaAs was verified by two-dimensional pMOKE scans at the cleaved edge at low temperatures. The results demonstrate the powerful detection method by imaging the spin accumulation in the n-GaAs channel in remanence and even below the ferromagnetic contacts, which is a unique feature of this measurement geometry. The different spin density distribution from both injector materials unveils the inhomogeneous current density across the Schottky barrier arising from the relatively low interface resistance of the Fe contact, in contrast to the (Ga,Mn)As contact.

Further investigations have shown that a nonuniform current in the n-GaAs channel also affects the injected spin density distribution. The pronounced electric field beneath the contact area when electrically extracting spins generates a drift towards the diffusion side of the GaAs channel. This effect was not considered so

far and could be nicely reproduced by two-dimensional simulations of the electron drift and spin diffusion. The effect shifts the maximum spin accumulation beneath the contact area towards the contact edge at the diffusion side of the n-GaAs channel. As a consequence, Hanle curves are widened when measured on this side of the contact. Thus, extracting the spin lifetime τ_s with the frequently used one-dimensional model spuriously leads to a strong bias and contact distance dependence of τ_s. Correct spin lifetimes could be extracted by using a fitting procedure with a novel two-dimensional model. The remaining variations with distance and bias can be attributed to Joule heating or the presence of electric fields around the contact area. The experiment for the first time has shown the influence of the nonuniform current density through electrical spin injection on Hanle lineshapes and the importance for the determination of the spin lifetime in electrical spin injection experiments.

Furthermore a novel spintronic device that combines the principle of a solar cell with the creation of spin accumulation could be realized in this work. The working principle is demonstrated by using the laser beam simultaneously as a light source for the generation of electron-hole pairs and for the detection of the generated spin accumulation via the polar magneto-optic Kerr effect (pMOKE). The spin solar cell effect could also be observed electrically in a non-local voltage geometry where the creation of spin-polarized carriers by illumination and their detection are separated. In addition, a second working mode was realized by applying a negative voltage to the (Ga,Mn)As contact: the spin photodiode effect. Here, the negative bias drives the optically excited spins from the (Ga,Mn)As conduction band into the GaAs layer, resulting in a sign reversal of the spin polarization with respect to the spin solar cell effect. Both effects are prototypical for the basic idea of semiconductor spintronics. The effects can be used to create a spin photo-sensor where light is not only converted into a current or a voltage, but additionally into a spin current and a spin accumulation. The spin solar cell effect also enables a new and efficient method for the optical generation of spins with unpolarized light, independent of optical selection rules and not limited to certain wavelengths. The very general mechanism behind the spin solar cell effect is expected to allow adaptation to different material systems such as Fe on Si. Since room-temperature spin injection into GaAs or Si has already been achieved, all requirements for a working room-temperature spin solar cell are fulfilled.

In order to reduce energy consumption in future spintronic devices, modern concepts as thermal spin injection and spin pumping try to avoid charge currents which cause Joule heating. The investigation of both effects in the present work has shown the practical obstacles that have to be overcome for efficient spin injection into a semiconductor like GaAs. Despite the low interface resistance of the used Fe/n-GaAs sample, spin injection by applying a thermal gradient did not result in a significant spin accumulation. The comparison with electrical spin injection on the same sample shows that larger spin Seebeck coefficients are

necessary for the generation of a sizeable spin current. In addition a direct comparison with electrical detection, e.g. the three-terminal geometry, should provide a better understanding of this effect.

Spin pumping is another method for the generation of pure spin currents and is based on magnetization dynamics. Spin pumping is usually observed electrically via the inverse spin Hall effect. Due to possible side effects in the electrical signal, the optical verification of spin pumping is desirable. However, in the present work no clear indication of spin accumulation could be observed in the GaAs by bringing the Fe layer into ferromagnetic resonance. This is in mismatch with recent spin pumping experiments into GaAs where a large spin current was extracted from the observed inverse Spin Hall voltage. Despite the lower interface resistance of the Fe/n-GaAs sample used in the present experiment, the spin current density seems to be at least two orders of magnitude lower than reported in the literature. The reported value might be overestimated due to possible artifacts in the electrical signal. Therefore, an optical verification of the spin pumping mechanism and the generated spin accumulation in GaAs would be important. Future experiments should clarify whether spin pumping into semiconductors really is efficient, ideally with an optimized contact geometry and a maximized magnetization excitation close to the cleaved edge.

Finally, spin injection from (Ga,Mn)As into a two-dimensional electron gas (2DEG) was investigated. For the realization of spin-based transistors, e.g. the Datta-Das spin field effect transistor, electrical spin injection into a 2DEG is a crucial step which has not yet been clearly demonstrated. In the present work, the optical measurements on the cleaved edge demonstrate electrical spin injection into the GaAs based heterostructure. The observed spin diffusion length of 3.5 µm is consistent with the results obtained by electrical detection on a similar sample. A spin lifetime of about 100 ps could be estimated from the spin diffusion length and the large mobility in the 2DEG. The relatively small spin lifetime is expected from such heterostructures and is consistent with Hanle measurements showing almost no depolarization of the spin accumulation within the applied external magnetic field range. This observation excludes that the spin accumulation or the spin transport take place in the n-doped bulk region showing a larger spin lifetime. However, in contrast to the electrical detection method, the creation of a parallel transport channel in the n-GaAs due to the generation of electron-hole pairs during the optical measurements can not be excluded. This influence should be analyzed in future experiments. Furthermore, the electrical results on a similar sample are not yet completely understood. On the one hand the Hanle curves showed an unexpected large spin lifetime of about 10 ns, on the other hand the non-local voltage signal is larger than theoretically predicted. Future experiments using a combination of electrical and optical detection should give a better understanding of the system. Nevertheless, the realization of electrical spin injection into a 2DEG brings us closer to spin-based transistors.

In summary, the present work provides further insights into the generation, the distribution and the lifetime of spins in GaAs. In addition the spin solar cell effect is demonstrated, a novel mechanism for the optical generation of spins with potential for future spintronic applications. Also important for spin-based devices as transistors is the presented realization of electrical spin injection into a two-dimensional electron gas. The next step should be the manipulation and control of the injected spins (without using external magnetic fields) and the demonstration of functionality at room temperature.

A. Appendix

A.1. MBE picture

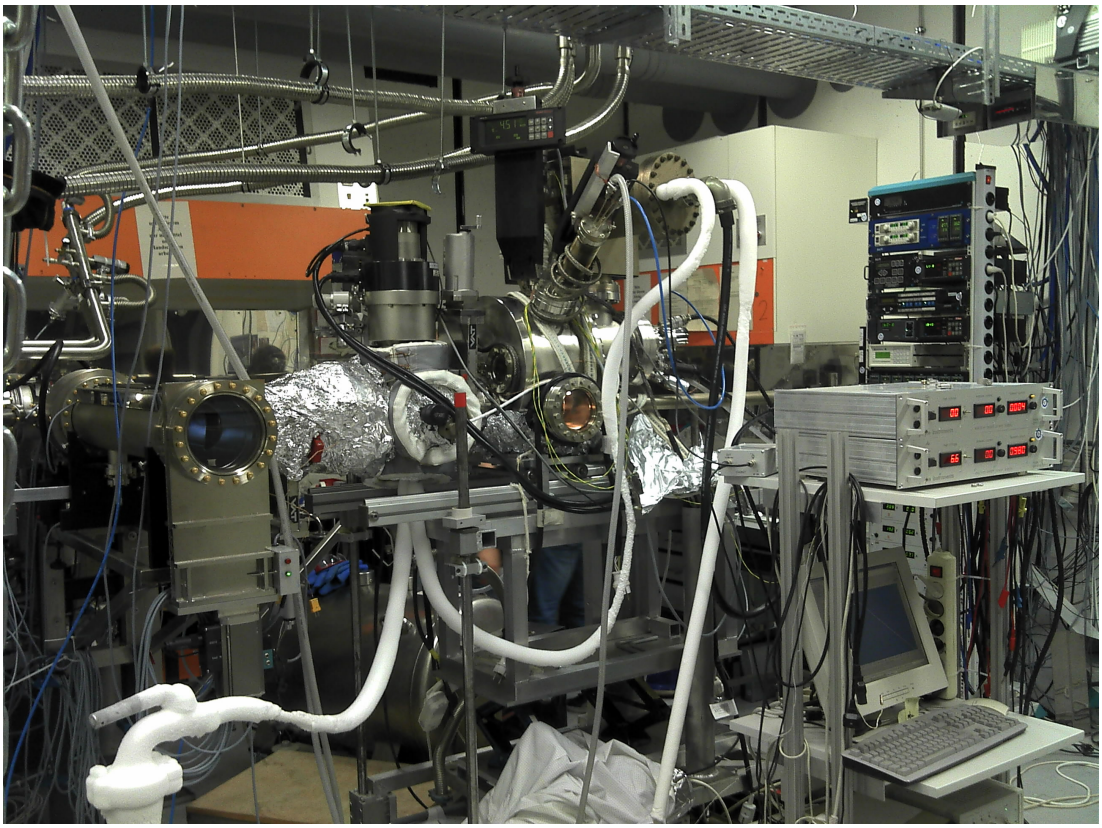

Figure A.1.: Picture of the transportable metal MBE during film growth while connected to the III-V semiconductor MBE on the left.

A.2. Optical setup picture

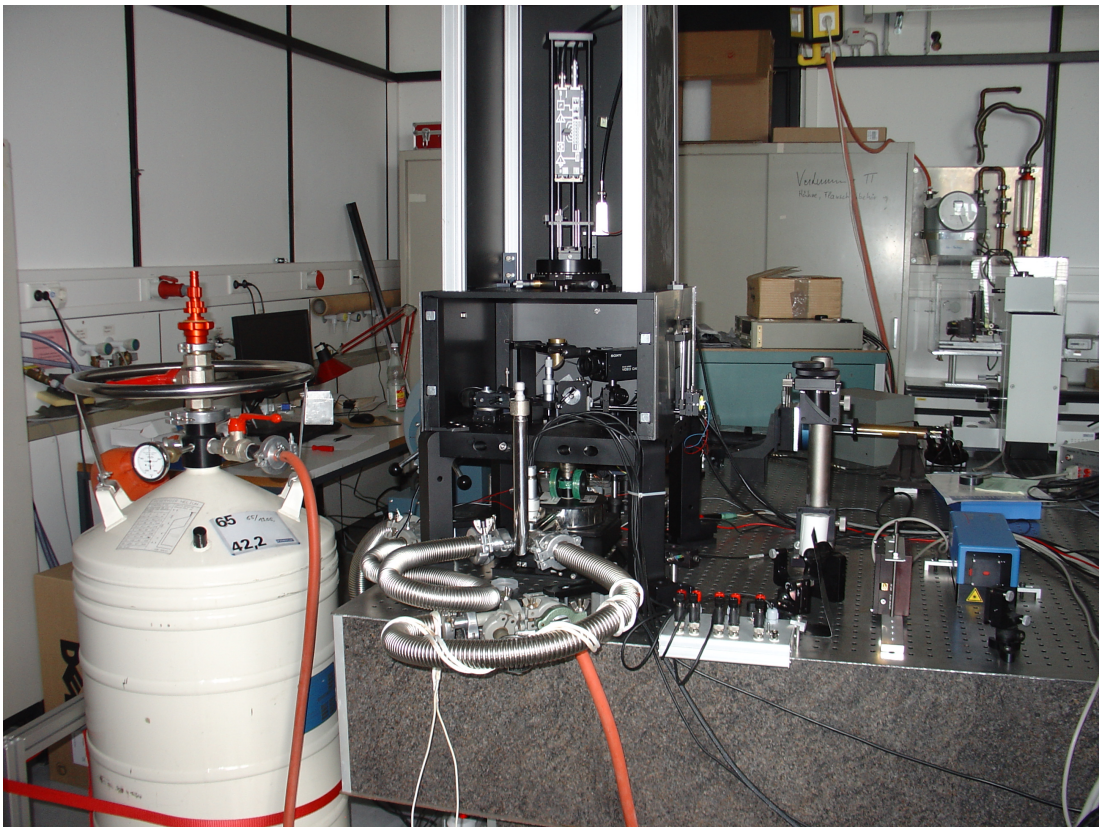

Figure A.2.: Picture of the optical setup with the scanning Kerr microscope in the middle. The tuneable diode laser is on the right hand side (blue), on the left the helium can is visible.

Bibliography

[1] G. E. Moore, "Cramming More Components onto Integrated Circuits," *Electronics*, vol. 38, 114–117, Apr. 1965.

[2] M. N. Baibich, J. M. Broto, A. Fert, F. Nguyen van Dau, F. Petroff, P. Etienne, G. Creuzet, A. Friederich, and J. Chazelas, "Giant magnetoresistance of (001)Fe/(001)Cr magnetic superlattices," *Physical Review Letters*, vol. 61, 2472–2475, Nov. 1988.

[3] G. Binasch, P. Grünberg, F. Saurenbach, and W. Zinn, "Enhanced magnetoresistance in layered magnetic structures with antiferromagnetic interlayer exchange," *Physical Review B*, vol. 39, 4828–4830, Mar. 1989.

[4] K. C. Hall and M. E. Flatté, "Performance of a spin-based insulated gate field effect transistor," *Applied Physics Letters*, vol. 88, 162503, Apr. 2006.

[5] E. Tsymbal and I. Zutic, *Handbook of Spin Transport and Magnetism*. CRC Press, 2012.

[6] T. Taniyama, E. Wada, M. Itoh, and M. Yamaguchi, "Electrical and optical spin injection in ferromagnet/semiconductor heterostructures," *NPG Asia Materials*, vol. 3, 65–73, July 2011.

[7] J. M. Kikkawa and D. D. Awschalom, "Resonant Spin Amplification in n-Type GaAs," *Physical Review Letters*, vol. 80, 4313–4316, May 1998.

[8] D. Hägele, M. Oestreich, W. W. Rühle, N. Nestle, and K. Eberl, "Spin transport in GaAs," *Applied Physics Letters*, vol. 73, 1580, Sept. 1998.

[9] J. M. Kikkawa and D. D. Awschalom, "Lateral drag of spin coherence in gallium arsenide," *Nature*, vol. 397, 139–141, Jan. 1999.

[10] R. Fiederling, M. Keim, G. Reuscher, W. Ossau, G. Schmidt, A. Waag, and L. W. Molenkamp, "Injection and detection of a spin-polarized current in a light-emitting diode," *Nature*, vol. 402, 787–790, Dec. 1999.

[11] Y. Ohno, D. K. Young, B. Beschoten, F. Matsukura, H. Ohno, and D. D. Awschalom, "Electrical spin injection in a ferromagnetic semiconductor heterostructure," *Nature*, vol. 402, 790–792, Dec. 1999.

[12] P. Kotissek, M. Bailleul, M. Sperl, A. Spitzer, D. Schuh, W. Wegscheider, C. H. Back, and G. Bayreuther, "Cross-sectional imaging of spin injection into a semiconductor," *Nature Physics*, vol. 3, 872–877, Dec. 2007.

[13] I. Žutić, J. Fabian, and S. Das Sarma, "Spintronics: Fundamentals and applications," *Reviews of Modern Physics*, vol. 76, 323–410, Apr. 2004.

[14] R. I. Dzhioev, K. V. Kavokin, V. L. Korenev, M. V. Lazarev, B. Y. Meltser, M. N. Stepanova, B. P. Zakharchenya, D. Gammon, and D. S. Katzer, "Low-temperature spin relaxation in n-type GaAs," *Physical Review B*, vol. 66, 245204, Dec. 2002.

[15] M. Beck, *Electron spin relaxation, transport and strain-induced precession in n-GaAs*. PhD thesis, Universität Erlangen, 2005.

[16] P. Kotissek, *Remanente Spininjektion und zweidimensionale Spindichte-Verteilung in einem Halbleiter*. PhD thesis, Universität Regensburg, 2008.

[17] J. Fabian, A. Matos-Abiague, C. Ertler, P. Stano, and I. Žutić, "Semiconductor spintronics," *Acta Physica Slovaca*, vol. 57, 565–907, Aug. 2007.

[18] R. I. Dzhioev, K. V. Kavokin, V. L. Korenev, M. V. Lazarev, B. Y. Meltser, M. N. Stepanova, B. P. Zakharchenya, D. Gammon, and D. S. Katzer, "Low-temperature spin relaxation in n-type GaAs," *Physical Review B*, vol. 66, 245204, Dec. 2002.

[19] S. Blügel, D. Bürgler, M. Morgenstern, C. M. Schneider, and R. Waser, *Spintronics - from GMR to Quantum Information*. Lecture manuscripts of the Springschool 2009, Forschungszentrum Jülich, 2009.

[20] P. E. Hohage, G. Bacher, D. Reuter, and A. D. Wieck, "Coherent spin oscillations in bulk GaAs at room temperature," *Applied Physics Letters*, vol. 89, 231101, Dec. 2006.

[21] E. F. Schubert, *Physical Foundations of Solid-State Devices*. non-commercial, 2009.

[22] M. Hudait, P. Modak, and S. Krupanidhi, "Si incorporation and burstein–moss shift in n-type gaas," *Materials Science and Engineering: B*, vol. 60, no. 1, 1–11, 1999.

[23] G. Schmidt, D. Ferrand, L. W. Molenkamp, A. T. Filip, and B. J. van Wees, "Fundamental obstacle for electrical spin injection from a ferromagnetic metal into a diffusive semiconductor," *Physical Review B*, vol. 62, R4790–R4793, Aug. 2000.

[24] C. Chappert, A. Fert, and F. N. van Dau, "The emergence of spin electronics in data storage," *Nature Materials*, vol. 6, 813–823, Nov. 2007.

[25] A. Fert, J.-M. George, H. Jaffres, and R. Mattana, "Semiconductors Between Spin-Polarized Sources and Drains," *IEEE Transactions on Electron Devices*, vol. 54, 921–932, May 2007.

[26] E. I. Rashba, "Theory of electrical spin injection: Tunnel contacts as a solution of the conductivity mismatch problem," *Physical Review B*, vol. 62, R16267–R16270, Dec 2000.

[27] H. Lüth, *Solid Surfaces, Interfaces and Thin Films*. Springer, 2001.

[28] F. Padovani, "Field and thermionic-field emission in Schottky barriers," *Solid State Electronics*, vol. 9, 695–707, July 1966.

[29] B. Endres, "Ferromagetic Contacts on GaAs for Spin Injection and Detection," Diploma thesis, Universität Regensburg, 2008.

[30] B. L. Sharma, *Metal-Semiconductor Schottky Barrier Junctions and Their Applications*. Plenum Press, 1984.

[31] O. Wunnicke, P. Mavropoulos, R. Zeller, P. H. Dederichs, and D. Grundler, "Ballistic spin injection from Fe(001) into ZnSe and GaAs," *Physical Review B*, vol. 65, 241306, May 2002.

[32] A. Di Carlo, "TOPICAL REVIEW: Microscopic theory of nanostructured semiconductor devices: beyond the envelope-function approximation," *Semiconductor Science Technology*, vol. 18, 1, Jan. 2003.

[33] P. Mavropoulos, N. Papanikolaou, and P. H. Dederichs, "Complex Band Structure and Tunneling through Ferromagnet /Insulator /Ferromagnet Junctions," *Physical Review Letters*, vol. 85, 1088–1091, July 2000.

[34] P. H. Dederichs, P. Mavropoulos, O. Wunnicke, N. Papanikolaou, V. Bellini, R. Zeller, V. Drchal, and J. Kudrnovsky, "Importance of complex band structure and resonant states for tunneling," *Journal of Magnetism and Magnetic Materials*, vol. 240, 108–113, Feb. 2002.

[35] O. Wunnicke, P. Mavropoulos, R. Zeller, and P. H. Dederichs, "Ballistic spin injection from Fe into ZnSe(001), (111), and (110), and into GaAs(001)," *Journal of Physics Condensed Matter*, vol. 16, 4643–4659, July 2004.

[36] A. T. Hanbicki, B. T. Jonker, G. Itskos, G. Kioseoglou, and A. Petrou, "Efficient electrical spin injection from a magnetic metal/tunnel barrier contact into a semiconductor," *Applied Physics Letters*, vol. 80, 1240–1242, Feb. 2002.

[37] A. T. Hanbicki, O. M. J. van't Erve, R. Magno, G. Kioseoglou, C. H. Li, B. T. Jonker, G. Itskos, R. Mallory, M. Yasar, and A. Petrou, "Analysis of the transport process providing spin injection through an Fe/AlGaAs Schottky barrier," *Applied Physics Letters*, vol. 82, 4092, June 2003.

[38] X. Lou, C. Adelmann, S. A. Crooker, E. S. Garlid, J. Zhang, K. S. M. Reddy, S. D. Flexner, C. J. Palmstrøm, and P. A. Crowell, "Electrical detection of spin transport in lateral ferromagnet-semiconductor devices," *Nature Physics*, vol. 3, 197–202, Mar. 2007.

[39] H. Ohno, A. Shen, F. Matsukura, A. Oiwa, A. Endo, S. Katsumoto, and Y. Iye, "(Ga,Mn)As: A new diluted magnetic semiconductor based on GaAs," *Applied Physics Letters*, vol. 69, 363–365, July 1996.

[40] A. X. Gray, J. Minár, S. Ueda, P. R. Stone, Y. Yamashita, J. Fujii, J. Braun, L. Plucinski, C. M. Schneider, G. Panaccione, H. Ebert, O. D. Dubon, K. Kobayashi, and C. S. Fadley, "Bulk electronic structure of the dilute magnetic semiconductor $Ga_{1-x}Mn_xAs$ through hard x-ray angle-resolved photoemission," *Nature Materials*, vol. 11, 957–962, Nov. 2012.

[41] L. Esaki, "New Phenomenon in Narrow Germanium p-n Junctions," *Physical Review*, vol. 109, 603–604, Jan. 1958.

[42] M. Utz, *Epitaxie von (Ga,Mn)As*. PhD thesis, Universität Regensburg, Oct. 2012.

[43] M. Kohda, Y. Ohno, K. Takamura, F. Matsukura, and H. Ohno, "A Spin Esaki Diode," *Japanese Journal of Applied Physics*, vol. 40, 1274, Dec. 2001.

[44] P. van Dorpe, Z. Liu, W. van Roy, V. F. Motsnyi, M. Sawicki, G. Borghs, and J. de Boeck, "Very high spin polarization in GaAs by injection from a (Ga,Mn)As Zener diode," *Applied Physics Letters*, vol. 84, 3495, May 2004.

[45] M. Ciorga, A. Einwanger, U. Wurstbauer, D. Schuh, W. Wegscheider, and D. Weiss, "Electrical spin injection and detection in lateral all-semiconductor devices," *Physical Review B*, vol. 79, 165321, Apr. 2009.

[46] P. Sankowski, P. Kacman, J. A. Majewski, and T. Dietl, "Spin-dependent tunneling in modulated structures of (Ga,Mn)As," *Physical Review B*, vol. 75, 045306, Jan. 2007.

[47] P. Van Dorpe, W. Van Roy, J. De Boeck, G. Borghs, P. Sankowski, P. Kacman, J. A. Majewski, and T. Dietl, "Voltage-controlled spin injection in a (Ga,Mn)As/(Al,Ga)As zener diode," *Physical Review B*, vol. 72, 205322, Nov. 2005.

[48] G. Bayreuther, M. Dumm, B. Uhl, R. Meier, and W. Kipferl, "Magnetocrystalline volume and interface anisotropies in epitaxial films: Universal relation and Néel's model (invited)," *Journal of Applied Physics*, vol. 93, 8230–8235, May 2003.

[49] J. Wenisch, C. Gould, L. Ebel, J. Storz, K. Pappert, M. J. Schmidt, C. Kumpf, G. Schmidt, K. Brunner, and L. W. Molenkamp, "Control of Magnetic Anisotropy in (Ga,Mn)As by Lithography-Induced Strain Relaxation," *Physical Review Letters*, vol. 99, 077201, Aug. 2007.

[50] F. Hoffmann, G. Woltersdorf, W. Wegscheider, A. Einwanger, D. Weiss, and C. H. Back, "Mapping the magnetic anisotropy in (Ga,Mn)As nanostructures," *Physical Review B*, vol. 80, 054417, Aug. 2009.

[51] S. A. Crooker, M. Furis, X. Lou, C. Adelmann, D. L. Smith, C. J. Palmstrøm, and P. A. Crowell, "Imaging Spin Transport in Lateral Ferromagnet/Semiconductor Structures," *Science*, vol. 309, 2191–2195, Sept. 2005.

[52] J. H. Versluis, A. V. Kimel, A. Kirilyuk, P. Grabs, F. Lehmann, G. Schmidt, L. W. Molenkamp, and T. Rasing, "Electric-field induced modulation of the magneto-optical Kerr effect in a (Zn,Be,Mn)Se/GaAs spintronic device," *Physical Review B*, vol. 80, 193303, Nov. 2009.

[53] D. D. Sell and H. C. Casey, "Optical absorption and photoluminescence studies of thin GaAs layers in GaAs-$Al_xGa_{1-x}As$ double heterostructures," *Journal of Applied Physics*, vol. 45, 800–807, Feb. 1974.

[54] T. T. Chiang and W. E. Spicer, "Arsenic on GaAs: Fermi-level pinning and thermal desorption studies," *Journal of Vacuum Science Technology*, vol. 7, 724–730, May 1989.

[55] J. S. Blakemore, "Semiconducting and other major properties of gallium arsenide," *Journal of Applied Physics.*, vol. 53, R123, Oct. 1982.

[56] M. Griesbeck, "Experimente zur Spindynamik in Halbleitern," Diploma thesis, Universität Regensburg, 2008.

[57] M. Furis, D. L. Smith, S. Kos, E. S. Garlid, K. S. M. Reddy, C. J. Palmstrøm, P. A. Crowell, and S. A. Crooker, "Local Hanle-effect studies of spin drift and diffusion in n:GaAs epilayers and spin-transport devices," *New Journal of Physics*, vol. 9, 347, Sept. 2007.

[58] C. Awo-Affouda, O. M. J. van't Erve, G. Kioseoglou, A. T. Hanbicki, M. Holub, C. H. Li, and B. T. Jonker, "Contributions to Hanle lineshapes in Fe/GaAs nonlocal spin valve transport," *Applied Physics Letters*, vol. 94, 102511, Mar. 2009.

[59] J. Shiogai, M. Ciorga, M. Utz, D. Schuh, T. Arakawa, M. Kohda, K. Kobayashi, T. Ono, W. Wegscheider, D. Weiss, and J. Nitta, "Dynamic nuclear spin polarization in an all-semiconductor spin injection device with (Ga,Mn)As/n-GaAs spin Esaki diode," *Applied Physics Letters*, vol. 101, 212402, Nov. 2012.

[60] A. Fuhrer, S. F. Alvarado, G. Salis, and R. Allenspach, "Fast electrical switching of spin injection in nonlocal spin transport devices," *Applied Physics Letters*, vol. 98, 202104, May 2011.

[61] Y. S. Chen, J. Huang, A. Ludwig, D. Reuter, A. D. Wieck, and G. Bacher, "Manipulation of nuclear spin dynamics in n-GaAs using an on-chip micro-coil," *Journal of Applied Physics*, vol. 109, 016106, Jan. 2011.

[62] M. K. Chan, Q. O. Hu, J. Zhang, T. Kondo, C. J. Palmstrøm, and P. A. Crowell, "Hyperfine interactions and spin transport in ferromagnet-semiconductor heterostructures," *Physical Review B*, vol. 80, 161206, Oct. 2009.

[63] G. Salis, A. Fuhrer, and S. F. Alvarado, "Signatures of dynamically polarized nuclear spins in all-electrical lateral spin transport devices," *Physical Review B*, vol. 80, 115332, Sept. 2009.

[64] O. M. J. van't Erve, G. Kioseoglou, A. T. Hanbicki, C. H. Li, and B. T. Jonker, "Remanent electrical spin injection from Fe into AlGaAs/GaAs light emitting diodes," *Applied Physics Letters*, vol. 89, 072505, Aug. 2006.

[65] M. Sperl, *Magnetische Eigenschaften von (Ga,Mn)As-Schichten und Fe/(Ga,Mn)As-Hybridstrukturen.* PhD thesis, Universität Regensburg, 2009.

[66] A. Einwanger, M. Ciorga, U. Wurstbauer, D. Schuh, W. Wegscheider, and D. Weiss, "Tunneling anisotropic spin polarization in lateral (Ga,Mn)As/GaAs spin Esaki diode devices," *Applied Physics Letters*, vol. 95, 152101, Oct. 2009.

[67] M. Ciorga. Private communication, 2013.

[68] R. Engel-Herbert and T. Hesjedal, "Calculation of the magnetic stray field of a uniaxial magnetic domain," *Journal of Applied Physics*, vol. 97, 074504, Apr. 2005.

[69] S. P. Dash, S. Sharma, J. C. Le Breton, J. Peiro, H. Jaffrès, J.-M. George, A. Lemaître, and R. Jansen, "Spin precession and inverted Hanle effect in a semiconductor near a finite-roughness ferromagnetic interface," *Physical Review B*, vol. 84, 054410, Aug. 2011.

[70] B. Endres, F. Hoffmann, C. Wolf, A. Einwanger, M. Utz, D. Schuh, G. Woltersdorf, M. Ciorga, D. Weiss, C. H. Back, and G. Bayreuther, "Bias dependence of spin injection into GaAs from Fe, FeCo, and (Ga,Mn)As contacts," *Journal of Applied Physics*, vol. 109, 07C505, Apr. 2011.

[71] A. Spitzer, "Schottky-Kontakte auf GaAs," Diploma thesis, Universität Regensburg, 2004.

[72] H. Dery and L. J. Sham, "Spin extraction theory and its relevance to spintronics," *Physical Review Letters*, vol. 98, 046602, Jan 2007.

[73] A. N. Chantis, K. D. Belashchenko, D. L. Smith, E. Y. Tsymbal, M. van Schilfgaarde, and R. C. Albers, "Reversal of spin polarization in Fe/GaAs (001) driven by resonant surface states: First-principles calculations," *Physical Review Letters*, vol. 99, 196603, Nov 2007.

[74] B. D. Schultz, N. Marom, D. Naveh, X. Lou, C. Adelmann, J. Strand, P. A. Crowell, L. Kronik, and C. J. Palmstrøm, "Spin injection across the Fe/GaAs interface: Role of interfacial ordering," *Physical Review B*, vol. 80, 201309, Nov 2009.

[75] G. Salis, S. F. Alvarado, and A. Fuhrer, "Spin-injection spectra of CoFe/GaAs contacts: Dependence on Fe concentration, interface, and annealing conditions," *Physical Review B*, vol. 84, 041307, July 2011.

[76] L. R. Fleet, K. Yoshida, H. Kobayashi, Y. Kaneko, S. Matsuzaka, Y. Ohno, H. Ohno, S. Honda, J. Inoue, and A. Hirohata, "Correlating the interface structure to spin injection in abrupt Fe/GaAs(001) films," *Physical Review B*, vol. 87, 024401, Jan. 2013.

[77] S. Merz, "Temperaturabhängige Spininjektion von Eisen in GaAs," Diploma thesis, Universität Regensburg, 2012.

[78] B. Endres, M. Ciorga, R. Wagner, S. Ringer, M. Utz, D. Bougeard, D. Weiss, C. H. Back, and G. Bayreuther, "Nonuniform current and spin accumulation in a 1 μm thick n-GaAs channel," *Applied Physics Letters*, vol. 100, 092405, Feb. 2012.

[79] R. Wagner, "Simulation of Spin Polarized Currents with COMSOL," Thesis (Zulassungsarbeit), Universität Regensburg, 2012.

[80] M. Beck, C. Metzner, S. Malzer, and G. H. Döhler, "Spin lifetimes and strain-controlled spin precession of drifting electrons in GaAs," *Europhysics Letters*, vol. 75, 597–603, Aug. 2006.

[81] M. Furis, D. L. Smith, S. A. Crooker, and J. L. Reno, "Bias-dependent electron spin lifetimes in n-GaAs and the role of donor impact ionization," *Applied Physics Letters*, vol. 89, 102102, Sept. 2006.

[82] H.-L. Yu, X.-M. Zhang, P.-F. Wang, H.-Q. Ni, Z.-C. Niu, and T. Lai, "Measuring spin diffusion of electrons in bulk n-GaAs using circularly dichromatic absorption difference spectroscopy of spin gratings," *Applied Physics Letters*, vol. 94, 202109, May 2009.

[83] M. E. Flatté and J. M. Byers, "Spin Diffusion in Semiconductors," *Physical Review Letters*, vol. 84, 4220–4223, May 2000.

[84] I. D'Amico and G. Vignale, "Spin diffusion in doped semiconductors: The role of Coulomb interactions," *EPL (Europhysics Letters)*, vol. 55, 566–572, Aug. 2001.

[85] F. D. Czeschka, L. Dreher, M. S. Brandt, M. Weiler, M. Althammer, I.-M. Imort, G. Reiss, A. Thomas, W. Schoch, W. Limmer, H. Huebl, R. Gross, and S. T. B. Goennenwein, "Scaling Behavior of the Spin Pumping Effect in Ferromagnet-Platinum Bilayers," *Physical Review Letters*, vol. 107, 046601, July 2011.

[86] K. Ando, S. Takahashi, J. Ieda, H. Kurebayashi, T. Trypiniotis, C. H. W. Barnes, S. Maekawa, and E. Saitoh, "Electrically tunable spin injector free from the impedance mismatch problem," *Nature Materials*, vol. 10, 655–659, Sept. 2011.

[87] K. Uchida, H. Adachi, T. An, T. Ota, M. Toda, B. Hillebrands, S. Maekawa, and E. Saitoh, "Long-range spin Seebeck effect and acoustic spin pumping," *Nature Materials*, vol. 10, 737–741, Oct. 2011.

[88] J.-C. Le Breton, S. Sharma, H. Saito, S. Yuasa, and R. Jansen, "Thermal spin current from a ferromagnet to silicon by Seebeck spin tunnelling," *Nature*, vol. 475, 82–85, July 2011.

[89] I. Žutić, J. Fabian, and S. Das Sarma, "Spin-Polarized Transport in Inhomogeneous Magnetic Semiconductors: Theory of Magnetic/Nonmagnetic p-n Junctions," *Physical Review Letters*, vol. 88, 066603, Feb. 2002.

[90] J. Fabian, I. Žutić, and S. Das Sarma, "Theory of spin-polarized bipolar transport in magnetic p-n junctions," *Physical Review B*, vol. 66, 165301, Oct. 2002.

[91] T. Kondo, J. Hayafuji, and H. Munekata, "Investigation of Spin Voltaic Effect in a p-n Heterojunction," *Japanese Journal of Applied Physics*, vol. 45, L663–L665, July 2006.

[92] J. Fabian, I. Žutić, and S. Das Sarma, "Magnetic bipolar transistor," *Applied Physics Letters*, vol. 84, 85, Jan. 2004.

[93] J. Fabian and I. Žutić, "The Ebers-Moll model for magnetic bipolar transistors," *Applied Physics Letters*, vol. 86, 133506, Mar. 2005.

[94] N. Rangaraju, J. A. Peters, and B. W. Wessels, "Magnetoamplification in a Bipolar Magnetic Junction Transistor," *Physical Review Letters*, vol. 105, 117202, Sept. 2010.

[95] J. Wunderlich, A. C. Irvine, J. Sinova, B. G. Park, L. P. Zârbo, X. L. Xu, B. Kaestner, V. Novák, and T. Jungwirth, "Spin-injection Hall effect in a planar photovoltaic cell," *Nature Physics*, vol. 5, 675–681, Sept. 2009.

[96] T. Jungwirth, J. Wunderlich, and K. Olejník, "Spin Hall effect devices," *Nature Materials*, vol. 11, 382–390, May 2012.

[97] T. Naydenova, P. Dürrenfeld, K. Tavakoli, N. Pégard, L. Ebel, K. Pappert, K. Brunner, C. Gould, and L. W. Molenkamp, "Diffusion Thermopower of (Ga,Mn)As/GaAs Tunnel Junctions," *Physical Review Letters*, vol. 107, 197201, Nov. 2011.

[98] M. Johnson and R. H. Silsbee, "Interfacial charge-spin coupling: Injection and detection of spin magnetization in metals," *Physical Review Letters*, vol. 55, 1790–1793, Oct. 1985.

[99] F. L. Bakker, A. Slachter, J.-P. Adam, and B. J. van Wees, "Interplay of Peltier and Seebeck Effects in Nanoscale Nonlocal Spin Valves," *Physical Review Letters*, vol. 105, 136601, Sept. 2010.

[100] R. K. Kawakami, Y. Kato, M. Hanson, I. Malajovich, J. M. Stephens, E. Johnston-Halperin, G. Salis, A. C. Gossard, and D. D. Awschalom, "Ferromagnetic Imprinting of Nuclear Spins in Semiconductors," *Science*, vol. 294, 131–134, Oct. 2001.

[101] R. J. Epstein, I. Malajovich, R. K. Kawakami, Y. Chye, M. Hanson, P. M. Petroff, A. C. Gossard, and D. D. Awschalom, "Spontaneous spin coherence in n-GaAs produced by ferromagnetic proximity polarization," *Physical Review B*, vol. 65, 121202, Mar. 2002.

[102] Y. Li, Y. Chye, Y. F. Chiang, K. Pi, W. H. Wang, J. M. Stephens, S. Mack, D. D. Awschalom, and R. K. Kawakami, "Inversion of Ferromagnetic Proximity Polarization by MgO Interlayers," *Physical Review Letters*, vol. 100, 237205, June 2008.

[103] I. Žutić, J. Fabian, and S. Das Sarma, "Spin injection through the depletion layer: A theory of spin-polarized p-n junctions and solar cells," *Physical Review B*, vol. 64, 121201, Sept. 2001.

[104] L. Berger, "Emission of spin waves by a magnetic multilayer traversed by a current," *Physical Review B*, vol. 54, 9353–9358, Oct. 1996.

[105] J. C. Slonczewski, "Current-driven excitation of magnetic multilayers," *Journal of Magnetism and Magnetic Materials*, vol. 159, L1–L7, June 1996.

[106] M. D. Stiles and A. Zangwill, "Anatomy of spin-transfer torque," *Physical Review B*, vol. 66, 014407, June 2002.

[107] E. B. Myers, D. C. Ralph, J. A. Katine, R. N. Louie, and R. A. Buhrman, "Current-induced switching of domains in magnetic multilayer devices," *Science*, vol. 285, 867–870, 1999.

[108] J. A. Katine, F. J. Albert, R. A. Buhrman, E. B. Myers, and D. C. Ralph, "Current-Driven Magnetization Reversal and Spin-Wave Excitations in Co /Cu /Co Pillars," *Physical Review Letters*, vol. 84, 3149–3152, Apr. 2000.

[109] H. J. Zhu, M. Ramsteiner, H. Kostial, M. Wassermeier, H.-P. Schönherr, and K. H. Ploog, "Room-Temperature Spin Injection from Fe into GaAs," *Physical Review Letters*, vol. 87, 016601, July 2001.

[110] X. Jiang, R. Wang, R. M. Shelby, R. M. Macfarlane, S. R. Bank, J. S. Harris, and S. S. Parkin, "Highly Spin-Polarized Room-Temperature Tunnel Injector for Semiconductor Spintronics using MgO(100)," *Physical Review Letters*, vol. 94, 056601, Feb. 2005.

[111] A. Sinsarp, T. Manago, F. Takano, and H. Akinaga, "Electrical Spin Injection from Out-of-Plane Magnetized FePt/MgO Tunneling Junction into GaAs at Room Temperature," *Japanese Journal of Applied Physics*, vol. 46, L4–L6, Jan. 2007.

[112] T. Manago and H. Akinaga, "Spin-polarized light-emitting diode using metal/insulator/semiconductor structures," *Applied Physics Letters*, vol. 81, 694–696, July 2002.

[113] G. Salis, A. Fuhrer, R. R. Schlittler, L. Gross, and S. F. Alvarado, "Temperature dependence of the nonlocal voltage in an Fe/GaAs electrical spin-injection device," *Physical Review B*, vol. 81, 205323, May 2010.

[114] S.-P. Dash, S. Sharma, R.-S. Patel, M.-P. de Jong, and R. Jansen, "Electrical creation of spin polarization in silicon at room temperature," *Nature*, vol. 462, 491–494, 2009.

[115] K.-R. Jeon, B.-C. Min, I.-J. Shin, C.-Y. Park, H.-S. Lee, Y.-H. Jo, and S.-C. Shin, "Electrical spin accumulation with improved bias voltage dependence in a crystalline CoFe/MgO/Si system," *Applied Physics Letters*, vol. 98, 262102, June 2011.

[116] T. Suzuki, T. Sasaki, T. Oikawa, M. Shiraishi, Y. Suzuki, and K. Noguchi, "Room-Temperature Electron Spin Transport in a Highly Doped Si Channel," *Applied Physics Express*, vol. 4, 023003, Feb. 2011.

[117] C. H. Li, O. M. J. van't Erve, and B. T. Jonker, "Electrical injection and detection of spin accumulation in silicon at 500 K with magnetic metal/silicon dioxide contacts," *Nature Communications*, vol. 2, Mar. 2011.

[118] R. Jansen, A. M. Deac, H. Saito, and S. Yuasa, "Thermal spin current and magnetothermopower by Seebeck spin tunneling," *Physical Review B*, vol. 85, 094401, Mar. 2012.

[119] B. Scharf, A. Matos-Abiague, I. Žutić, and J. Fabian, "Theory of thermal spin-charge coupling in electronic systems," *Physical Review B*, vol. 85, 085208, Feb. 2012.

[120] A. Slachter, F. L. Bakker, J.-P. Adam, and B. J. van Wees, "Thermally driven spin injection from a ferromagnet into a non-magnetic metal," *Nature Physics*, vol. 6, 879–882, Nov. 2010.

[121] R. Jansen, "Electrical and thermal spintronics in silicon," in *International Workshop on Spin Phenomena in Reduced Dimensions*, Universität Regensburg, 2012.

[122] R. Jansen, S. P. Dash, S. Sharma, and B. C. Min, "Silicon spintronics with ferromagnetic tunnel devices," *Semiconductor Science Technology*, vol. 27, 083001, Aug. 2012.

[123] K.-R. Jeon, B.-C. Min, S.-Y. Park, K.-D. Lee, H.-S. Song, Y.-H. Park, Y.-H. Jo, and S.-C. Shin, "Thermal spin injection and accumulation in CoFe/MgO/n-type Ge contacts," *Scientific Reports*, vol. 2, Dec. 2012.

[124] I. Žutić and H. Dery, "Spintronics: Taming spin currents," *Nature Materials*, vol. 10, no. 9, 647–648, 2011.

[125] Y. Tserkovnyak, A. Brataas, and G. E. Bauer, "Enhanced Gilbert Damping in Thin Ferromagnetic Films," *Physical Review Letters*, vol. 88, 117601, Mar. 2002.

[126] A. Brataas, Y. Tserkovnyak, G. E. Bauer, and B. I. Halperin, "Spin battery operated by ferromagnetic resonance," *Physical Review B*, vol. 66, 060404, Aug. 2002.

[127] O. Mosendz, J. E. Pearson, F. Y. Fradin, S. D. Bader, and A. Hoffmann, "Suppression of spin-pumping by a MgO tunnel-barrier," *Applied Physics Letters*, vol. 96, 022502, Jan. 2010.

[128] O. Mosendz, J. E. Pearson, F. Y. Fradin, G. E. W. Bauer, S. D. Bader, and A. Hoffmann, "Quantifying Spin Hall Angles from Spin Pumping: Experiments and Theory," *Physical Review Letters*, vol. 104, 046601, Jan. 2010.

[129] Z. Feng, J. Hu, L. Sun, B. You, D. Wu, J. Du, W. Zhang, A. Hu, Y. Yang, D. M. Tang, B. S. Zhang, and H. F. Ding, "Spin hall angle quantification from spin pumping and microwave photoresistance," *Physical Review B*, vol. 85, 214423, June 2012.

[130] S. Datta and B. Das, "Electronic analog of the electro-optic modulator," *Applied Physics Letters*, vol. 56, 665–667, Feb. 1990.

[131] Y. A. Bychkov and E. I. Rashba, "Oscillatory effects and the magnetic susceptibility of carriers in inversion layers," *Journal of Physics C Solid State Physics*, vol. 17, 6039–6045, Nov. 1984.

[132] H. C. Koo, J. H. Kwon, J. Eom, J. Chang, S. H. Han, and M. Johnson, "Control of Spin Precession in a Spin-Injected Field Effect Transistor," *Science*, vol. 325, 1515–1518, Sept. 2009.

[133] P. Agnihotri and S. Bandyopadhyay, "Analysis of the two-dimensional Datta-Das spin field effect transistor," *Physica E Low-Dimensional Systems and Nanostructures*, vol. 42, 1736–1740, Mar. 2010.

[134] M. Oltscher, "Spininjektion in zweidimensionale Elektronengase," Diploma thesis, Universität Regensburg, 2011.

[135] R. Fiederling, P. Grabs, W. Ossau, G. Schmidt, and L. W. Molenkamp, "Detection of electrical spin injection by light-emitting diodes in top- and side-emission configurations," *Applied Physics Letters*, vol. 82, 2160, Mar. 2003.

[136] D. Stich, J. Zhou, T. Korn, R. Schulz, D. Schuh, W. Wegscheider, M. W. Wu, and C. Schüller, "Effect of Initial Spin Polarization on Spin Dephasing and the Electron g Factor in a High-Mobility Two-Dimensional Electron System," *Physical Review Letters*, vol. 98, 176401, Apr. 2007.

[137] C. P. Weber, N. Gedik, J. E. Moore, J. Orenstein, J. Stephens, and D. D. Awschalom, "Observation of spin Coulomb drag in a two-dimensional electron gas," *Nature*, vol. 437, 1330–1333, Oct. 2005.

Danksagung

Zu Beginn möchte ich Prof. Dr. Günther Bayreuther für das außerordentlich interessante Thema aus dem Bereich der Halbleiter-Spintronik danken. Ich schätzte vor allem die Freiheit, meine eigenen Ideen durchführen und Neues ausprobieren zu können. Danke auch für die konstruktiven Ideen im Laufe meiner Arbeit und für die fruchtbaren Diskussionen, die zum besseren Verständnis beigetragen haben.

Großer Dank gilt auch Prof. Dr. Christian Back für die aktive Unterstützung meiner Arbeit und die Möglichkeit, die Experimente an seinem Lehrstuhl durchzuführen.

Prof. Dr. Dominique Bougeard möchte ich für die freundliche Unterstützung in mehreren Bereichen danken. Zum einen für das Interesse an meiner Arbeit sowie hilfreichen Diskussionen zum Verständnis neuerer Experimente, zum anderen für die Unterstützung bei der Entwicklung von Heterostrukturen für Spininjektion ins 2DEG. In diesem Zusammenhang möchte ich auch Michael Griesbeck, Roland Völkl und Dieter Schuh für ihre Hilfe danken.

Prof. Dr. Dieter Weiss danke ich für die Möglichkeit die Einrichtungen an seinem Lehrstuhl, insbesondere den Reinraum, zu benutzen und für die ergiebige Zusammenarbeit im gemeinsamen SFB-Projekt.

Prof. Dr. Jaroslav Fabian danke ich für hilfreiche Diskussionen zur Spin Solarzelle und Spin Photodiode. Aus seiner Gruppe möchte ich noch Benedikt Scharf danken, welcher sich immer für meine Fragen zum Verhalten von Spins im Halbleiter Zeit nahm.

Ein großer Dank gilt auch Dr. Mariusz Ciorga für die Präparation zahlreicher Proben und die gute Zusammenarbeit, um die elektrische und optische Detektion in Einklang zu bringen. Dies gilt ebenso für Andreas Einwanger und Martin Oltscher, dem ich die Probe zur elektrischen Spininjektion in ein zweidimensionales Elektronengas verdanke.

Dr. Georg Woltersdorf danke ich für die Hilfe zu den Spin-Pumpen-Experimenten. Hierbei möchte ich auch Martin Obstbaum für seine anschaulichen Erklärungen auf diesem Gebiet und Markus Härtinger für vorbereitende FMR-Messungen an meinen Proben danken.

Besonderer Dank gilt auch Martin Utz, welcher sehr viel Zeit in das Wachstum der Halbleiterschichten investiert hat. Auch für die hilfsbereite Kooperation beim Anflanschen unserer Metall-MBE an die Halbleiter-MBE zur Herstellung von Spininjektionsproben bin ich zu Dank verpflichtet. In diesem Zusammenhang möchte ich auch Dr. Matthias Sperl für die freundschaftliche Zusammenarbeit danken, zum einen für die experimentelle Hilfe während dieser Wachstumsaktionen aber auch für Diskussionen zu meiner Arbeit. Danken möchte ich auch Siegfried Dorfner für Röntgenfluoreszenz-Messungen zur Eichung der MBE Verdampferquellen.

Vielen Dank auch an Robert Wagner für die gelungenen COMSOL Simulationen im Laufe seiner Zulassungsarbeit.

Maximilian Schmid möchte ich zum einen für die technische Hilfe zum optischen Aufbau danken, aber auch für seine kompetente Unterstützung bei der elektrischen Detektion der Spin-Akkumulation.

Zuletzt möchte ich mich bei allen Kollegen am Lehrstuhl Back bedanken. Generell für die freundliche Atmosphäre aber auch für die selbstlose Hilfe bei vielen Kleinigkeiten.